Analysis of Nonlinear Effects on WDM System Performance and a Novel WDM Channel Monitoring Method Through HOS-based Blind Signal Separation

Thesis Submitted

in Accordance with the Requirements of

the University of Liverpool

for the Degree of

Doctor in Philosophy

Yumang Feng

July 2004

Acknowledgement

First of all, I would like to thank my supervisor, Prof. Asoke K. Nandi, for the excellent guidance, many stimulating discussions and encouragement. It has been a pleasure and a privilege to benefit from his skills and knowledge.

I would like to acknowledge the Signal Processing and Communications (SPC) group, Department of Electrical Engineering and Electronics, the University of Liverpool, which is led by Prof. A. K. Nandi, the significant research output on Blind Source Separation (BSS) from this group has made great contribution to this thesis. I would also like to thank the colleagues in the department, Yi Huang, Edward, Giles, Vince, Lindsay, Dennis, without the help from you guys the stay in Liverpool would not have been so exciting and memorable.

I would also like to thank the British Council and the University of Liverpool for their financial support throughout the study. Without this help, the present study cannot be completed.

Finally, I would like to thank very specially to my family for their support, encouragement and understanding during my study.

Abstract

The capacity and transmission distance of a high-speed Wavelength Division Multiplexing (WDM) transmission system are basically restricted by two factors: the first comes from the optical amplifier, including limited amplifying bandwidth, finite gain flatness, accumulation of Amplified spontaneous Emission (ASE) noise, and limited output power; the other comes from fibre dispersion, nonlinearities and polarization effects.

This thesis starts from investigating the fibre dispersion and nonlinear effects on WDM system performance. Analytical models for pulse propagation in optical fibres, fibre nonlinear effects including Stimulated Brillouin Scattering (SBS), Self-Phase Modulation (SPM), Cross-Phase Modulation (XPM) and Four Wave Multiplexing (FWM) are investigated as the theoretical foundation of this thesis.

As the design of photonic systems has reached to a stage where simulation is no longer a luxury but a necessity, the thesis presents a WDM transmission system simulation platform, with a new method to evaluate transmission quality through the eye diagrams and amplitude histograms. This evaluation method provides a good tradeoff between the simpleness and accuracy.

Receiver analysis of 100 / 150 km WDM transmission systems is then performed with the help of the simulation platform. The influence of the variation in fibre parameters including fibre loss, dispersion and fibre effective core area are investigated, the influence of prechirp, rise time, extinction ratio, and sequence length on WDM system performance are also examined.

Dispersion management is a vital issue for WDM transmission systems with higher bit rate, and is investigated in-depth in this thesis. After study the Group-Velocity Dispersion (GVD) - induced limitations on WDM systems, several dispersion management schemes are presented. The influence of XPM and SPM effects on WDM transmission systems applying dispersion management are studied. The noise amplification in a dispersion-managed WDM transmission system induced by modulation instability (MI) is investigated. Example of dispersion management for 16-channel WDM transmission systems is presented.

For the proper management of WDM transmission systems and particularly optical networks that use optical add-drop multiplexing (OADM) and optical cross-connect (OXC), it is essential to monitor a variety of channel performance parameters such as SNR, BER, Q-factor, etc., without compromising transparency. In a bid to reduce the number of expensive optical components, cost-effective monitoring solutions aim to perform most of the processing electronically. In this thesis we have proposed and demonstrated an optical transmission monitoring technique that utilizes blind signal separation methods based on higher-order statistics and an optical-loop structure. This technique shows a reduced complexity, a reformative cost-efficiency, and an improved performance.

Contents

Abbreviations

AM	Amplitude modulation
AML	Approximate maximum-likelihood
APD	Avalanche photo diode
ASE	Amplified spontaneous emission
ASK	Amplitude shift keying
BER	Bit error rate
BSS	Blind signal separation
CRLB	Cramer-Rao lower bound
CW	Continuous wave
DCF	Dispersion compensating fibre
DD	Direct detection
DSF	Dispersion shifted fibre
DST	Dispersion supported transmission
EDFA	Erbium doped fibre amplifier
EML	Extend maximum-likelihood
EVD	Eigenvalue decomposition
FFP	Fibre Fabry-Perot
FFT	Fast Fourier transform
FP	Fabry-Perot

FWHM	Full width half maximum
FWM	Four wave mixing
GA	Gaussian approximation
GVD	Group-velocity dispersion
HOS	Higher-order statistics
ICA	Independent component analysis
IF	Intermediate frequency
IM	Intensity modulation
ISI	Inter-symbol interference
JADE	Joint approximate diagonalization of eigenmatrices
LS	Least squares
MaSSFOC	Maximum sum of squared fourth-order cumulants
MI	Modulation instability
ML	Maximum-likelihood
MZ	Mach-Zehnder
NRZ	Non return-to-zero
NZDF	Non-zero dispersion fibre
OADM	Optical add-drop multiplexing
OOK	On-off keying
OPR	Optically preamplified receiver
OSNR	Optical signal-to-noise ratio
OXC	Optical cross-connect

PCA	Principal component analysis
PDF	Probability density function
PRBS	Pseudo random binary sequence
PSD	Power spectrum density
RX	Receiver
SAD	Symmetric adaptive decorrelation
SBS	Stimulated Brillouin scattering
SNR	Signal-to-noise ratio
SOA	Semiconductor optical amplifier
SOS	Second-order statistics
SPM	Self-phase modulation
SSMF	Standard single mode fibre
SVD	Singular value decomposition
TW	Travelling wave
TX	Transmitter
WDA	Wavelength-dependent attenuator
WDM	Wavelength division multiplexing
WP	Waveform-preserving

Chapter 1

Introduction

It is well known that, from the late 1990's, the demand for telecommunications capacity has been driven by the Internet. The internet itself has been driven by the availability of data in electronic form, and of inexpensive personal computers. The telecommunications network, once dominated by voice traffic, now carries more data than voice. Data traffic, unlike voice which is fixed per link, grows because of demand for higher-quality images, sound and video. There will probably be an ultimate data limit that the average user will be able to comprehend, but this has yet to be reached.

Until the late 1980's the growth in capacity was planned to be met by increasing the data rate along a fibre using a single wavelength. This was known as Time Division Multiplexing. Various schemes were proposed to overcome the 'Electronic Bottleneck' caused by the speed of electronic de-multiplexers. One, Optical Time

Division Multiplexing (OTDM), used interleaved pulses generated by a common source, but modulated by separated modulators, to provide a data rate several times the limit of each modulator. Dispersion in the optical link was overcome by using Soliton transmission, where the dispersion and the nonlinearity were used to balance each other exactly. However, the approach of increasing channel rate was only expandable to a certain level [1], and certainly could not meet an 'exponential' growth in capacity demanded by the internet.

Wavelength Division Multiplexing (WDM) has provided the scalability necessary to cope with the capacity demands of data-driven communications. WDM started humbly, with two channels on different optical wavelengths. The method of multiplexing and de-multiplexing was to use simple optical filters. This is far easier than using timing based de-multiplexers such as required for OTDM. WDM has now broken the 160-channel barrier, extending into previously dark regions of the fibre spectrum by the use of new wideband optical amplifier technologies. This is wideband WDM.

However, wider optical bandwidths push components to their performance limits [2]. For example, amplifiers and filters need to operate over extended wavelength ranges, and increased nonlinear effects in fibres due to greater numbers of channels cause optical crosstalk over wide spectral ranges. To continue an exponential growth in fibre capacity, denser WDM systems will be required as the fibre bandwidth is used up, which will have to operate with channel spacings reduced to a few times the channel bit rate. This too pushes components to their limits.

To overcome these limits and increase the capacity of WDM transmission systems, we have the following approaches:

- Increasing the bit rate of single channel to higher than 10 Gb/s, by employing techniques like new-type fibres, dispersion compensation and so on;

- Increasing the density of wavelength multiplexing, with the channel spacing of 100 GHz or even 50 GHz;

- Developing Erbium-doped Fibre Amplifier (EDFA) working at new wave band besides the traditional wave band (1530 ~ 1565 nm, C-band), e.g., L-band EDFA working at 1570 ~ 1610 nm [3], or Raman optical amplifier [4].

The capacity and transmission distance of a high-speed WDM transmission system are basically restricted by factors of two aspects. The first comes from the optical amplifier, including limited amplifying bandwidth, finite gain flatness, accumulation of Amplified Spontaneous Emission (ASE) noise, and limited output power. The combination of these factors restricts the Optical Signal-Noise Ratio (OSNR) after WDM transmission, and thus restricts the Bit Error Rate (BER) performance of the system. For the commercial EDFAs widely used in the industry, flat gain can be obtained in the band of 1542 ~ 1560 nm or 1570 ~ 1600 nm. Applying passive gain-equalizing filter such as long-period fibre grating, EDFA can obtain flat gain of 40 nm bandwidth in both C-band and L-band [5]. The major disadvantage of passive equalization is that, the inequality of each channel accumulates with the cascading of

amplifiers, which means the OSNR of the channels with insufficient optical gain will be damaged, and the system performance of the channels with exorbitant optical power will be remarkably influenced by the fibre nonlinearity. By applying active gain-equalizing filter, such as fibre acustic-optical filter, the above disadvantage can be overcome [6].

The other major restriction to WDM system performance comes from fibre dispersion, nonlinearities [7] and polarization effects [8]. These effects distort the optical signals after fibre transmission, and their combination with other optical noises influences the system performance remarkably. When the bit rate of single channel reaches 10Gb/s or even higher, the interaction of fibre dispersion and optical nonlinearities worsens the system performance seriously. The dispersion of SSMF at the wavelength of 1550nm is around 17ps/km/nm, it is difficult for binary NRZ code with negative-chirp modulation to transmit more than 100km in SSMF at the bit rate of 10Gb/s, long distance ($\geq$ 400km) [9] transmission can only be realized with dispersion management schemes using negative dispersion fibre or chirped fibre grating. To break the restriction of dispersion to WDM system performance, the Dispersion Shifted Fibre (DSF) was first introduced into the industry, which has zero dispersion at the wavelength of 1550nm; then, Non-Zero Dispersion Fibre (NZDF) was introduced to avoid the influence of Four Wave Mixing (FWM) [10], it's dispersion at the wavelength of 1550nm is large enough to restrain FWM, but small enough to support multi-hundred km transmission at the bit rate of 10Gb/s. While the effect of FWM can be restrained effectively, Self-Phase Modulation (SPM) and Cross-Phase Modulation (XPM) become primary fibre nonlinear effects that influence WDM system performance distinctly. As the influence of SPM and XPM depends on the dispersion

distributing straightly along the transmission fibre, dispersion management becomes the most efficient technique to restrain the influence of dispersion, SPM, XPM and their interaction to the performance of high-speed WDM transmission system.

The design of photonic systems has reached a stage where simulation is no longer a luxury, but a necessity. It is the advent of optical amplifiers, enabling high powers and long un-regenerated distances that have caused significant fibre nonlinearity that necessitated the use of numerical modeling: to calculate the spectral broadening caused by SPM, amplitude modulation due to XPM, crosstalk due to FWM, and the interplay of nonlinearities and dispersion. To achieve optimized transmission on optical links, equipment-makers and system integrators are assessing trade-offs between design variables including power range, fibre nonlinearities, temperature stability, gain-shaping and dispersion management. At the same time, component manufacturers are expected to deliver significant annual price decreases even as the development of multi-port, wavelength specified components (such as add-drop multiplexers, transmitters, and wavelength routers) becomes increasingly complex, quality standards increase and tolerances grow tighter. Many of these problems can be addressed with the help of automated software design tools. Just as Electronic Design Automation (EDA) tools have become an essential part of semiconductor and electronics industry development, Photonic Design Automation (PDA) tools can advance telecommunications infrastructure development.

The objective of this thesis is to set up a numerical simulation platform for WDM transmission systems based on the analytical models of fibre dispersion and nonlinear effects, and with the help of this simulation platform, the system performances for

WDM transmission over SSMF are studied; the dispersion management schemes and their contributions to the system performance are investigated; a novel WDM channel monitoring technique through blind signal separation is also presented. It is mentioned that in this thesis only 10Gb/s systems are considered and without further mention in the following chapters.

The thesis is organized as follows:

Chapter 2 of this thesis is devoted to the theoretical work of the analytical models for fibre dispersion and nonlinear effects. Firstly, the pulse propagation in optical fibres is studied, then the optical fibre nonlinear effects including Stimulated Brillouin Scattering (SBS), Self-Phase Modulation (SPM), Cross-Phase Modulation (XPM) and Four Wave Multiplexing (FWM) are investigated. Analytical models for these effects are presented in separate sections, which will be the foundation of the following chapters, and provide theoretical guidance for WDM system design.

Chapter 3 discusses the numerical simulation of WDM transmission systems. Firstly, the typical WDM system is introduced and the technology directions along which WDM systems can evolve to meet bandwidth capacity demands is duscussed. Then the expressions of signal and noise for the Optical Pre-amplifiers (OPRs) at the decision point are derived. A method to evaluate average Q-factor from the eye diagrams and amplitude histograms, and thus evaluate BER through the Q-factor, is also introduced. Finally the implementation of simulations is presented.

Chapter 4 gives the investigations on receiver performance of the OPRs in 100km and 150km 8×10Gb/s WDM transmission. Firstly, the influence of variations in fibre dispersion, fibre loss and effective core area on system performance is investigated. Then the effects of prechirp, extinction ratio and rise time of the input signal on system performance are studied. Finally, the influence of the sequence length used in simulations is discussed.

Chapter 5 is devoted to dispersion management for WDM systems. Firstly the GVD-induced limitations are investigated. Several dispersion management schemes are presented, then the influence of XPM and SPM effects on WDM transmission systems applying dispersion management are investigated. The noise amplification in a dispersion-managed WDM transmission system induced by modulation instability (MI) is investigated. Finally, example of dispersion management for 16-channel WDM transmission systems is presented.

Chapter 6 presents an effective technique to monitor the quality of WDM channels. This process uses a blind signal separation (BSS) method based on higher-order-statistics (HOS), and an optical-loop structure, to extract the baseband channels from the WDM transmission. From the reconstructed baseband waveforms, a series of WDM transmission quality parameters can be evaluated.

Chapter 7 summarizes the thesis and draws the major conclusions.

Publications arising out of the research related to this thesis are as follows:

[1] Y. Feng, V. Zarzoso and A. K. Nandi, "Quality monitoring of WDM channels with blind signal separation methods", *Journal of Optical Networking,* vol. 3, pp. 477-489, 2004.

[2] Y. Feng, V. Zarzoso and A. K. Nandi, "WDM monitoring through blind signal separation", in *Proceedings of OFC'02*, Anaheim, California, USA, pp. 746-748, 2002.

[3] Y. Feng, V. Zarzoso and A. K. Nandi, "WDM monitoring using blind signal separation based on higher-order statistics", in *Proceedings of DSP'02*, Greece, pp. 155-158, 2002.

[4] Y. Feng, V. Zarzoso and A. K. Nandi, "Application of blind signal separation to WDM optical transmission monitoring", in Procedings of EUSIPCO'02, paper # 198, France, 2002.

Chapter 2

Analytical Models for Optical Fibre Nonlinearities

The field of nonlinear fibre optics grew massively during the decade of the 1990s. A new dimension was added when optical fibres were doped with rare-earth elements and used to make amplifiers and lasers. Erbium-doped fibre amplifiers (EDFAs) attracted the most attention because they operate in the wavelength region near 1.55μm and can be used to compensation of losses in optical fibre systems. Such amplifiers were used for commercial applications beginning in 1995, and has led to a virtual revolution in the design of multichannel lightwave systems, i.e., wavelength division multiplexing (WDM) systems.

In WDM transmission systems, with the number of multiplexing channels becoming larger and the bit rate of each channel becoming higher, the impact of optical fibre nonlinear effects becomes more obvious, which limits the system performance remarkably. At this stage, it is infeasible to design a transmission system without investigating the fibre nonlinear characters.

In this chapter, the pulse propagation in optical fibres is firstly studied, and optical fibre nonlinear effects including Stimulated Brillouin Scattering (SBS), Self-Phase Modulation (SPM), Cross-Phase Modulation (XPM) and Four Wave Multiplexing (FWM) are investigated. Analytical models for these effects are presented in separate sections, which will be the foundation of the following chapters, and provide theoretical guidance for WDM system design.

2.1 Pulse propagation in fibres

For the understanding of the nonlinear phenomena in optical fibres, it is necessary to consider the theory of electromagnetic wave propagation in dispersive nonlinear media. Like all electromagnetic phenomena, the propagation of optical fields in fibres is governed by Maxwell's equations.

Derived from Maxwell's equations, pulse propagation theory is able to describe the propagation features and characters of optical fibres accurately. In this section, we use pulse propagation theory to investigate the pulse-propagation equation, and the numerical approach to the equation.

2.1.1 Pulse-propagation equation

The propagation of time-variable signals in nonlinear dispersive fibres can be described as [1]:

$$\frac{\partial A}{\partial z}+\frac{\alpha}{2}A+\frac{i}{2}\beta_2\frac{\partial^2 A}{\partial T^2}-\frac{1}{6}\beta_3\frac{\partial^3 A}{\partial T^3}$$
$$=i\gamma\left(|A|^2A+\frac{i}{\omega_0}\frac{\partial}{\partial T}(|A|^2A)-T_RA\frac{\partial|A|^2}{\partial T}\right) \tag{2.1}$$

where $A(z,t)$ is the slowly varying pulse envelope, $|A|^2$ is the optical power, z is the propagation distance, $T=t-z/v_g$ is the reference time, and α is the fibre loss. The second-order GVD coefficient β_2, higher-order GVD coefficient β_3, and the nonlinear parameter γ can be stated as:

$$\beta_2=-\frac{\lambda^2}{2\pi c}D, \tag{2.2}$$

$$\beta_3=\frac{\lambda^3}{(2\pi c)^2}\left(\lambda\frac{dD}{d\lambda}+2D\right), \tag{2.3}$$

$$\gamma=\frac{2\pi N_2}{\lambda A_{eff}}, \tag{2.4}$$

where λ is the channel wavelength, c is the light velocity in vacuum, D is the dispersion coefficient, N_2 is the Kerr coefficient, A_{eff} is the effective core area of fibre.

Equation (2.1) describes propagation of picosecond optical pulse in single-mode fibres. It is often referred to as the **nonlinear Schrödinger (NLS)** equation because it can be reduced to that form under certain conditions. It includes the effects of fibre losses through α, of chromatic dispersion through β_2 and β_3, and of fibre nonlinearity (Kerr effect) through γ.

For pulse of width $T_0 > 5$ ps, the parameters $(\omega_0 T_0)^{-1}$ and T_R / T_0 become so small (<0.001) that the last two terms in Eq. (2.1) can be neglected. As the contribution of the higher-order dispersion term is also quite small for such pulse (as long as the carrier wavelength is not too close to the zero-dispersion wavelength), one can use the simplified equation:

$$i\frac{\partial A}{\partial z} + \frac{i\alpha}{2}A - \frac{1}{2}\beta_2 \frac{\partial^2 A}{\partial T^2} + \gamma |A|^2 A = 0 . \qquad (2.5)$$

Eq. (2.5) is the simplest nonlinear equation for studying third-order nonlinear effects in optical fibres. In the special case of $\alpha = 0$, Eq. (2.5) is referred to as the NLS equation because it resembles the Schrödinger equation with a nonlinear potential term (variable z playing the role of time).

2.1.2 Numerical methods

The NLS equation is a nonlinear partial differential equation that does not generally lend itself to analytic solutions except for some specific cases in which the inverse scattering method can be employed. A numerical approach is therefore often necessary for an understanding of the nonlinear effects in optical fibres. A large number of numerical methods can be used for this purpose [1]. These can be classified into two broad categories known as: (i) the finite-difference methods; and (ii) the pseudospectral methods.

Generally speaking, pseudospectral methods are faster by up to an order of magnitude to achieve the same accuracy [2]. One method that has been used extensively to solve the pulse-propagation problem in nonlinear dispersive media is the split-step Fourier method.

The relative speed of this method compared with most finite-difference schemes can be attributed in part to the use of the fast-Fourier-transform (FFT) algorithm.

To understand the split-step Fourier method, it is useful to write Eq. (2.1) formally in the form:

$$\frac{\partial A}{\partial z} = (\hat{D} + \hat{N})A, \tag{2.8}$$

where $\hat{D}$ is a differential operator that accounts for dispersion and absorption in a linear medium and $\hat{N}$ is a nonlinear operator that governs the effect of fibre nonlinearities on pulse propagation. These operators are given by:

$$\hat{D} = -\frac{i}{2}\beta_2 \frac{\partial^2}{\partial T^2} + \frac{1}{6}\beta_3 \frac{\partial^3}{\partial T^3} - \frac{\alpha}{2}, \tag{2.9}$$

$$N = i\gamma|A|^2 . \tag{2.10}$$

In general, dispersion and nonlinearity act together along the length of the fibre. The split-step Fourier method obtains an approximate solution by assuming that in propagating the optical field over a small distance h, the dispersive and nonlinear effects can be pretended to act independently. More specifically, propagation from z to $z + h$ is carried out in two steps. In the first step, the nonlinearity acts alone, and $\hat{D} = 0$ in (2.8). In the second step, dispersion acts alone, and $\hat{N} = 0$. Mathematically,

$$A(z+h,T) \approx \exp(h\hat{D})\exp(h\hat{N})A(z,T) . \tag{2.11}$$

The exponential operator $\exp(h\hat{D})$ can be evaluated in the Fourier domain using the prescription:

$$\exp(h\hat{D})B(z,T) = \{ F^{-1}\exp[h\hat{D}(i\omega)]F \}B(z,T), \qquad (2.12)$$

where F denotes the Fourier-transform operation, $\hat{D}(i\omega)$ is obtained from (2.9) by replacing the differential operator $\partial/\partial T$ by $i\omega$, and ω is the frequency in the Fourier domain. As $\hat{D}(i\omega)$ is just a number in the Fourier space, the evaluation of Eq. (2.12) is straightforward. The use of the FFT algorithm makes numerical evaluation of Eq. (2.12) relatively fast. It is for this reason that the split-step Fourier method can be faster by up to two orders of magnitude compared with most finite-difference schemes.

To estimate the accuracy of the split-step Fourier method, a formally exact solution of Eq. (2.8) is given by:

$$A(z+h,T) = \exp[h(\hat{D}+\hat{N})]A(z,T), \qquad (2.13)$$

if $\hat{N}$ is assumed to be z independent. It is useful to recall the Baker-Hausdorff formula for two noncommuting operators $\hat{a}$ and $\hat{b}$ [1],

$$\exp(\hat{a})\exp(\hat{b}) = \exp[\ \hat{a}+\hat{b}+\frac{1}{2}[\hat{a},\hat{b}]+\frac{1}{12}[\hat{a}-\hat{b},[\hat{a},\hat{b}]]+\cdots\ ], \qquad (2.14)$$

where $[\hat{a},\hat{b}] = \hat{a}\hat{b}-\hat{b}\hat{a}$. A comparison of Eqs. (2.11) and (2.13) shows that the split-step Fourier method ignores the noncommutating nature of the operators $\hat{D}$ and $\hat{N}$. By using Eq. (2.14) with $\hat{a} = h\hat{D}$ and $\hat{b} = h\hat{N}$, the dominant error term is found to result from the

single commutator $\frac{1}{2}h^2[\hat{D},\hat{N}]$. Thus, the split-step Fourier method is accurate to second order in the step size h.

The split-step Fourier method has been applied to a wide variety of optical problems including wave propagation in atmosphere, graded-index fibres, semiconductor lasers, unstable resonators, and waveguide couplers. It is referred to as the beam-propagation method when applied to the propagation of CW optical beams in nonlinear media where dispersion is replaced by diffraction.

For the specific case of pulse propagation in optical fibres, the split-step Fourier method was first applied in 1973 [1]. Its use has become widespread since then because of its fast execution compared with most finite-difference schemes. Although the method is relatively straightforward to implement, it requires that step sizes in z and T be selected carefully to maintain the required accuracy. In particular, it is necessary to monitor the accuracy by calculating the conserved quantities such as the pulse energy (in the absence of absorption) along the fibre length. The optimum choice of step sizes depends on the complexity of the problem. Although a few guidelines are available, it may sometimes be necessary to repeat the calculation by reducing the step size to ensure the accuracy of numerical simulations.

2.2 Group-velocity dispersion (GVD)

In Section 2.1 we obtained the nonlinear Schrödinger (NLS) equation that governs propagation of optical pulses inside single mode fibres. For pulse widths >5 ps, one can use Eq. (2.5) given by:

$$i\frac{\partial A}{\partial z} = -\frac{i\alpha}{2}A + \frac{1}{2}\beta_2\frac{\partial^2 A}{\partial T^2} - \gamma|A|^2 A, \qquad (2.15)$$

where A is the slowly varying amplitude of the pulse envelope and T is measured in a frame of reference moving with the pulse at the group velocity v_g ($T = t - z/v_g$). The three terms on the right hand side of Eq. (2.15) govern, respectively, the effects of fibre losses, dispersion, and nonlinearity on pulses propagating inside optical fibres. Depending on the initial width T_0 and the peak power P_0 of the incident pulse, either dispersive or nonlinear effects may dominate along the fibre.

2.2.1 Different propagation regimes

It is useful to introduce two length scales, known as the dispersion length L_D and the nonlinear length L_{NL}. Depending on the relative magnitudes of L_D and L_{NL}, and the fibre length L, pulses can evolve quite differently.

Let us introduce a time scale normalized to the input pulse width T_0 as:

$$\tau = \frac{T}{T_0} = \frac{t - z/v_g}{T_0}. \qquad (2.16)$$

At the same time, we introduce a normalized amplitude U as:

$$A(z,\tau) = \sqrt{P_0}\exp(-\alpha z/2)U(z,\tau), \qquad (2.17)$$

where P_0 is the peak power of the incident pulse. The exponential factor in Eq. (2.17) accounts for fibre losses. By using Eqs. (2.15) – (2.17), $U(z,\tau)$ is found to satisfy:

$$i\frac{\partial U}{\partial z} = \frac{\mathrm{sgn}(\beta_2)}{2L_D}\frac{\partial^2 U}{\partial \tau^2} - \frac{\exp(-\alpha z)}{L_{NL}}|U|^2 U, \qquad (2.18)$$

where $\mathrm{sgn}(\beta_2) = \pm 1$ depending on the sign of the GVD parameter β_2 and

$$L_D = \frac{T_0^2}{|\beta_2|}, \qquad L_{NL} = \frac{1}{\gamma P_0}. \qquad (2.19)$$

The dispersion length L_D and the nonlinear length L_{NL} provide the length scales over which dispersive or nonlinear effects become important for pulse evolution. Depending on the relative magnitudes of L, L_D and L_{NL}, the propagation behaviour can be classified in the following four categories:

(i) When fibre length is such that $L \ll L_{NL}$ and $L \ll L_D$, neither dispersive nor nonlinear effects play a significant role during pulse propagation. This can be seen by noting that both terms on the right hand side of Eq. (2.18) can be

neglected in that case. As a result, $U(z,\tau) = U(0,\tau)$, i.e., the pulse maintains its shape during propagation. The fibre plays a passive role in this regime and acts as a mere transporter of optical pulse.

(ii) When the fibre length is such that $L << L_{NL}$ but $L \sim L_D$, the last term in Eq. (2.18) is negligible compared to the other two. The pulse evolution is then governed by GVD, and the nonlinear effects play a relatively minor role. The effect of GVD on propagation of optical pulse is discussed in this section. The dispersion-dominant regime is applicable whenever the fibre and pulse parameters are such that:

$$\frac{L_D}{L_{NL}} = \frac{\gamma P_0 T_0^2}{|\beta_2|} << 1. \qquad (2.20)$$

(iii) When the fibre length is such that $L << L_D$ but $L \sim L_{NL}$, the dispersion term in Eq. (2.18) is negligible compared to the nonlinear term. In that case, pulse evolution in the fibre is governed by SPM that leads to spectral broadening of the pulse. This phenomenon is considered in the next section. The nonlinear-dominant regime is applicable whenever:

$$\frac{L_D}{L_{NL}} = \frac{\gamma P_0 T_0^2}{|\beta_2|} >> 1. \qquad (2.21)$$

(iv) When the fibre length L is longer or comparable to both L_D and L_{NL}, dispersion and nonlinearity act together as the pulse propagates along the fibre. The

interplay of the GVD and SPM effects can lead to a qualitatively different behaviour compared with that expected from GVD or SPM alone.

2.2.2 Dispersion-induced pulse broadening

The effect of GVD on optical pulses propagating in a linear dispersive medium is studied by setting $\gamma = 0$ in Eq. (2.15). If we define the normalized amplitude $U(z,T)$ according to Eq. (2.17), $U(z,T)$ satisfies the following linear partial differential equation [1]:

$$i\frac{\partial U}{\partial z} = \frac{\beta_2}{2}\frac{\partial^2 U}{\partial T^2}. \qquad (2.22)$$

This equation is similar to the paraxial wave equation that governs diffraction of CW light and becomes identical to it when diffraction occurs in only one transverse direction and β_2 is replaced by $-\lambda/(2\pi)$, where λ is the wavelength of light. For this reason, the dispersion-induced temporal effects have a close analogy with the diffraction-induced spatial effects [3].

Equation (2.22) is readily solved by using the Fourier-transform method. If $\tilde{U}(z,\omega)$ is the Fourier transform of $U(z,T)$ such that:

$$U(z,T) = \frac{1}{2\pi}\int_{-\infty}^{\infty}\tilde{U}(z,\omega)\exp(-i\omega T)d\omega, \qquad (2.23)$$

then it satisfies an ordinary differential equation:

$$i\frac{\partial \tilde{U}}{\partial z} = -\frac{1}{2}\beta_2 \omega^2 \tilde{U}\,, \tag{2.24}$$

whose solution is given by:

$$\tilde{U}(z,\omega) = \tilde{U}(0,\omega)\exp(\frac{i}{2}\beta_2 \omega^2 z)\,. \tag{2.25}$$

Equation (2.25) shows that GVD changes the phase of each spectral component of the pulse by an amount that depends on both the frequency and the propagated distance. Even though such phase changes do not affect the pulse spectrum, they can modify the pulse shape. By substituting Eq. (2.25) in Eq. (2.23), the general solution of Eq. (2.22) is given by:

$$U(z,T) = \frac{1}{2\pi}\int_{-\infty}^{\infty}\tilde{U}(0,\omega)\exp(\frac{i}{2}\beta_2 \omega^2 z - i\omega T)d\omega\,, \tag{2.26}$$

where $\tilde{U}(0,\omega)$ is the Fourier transform of the incident field at $z = 0$ and is obtained using:

$$\tilde{U}(0,\omega) = \int_{-\infty}^{\infty} U(0,T)\exp(i\omega T)dT\,. \tag{2.27}$$

Equations (2.26) and (2.27) can be used for input pulses of arbitrary shapes.

(i) Gaussian pulses

As a simple example, consider the case of a Gaussian pulse for which the incident field is of the form:

$$U(0,T) = \exp(-\frac{T^2}{2T_0^2}), \tag{2.28}$$

where T_0 is the half-width at 1/e-intensity point. In practice, it is customary to use the full width at half maximum (FWHM) in place of T_0. For a Gaussian pulse, the two are related as:

$$T_{FWHM} = 2(\ln 2)^{1/2} T_0 \approx 1.665 T_0 . \tag{2.29}$$

By using Eqs. (2.26) ~ (2.28) and carrying out the integration, the amplitude at any point z along the fibre is given by:

$$U(z,T) = \frac{T_0}{(T_0^2 - i\beta_2 z)^{1/2}} \exp\left(-\frac{T^2}{2(T_0^2 - i\beta_2 z)}\right). \tag{2.30}$$

Thus, a Gaussian pulse maintains its shape on propagation but its width T_1 increases with z as:

$$T_1(z) = T_0[1 + (z/L_D)^2]^{1/2}, \tag{2.31}$$

where the dispersion length $L_D = T_0^2/|\beta_2|$. Equation (2.31) shows how GVD broadens a Gaussian pulse. The extent of broadening is governed by the dispersion length L_D. For a

given fibre length, short pulse broaden more because of a smaller dispersion length. At $z = L_D$, a Gaussian pulse broadens by a factor of $\sqrt{2}$.

A comparison of Eqs. (2.28) and (2.30) shows that although the incident pulse is unchirped (with no phase modulation), the transmitted pulse becomes chirped. This can be seen clearly by writing $U(z,T)$ in the form:

$$U(z,T) = |U(z,T)| \exp[i\phi(z,T)], \tag{2.32}$$

where

$$\phi(z,T) = -\frac{\mathrm{sgn}(\beta_2)(z/L_D)}{1+(z/L_D)^2}\frac{T^2}{T_0^2} + \frac{1}{2}\tan^{-1}\left(\frac{z}{L_D}\right). \tag{2.33}$$

The time dependence of the phase $\phi(z,T)$ implies that the instantaneous frequency differs across the pulse from the central frequency ω_0. The difference $\delta\omega$ is just the time derivative $-\partial\phi/\partial T$ and is given by:

$$\delta\omega(T) = -\frac{\partial\phi}{\partial T} = \frac{\mathrm{sgn}(\beta_2)(2z/L_D)}{1+(z/L_D)^2}\frac{T}{T_0^2}. \tag{2.34}$$

Equation (2.34) shows that the frequency changes linearly across the pulse, i.e., a fibre imposes linear frequency chirp on the pulse. The chirp $\delta\omega$ depends on the sign of β_2. In the normal-dispersion regime ($\beta_2 > 0$), $\delta\omega$ is negative at the leading edge ($T < 0$) and increases linearly across the pulse; the opposite occurs in the anomalous-dispersion regime ($\beta_2 < 0$).

(ii) Super-Gaussian pulses

Dispersion-induced broadening is sensitive to pulse edge steepness. Generally speaking, a pulse with steeper leading and trailing edges broadens more rapidly with propagation simply because such a pulse has a wider spectrum to start with. Pulse emitted by directly modulated semi-conductor lasers fall in this category and cannot generally be approximated by a Gaussian pulse. A super-Gaussian shape can be used to model the effects of steep leading and trailing edges on dispersion-induced pulse broadening. For a super-Gaussian pulse, the incident field can be written as:

$$U(0,T) = \exp\left[-\frac{1+iC}{2}\left(\frac{T}{T_0}\right)^{2m}\right], \tag{2.35}$$

where the parameter m controls the degree of edge sharpness, and C stands for the prechirp. For $m = 1$ we recover the case of Gaussian pulses. For larger value of m, the pulse becomes square shaped with sharper leading and trailing edges. If the rise time T_r is defined as the duration during which the intensity increases from 10 to 90% of its peak value, it is related to the parameter m as:

$$T_r = (\ln 9)\frac{T_0}{2m} \approx \frac{T_0}{m}. \tag{2.36}$$

Thus the parameter m can be determined from the measurements of T_r and T_0.

To see how pulse broadening depends on the steepness of pulse edges, Fig. 2.1 shows the pulse broadening due to the fibre dispersion for the Gaussian pulse ($T_0 = 50$ ps) and super-Gaussian pulse (m=3, $T_0 = 50$ ps), with raised-cosine pulses (rise time of 20, 30, 40, and 50

ps) as reference, after transmissions in SSMF (dispersion parameter: D=17 ps/nm/km or $\beta_2 = -21.68\, ps^2/km$, fibre loss: α=0.2 dB/km) of 50, 100, and 150 km.

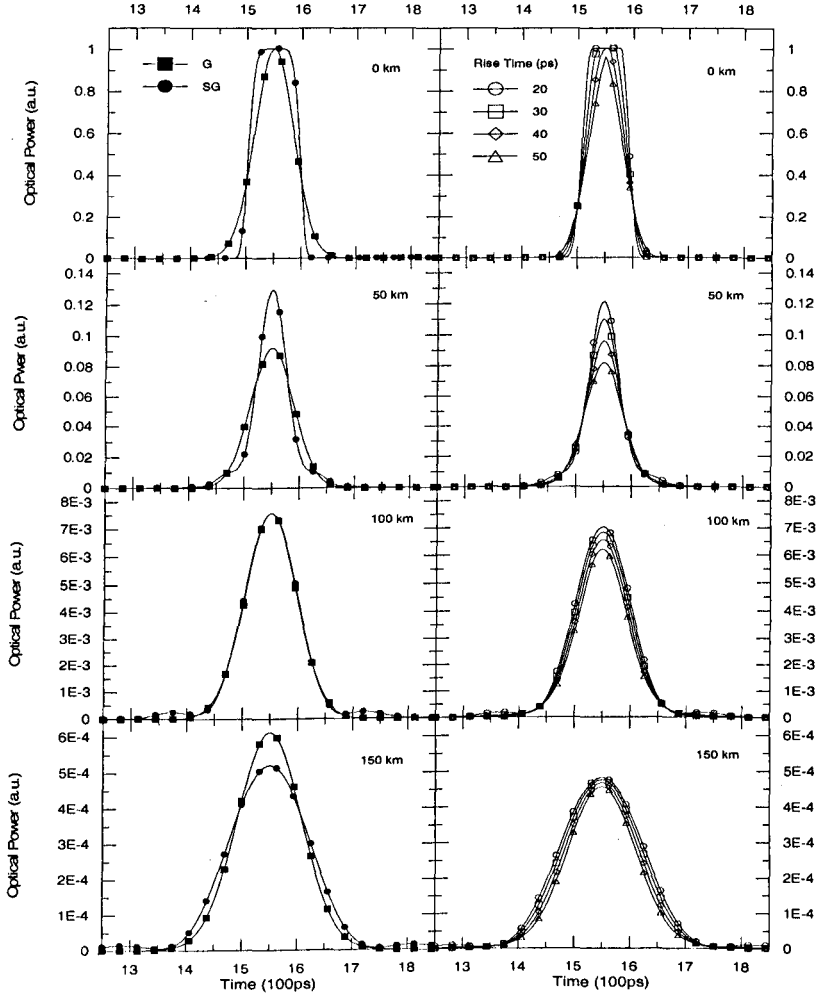

Figure 2.1: Pulse broadening caused by fiber dispersion for Gaussian pulse, super-Gaussian pulse (m=3), and raised-cosine pulse (rise time for 20, 30, 40, and 50 ps) after transmissions in SSMF of 50, 100 and 150 km.

It shows that the Gaussian pulse maintains its shape and its width becomes 54.5, 66.2, and 82.0 ps after 50, 100, and 150 *km* transmissions respectively, the good agreements with Eqs. (2.30) and (2.31). The super-Gaussian pulse not only broadens at a faster rate than the Gaussian pulse but also distorts in shape. For the raised-cosine pulses, it shows that the pulse broadens faster for the shorter rise time and the pulse shapes are also distorted. The significant interference with the neighbouring bits happens after 50 km transmission, the

severe interference after 100 km transmission, and the broadening covered 2-bit width after 150 km transmission.

2.3 Self-phase modulation (SPM)

The intensity dependence of the refractive index in nonlinear optical media, i.e., the Kerr effect, is partially manifested through self-phase modulation (SPM), a phenomenon that leads to spectral broadening of optical pulses. The dispersion leads to pulse broadening and the SPM leads to spectral broadening of optical pulses. A general description of SPM in optical fibres requires numerical solutions of the pulse-propagation equation (2.1). The simpler equation (2.5) can be used for pulse widths $T_0 > 5$ ps. A further simplification occurs if the effect of GVD on SPM is negligible so that the β_2 term in Eq. (2.5) can be set to zero.

2.3.1 SPM-induced spectral broadening

The conditions under which GVD can be ignored were discussed in Section 2.2.1 by introducing the length scales L_D and L_{NL} [see Eq. 2.19]. In general, the pulse width and the peak power should be such that $L_D >> L > L_{NL}$ for a fibre of length L. Equation (2.21) shows that the GVD effects are negligible for relatively wide pulse ($T_0 > 100$ ps) with a large peak power ($P_0 > 1$ W).

In terms of the normalized amplitude $U(z,T)$ defined as in Eq. (2.17), the pulse-propagation equation (2.18), in the limit of $\beta_2 = 0$, becomes:

$$\frac{\partial U}{\partial z} = \frac{ie^{-\alpha z}}{L_{NL}}|U|^2 U, \tag{2.37}$$

which can be solved by substituting $U = V\exp(i\phi_{NL})$ and equating the real and imaginary parts so that:

$$\frac{\partial V}{\partial z} = 0; \qquad \frac{\partial \phi_{NL}}{\partial z} = \frac{e^{-\alpha z}}{L_{NL}}V^2. \tag{2.38}$$

As the amplitude V does not change along the fibre length L, the phase equation can in integrated analytically to obtain the general solution:

$$U(L,T) = U(0,T)\exp[i\phi_{NL}(L,T)], \tag{2.39}$$

where $U(0,T)$ is the field amplitude at $z = 0$ and

$$\phi_{NL}(L,T) = |U(0,T)|^2 (L_{eff} / L_{NL}), \tag{2.40}$$

with the effective length L_{eff} defined as:

$$L_{eff} = [1 - \exp(-\alpha L)]/\alpha. \tag{2.41}$$

Equation (2.39) shows that SPM gives rise to an intensity-dependent phase shift but the pulse shape remains unaffected. The nonlinear phase shift ϕ_{NL} in Eq. (2.40) increases with fibre length L. the quantity L_{eff} plays the role of an effective length that is smaller than L because of fibre losses. In the absence of fibre losses, $\alpha = 0$, and $L_{eff} = L$. The maximum phase shift $\phi_{\max}$ occurs at the pulse centre located at $T = 0$. With U normalized such that $U(0,0) = 1$, it is given by:

$$\phi_{\max} = L_{eff} / L_{NL} = \gamma P_0 L_{eff} . \qquad (2.42)$$

The physical meaning of the nonlinear length L_{NL} is clear from Eq. (2.42): it is the effective prpagation distance at which $\phi_{\max} = 1$. If we use a typical value $\gamma = 2\,\mathrm{W^{-1}km^{-1}}$ in the 1.55-μm wavelength region, $L_{NL} = 50\,\mathrm{km}$ at a power level $P_0 = 10\,\mathrm{mW}$ and decreases inversely with an increase in P_0.

The SPM-induced spectral broadening is a consequence of the time dependence of ϕ_{NL}. This can be understood by noting that a temporally varying phase implies that the instantaneous optical frequency differs across the pulse from its central value ω_0. The difference $\delta\omega$ is given by:

$$\delta\omega(T) = -\frac{\partial \phi_{NL}}{\partial T} = -\left(\frac{L_{eff}}{L_{NL}}\right)\frac{\partial}{\partial T}|U(0,T)|^2 . \qquad (2.43)$$

The time dependence of $\delta\omega$ is referred to as frequency chirping. The chirp induced by SPM increases in magnitude with the propagated distance. In other words, new frequency

components are generated continuously as the pulse propagates down the fibre. These SPM-generated frequency components broaden the spectrum over its initial width at $z = 0$.

The extent of spectral broadening depends on the pulse shape. Consider, for example, the case of a super-Gaussian pulse with the incident field $U(0,T)$ given by Eq. (2.35), the SPM-induced chirp $\delta\omega(T)$ for such a pulse is:

$$\delta\omega(T) = \frac{2m}{T_0}\frac{L_{eff}}{L_{NL}}\left(\frac{T}{T_0}\right)^{2m-1}\exp\left[-\left(\frac{T}{T_0}\right)^{2m}\right], \tag{2.44}$$

where m is the super-Gaussian index. The maximum frequency chirp and its positions are respectively found as:

$$\delta\omega_{\max} = \frac{m}{\pi T_0}\frac{\gamma p_0\left(1-e^{-\alpha z}\right)}{\alpha}\left(\frac{2m-1}{2m}\right)^{\frac{2m-1}{2m}} e^{-\frac{2m-1}{2m}}, \tag{2.45}$$

and

$$T_{\max} = T_0\left(\frac{2m-1}{2m}\right)^{1/2m}. \tag{2.46}$$

Fig. 2.2 shows the SPM-induced frequency chirp for the Gaussian pulse, super-Gaussian pulse, and raised-cosine pulses (rise time of 20 ps and 40 ps) after transmission of 50, 100, 150 km, where the input peak power is 23 dBm, the nonlinear coefficient of fiber is

1.37 $W^{-1}km^{-1}$, and fibre loss is 0.2 dB/km. For the Gaussian and super-Gaussian (m=3) pulses, the maximum frequency chirps are around 15 and 40 GHz respectively after 50 km transmission. The maximum frequency chirp and its position agree with Eqs. (2.45) and (2.46). For raised-cosine pulse, the maximum frequency chirp is around 40 GHz for rise time of 20 ps and 20 GHz for rise time of 40 ps after 50 km transmission. It is found from this figure that the larger maximum frequency chirp happens for the steeper edge of the pulse.

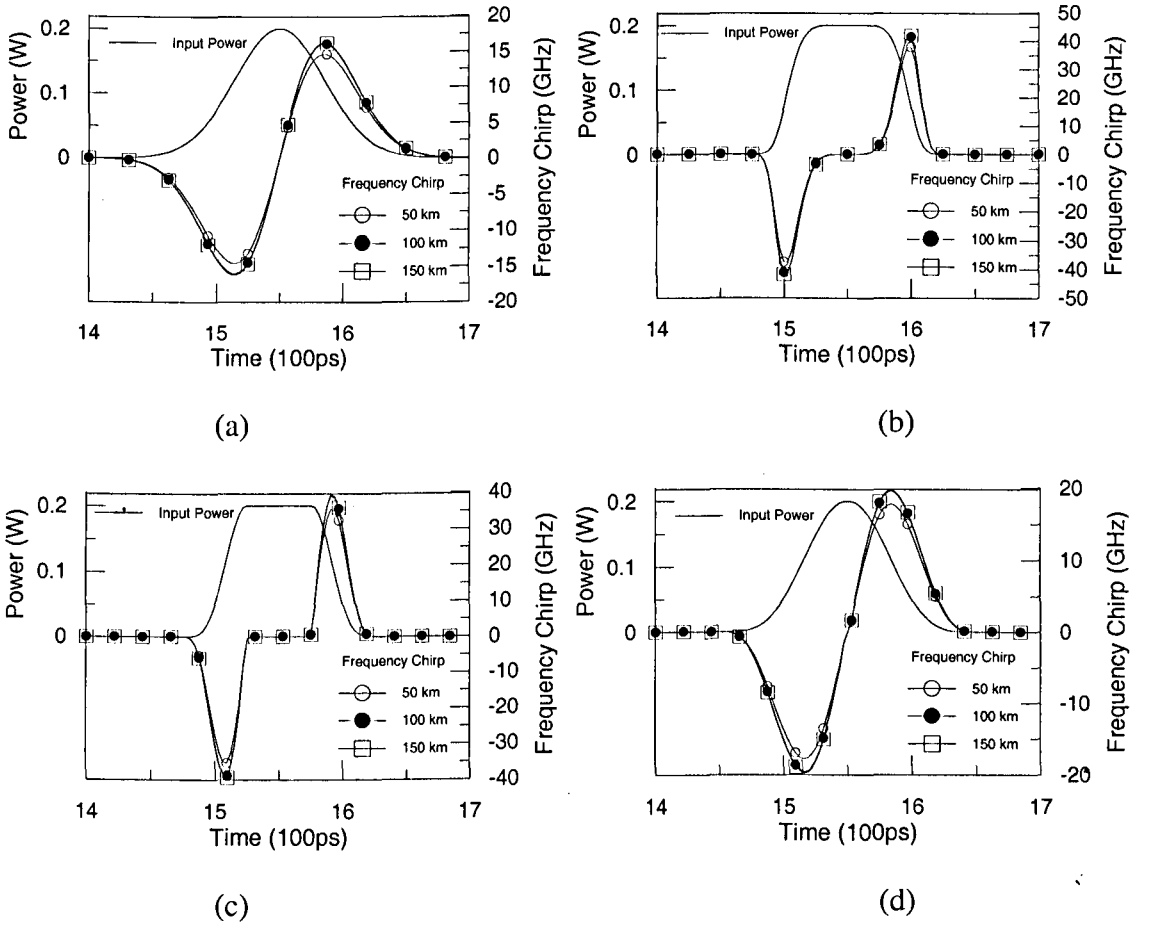

Figure 2.2: SPM-induced frequency chirp for (a). Gaussian pulse, (b). super-Gaussian pulse, and raised-cosine pulse (rise time of (c). 20 ps and (d). 40 ps) after transmission of 50, 100, 150 km.

2.3.2 Interplay between SPM and GVD

The SPM effects discussed in Section 2.3.1 describe the propagation behaviour realistically only for relatively long pulses ($T_0 > 100\,\text{ps}$) for which the dispersion length L_D is much larger compared with both the fibre length L and the nonlinear length L_{NL}. As pulses become shorter and the dispersion length becomes comparable to the fibre length, it becomes necessary to consider the combined effects of GVD and SPM. In the anomalous-dispersion regime of an optical fibre, the two phenomena can cooperate in such a way that the pulse propagates as an optical soliton [1]. In the normal-dispersion regime, the combined effects of GVD and SPM can be used for pulse compression.

The starting point is the NLS equation (2.5) or Eq. (2.18). The later equation can be written in a normalized form as:

$$i\frac{\partial U}{\partial \xi} = \text{sgn}(\beta_2)\frac{1}{2}\frac{\partial^2 U}{\partial \tau^2} - N^2 e^{-\alpha z}|U|^2 U\,, \tag{2.47}$$

where ξ and τ represent the normalized distance and time variables defined as:

$$\xi = z/L_D\,, \qquad \tau = T/T_0\,, \tag{2.48}$$

and the parameter N is introduced by using:

$$N^2 = \frac{L_D}{L_{NL}} \equiv \frac{\gamma P_0 T_0^2}{|\beta_2|}\,. \tag{2.49}$$

As evident from Eq. (2.49), N governs the relative importance of the SPM and GVDeffects on pulse evolution along the fibre. Dispersion dominates for $N << 1$ while SPM dominates for $N >> 1$. For values of $N \sim 1$, both SPM and GVD play an equally important role during pulse evolution. In Eq. (2.47), $\text{sgn}(\beta_2) = \pm 1$ depending on whether GVD is normal ($\beta_2 > 0$) or anomalous ($\beta_2 < 0$). The split-step Fourier method of Section 2.1.2 can be used to solve Eq. (2.47) numerically.

For the case of $N \sim 1$, in the normal-dispersion regime, the pulse broadens much more rapidly compared with the $N = 0$ case (no SPM). This can be understood by noting that SPM generates new frequency components that are red-shifted near the leading edge and blue-shifted near the trailing edge of the pulse. As the red components travel faster than the blue components in the normal-dispersion regime, SPM leads to an enhanced rate of pulse broadening compared with that expected from GVD alone. This in turn affects spectral broadening as the SPM-induced phase shift ϕ_{NL} becomes less than that occurring if the pulse shape were to remain unchanged.

The situation is different for pulses propagating in the anomalous-dispersion regime of the fibre. The pulse broadens initially at a rate much lower than that expected in the absence of SPM and then appears to reach a steady state for $z > 4L_D$. At the same time, the spectrum narrows rather than exhibiting broadening expected by SPM in the absence of GVD. This behaviour can be understood by noting the SPM-induced chirp given by Eq. (2.44) is positive while the dispersion-induced chirp given by Eq. (2.34) is negative for $\beta_2 < 0$. The two chirp contributions nearly cancel each other along the centre portion of the Gaussian

pulse when $L_D = L_{NL}(N=1)$. Pulse shape adjusts itself during propagation to make such cancellation as complete as possible. Thus, GVD and SPM cooperate with each other to maintain a chirp-free pulse.

2.3.3 Higher-order nonlinear effects

The discussion of SPM so far is based on the simplified propagation equation (2.5). For ultrashort optical pulse ($T_0 < 1$ ps), it is necessary to include the higher-order nonlinear effects through Eq. (2.1). If Eq. (2.17) is used to define the normalized amplitude U, this equation takes the form:

$$\frac{\partial U}{\partial z} + i\frac{\mathrm{sgn}(\beta_2)}{2L_D}\frac{\partial^2 U}{\partial \tau^2} = \frac{\mathrm{sgn}(\beta_3)}{6L_D'}\frac{\partial^3 U}{\partial \tau^3} + i\frac{e^{-\alpha z}}{L_{NL}}\left(|U|^2 U + is\frac{\partial}{\partial \tau}(|U|^2 U) - \tau_R U\frac{\partial |U|^2}{\partial \tau}\right) \tag{2.50}$$

where L_D, L_D' and L_{NL} are the three length scales defined as:

$$L_D = \frac{T_0^2}{|\beta_2|}, \qquad L_D' = \frac{T_0^3}{|\beta_3|}, \qquad L_{NL} = \frac{1}{\gamma P_0}. \tag{2.51}$$

The parameters s and τ_R govern the effects of self-steeping and intrapulse Raman scattering, respectively, and are defined as:

$$s = \frac{1}{\omega_0 T_0}, \qquad \tau_R = \frac{T_R}{T_0}. \tag{2.52}$$

Both of these effects are quite small for picosecond pulses but must be considered for ultrashort pulses with $T_0 < 0.1\,\text{ps}$.

Before solving Eq. (2.50) numerically, it is instructive to consider the dispersionless case by setting $\beta_2 = \beta_3 = 0$. Equation (2.50) can be solved analytically in this specific case if we also set $\tau_R = 0$. Defining a normalized distance as $Z = z/L_{NL}$ and neglecting fibre losses ($\alpha = 0$), Eq. (2.50) becomes:

$$\frac{\partial U}{\partial Z} + s\frac{\partial}{\partial \tau}(|U|^2 U) = i|U|^2 U\,. \tag{2.53}$$

Using $U = \sqrt{I}\exp(i\phi)$ in Eq. (2.53) and separating the real and imaginary parts. We obtain the following two equations:

$$\frac{\partial I}{\partial Z} + 3sI\frac{\partial I}{\partial \tau} = 0, \tag{2.54}$$

$$\frac{\partial \phi}{\partial Z} + sI\frac{\partial \phi}{\partial \tau} = I\,. \tag{2.55}$$

Since the intensity equation (2.54) is decoupled from the phase equation (2.55), it can be solved easily using the method of characteristics. Its general solution is given by:

$$I(Z,\tau) = f(\tau - 3sIZ), \tag{2.56}$$

where we used the initial condition $I(0,\tau) = f(\tau)$, where $f(\tau)$ describes the pulse shape at $z = 0$. Equation (2.56) shows that each point τ moves along a straight line from its initial value, and the slope of the line is intensity dependent. This feature leads to pulse distortion. As an example, consider the case of a Gaussian pulse for which:

$$I(0,\tau) = f(\tau) = \exp(-\tau^2). \tag{2.57}$$

From Eq. (2.56), the pulse shape at a distance Z is obtained by using:

$$I(Z,\tau) = \exp[-(\tau - 3sIZ)^2]. \tag{2.58}$$

The implicit relation for $I(Z,\tau)$ should be solved for each τ to obtain the pulse shape at a given value of Z.

Self-steepening of the pulse eventually creates an optical shock, analogous to the development of an acoustic shock on the leading edge of a sound wave. The distance at which the shock is formed is obtained from Eq. (2.58) by requiring that $\partial I / \partial \tau$ be infinite at the shock location. It is given by:

$$z_s = \left(\frac{e}{2}\right)^{1/2} \frac{L_{NL}}{3s} \approx 0.39(L_{NL}/s). \tag{2.59}$$

Self-steepening also affects SPM-induced spectral broadening. In the dispersionless case, $\phi(z,\tau)$ is obtained by solving Eq. (2.55). It can then be used to calculate the spectrum using:

$$S(\omega)=\left|\int_{-\infty}^{\infty}[I(z,\tau)]^{1/2}\exp[i\phi(z,\tau)+i(\omega-\omega_0)\tau]d\tau\right|^2. \qquad (2.60)$$

2.4 Cross-phase modulation (XPM)

When two or more optical fields having different wavelengths propagate simultaneously inside a fibre, they interact with each other through the fibre nonlinearity. In general, such an interaction can generate new waves under appropriate conditions through a variety of nonlinear phenomena such as stimulated Raman or Brillouin scattering, harmonic generation, and four-wave mixing. The fibre nonlinearity can also couple two fields through cross-phase modulation (XPM) without including any energy transfer between them. XPM is always accompanied by SPM and occurs because the effective refractive index seen by an optical beam in a nonlinear medium depends not only on the intensity of that beam but also on the intensity of other co-propagating beams.

2.4.1 Nonlinear refractive index

In the quasi-monochromatic approximation, it is useful to separate the rapidly varying part of the electric field by writing it in the form:

$$\mathbf{E}(\mathbf{r},t)=\frac{1}{2}\hat{x}[E_1\exp(-i\omega_1 t)+E_2\exp(-i\omega_2 t)]+\text{c.c.}, \qquad (2.61)$$

where $\hat{x}$ is the polatization unit vector, ω_1 and ω_2 are the carrier frequencies of the two pulses, and the corresponding amplitudes E_1 and E_2 are assumed to be slowly varying functions of time compared with an optical period. This assumption is equivalent to assuming that the spectral width of each pulse satisfies the condition $\Delta\omega_j << \omega_j (j = 1, 2)$, and holds quite well for pulse widths >0.1 ps.

To see the origin of XPM, the nonlinear polarization can be written as:

$$\begin{aligned}\mathbf{P}_{NL}(\mathbf{r},t) = \frac{1}{2}\hat{x}[&P_{NL}(\omega_1)\exp(-i\omega_1 t) + P_{NL}(\omega_2)\exp(-i\omega_2 t) \\ &+ P_{NL}(2\omega_1 - \omega_2)\exp[-i(2\omega_1 - \omega_2)t] \\ &+ P_{NL}(2\omega_2 - \omega_1)\exp[-i(2\omega_2 - \omega_1)t] + \text{c.c.},\end{aligned} \tag{2.62}$$

where the four terms depend on E_1 and E_2 as:

$$P_{NL}(\omega_1) = \chi_{eff}(|E_1|^2 + 2|E_2|^2)E_1, \tag{2.63}$$

$$P_{NL}(\omega_2) = \chi_{eff}(|E_2|^2 + 2|E_1|^2)E_2, \tag{2.64}$$

$$P_{NL}(2\omega_1 - \omega_2) = \chi_{eff} E_1^2 E_2^*, \tag{2.65}$$

$$P_{NL}(2\omega_2 - \omega_1) = \chi_{eff} E_2^2 E_1^*, \tag{2.66}$$

where $\chi_{eff} = (3\varepsilon_0/4)\chi^{(3)}_{xxxx}$ acting as an effective nonlinear parameter.

The induced nonlinear polarization in Eq. (2.62) has terms oscillating at the new frequencies $2\omega_1 - \omega_2$ and $2\omega_2 - \omega_1$. These terms result from the phenomenon of four-

wave mixing discussed in the next section. It is necessary to satisfy the phase-matching condition if the new frequency components are to build up significantly, a condition not generally satisfied in practice unless special precautions are taken. The FWM terms are neglected in this section after assuming that phase matching does not occur. The remaining two terms provide a nonlinear contribution to the refractive index. This can be seen writing $P_{NL}(\omega_j)$ in the form ($j = 1, 2$):

$$P_{NL}(\omega_j) = \varepsilon_0 \varepsilon_j^{NL} E_j, \tag{2.67}$$

and combining it with the linear part so that the total induced polarization is given by:

$$P(\omega_j) = \varepsilon_0 \varepsilon_j E_j, \tag{2.68}$$

where

$$\varepsilon_j = \varepsilon_j^L + \varepsilon_j^{NL} = (n_j^L + \Delta n_j)^2, \tag{2.69}$$

n_j^L is the linear part of the refractive index and Δn_j is the change induced by the third-order nonlinear effects. Using the approximation $\Delta n_j << n_j^L$, the nonlinear part of the refractive index is given by:

$$\Delta n_j \approx \varepsilon_j^{NL} / 2n_j \approx n_2(|E_j|^2 + 2|E_{3-j}|^2), \tag{2.70}$$

where $n_1^L \approx n_2^L = n$ has been assumed. The nonlinear parameter n_2 is defined as:

$$n_2 = \frac{3}{8n}\mathrm{Re}(\chi^{(3)}_{xxxx}). \tag{2.71}$$

Equation (2.70) shows that the refractive index seen by an optical field inside an optical fibre depends not only on the intensity of that field but also on the intensity of other copropagating fields. As the optical field propagates inside the fibre, it acquires an intensity-dependent nonlinear phase shift:

$$\phi_j^{NL}(z) = (\omega_j / c)\Delta n_j z = n_2(\omega_j / c)(|E_j|^2 + 2|E_{3-j}|^2)z, \tag{2.72}$$

where $j = 1$ or 2. The first term is responsible for SPM. The second term results from phase modulation of one wave by the copropagating wave and is responsible for XPM. The factor of 2 on the right-hand side of Eq. (2.72) shows that XPM is twice as SPM for the same intensity.

2.4.2 Coupled NLS equations

Assuming that the nonlinear effects do not affect significantly the fibre modes, the transverse dependence can be factored out writing $\mathbf{E}_j(\mathbf{r},t)$ in the form:

$$\mathbf{E}_j(\mathbf{r},t) = F_j(x,y)A_j(z,t)\exp(i\beta_{0j}z), \tag{2.73}$$

where $F_j(x,y)$ is the transverse distribution of the fibre mode for the j-th field (j = 1, 2), $A_j(z,t)$ is the slowly varying amplitude, and β_{0j} is the corresponding propagation constant at the carrier frequency ω_j. The dispersive effects are included by expanding the frequency-dependent propagation constant $\beta_j(\omega)$ for each wave and retaining only up to the quadratic term. The resulting propagation equation for $A_j(z,t)$ becomes:

$$\frac{\partial A_j}{\partial z}+\beta_{1j}\frac{\partial A_j}{\partial t}+\frac{i\beta_{2j}}{2}\frac{\partial^2 A_j}{\partial t^2}+\frac{\alpha_j}{2}A_j = in_2(\omega_j/c)(f_{jj}|A_j|^2+2f_{jk}|A_k|^2) \tag{2.74}$$

where $k \neq j$, $\beta_{1j}=1/v_{gj}$, v_{gj} is the group velocity, β_{2j} is the GVD coefficient, and α_j is the loss coefficient. The overlap integral f_{jk} is defined as:

$$f_{jk}=\frac{\iint_{-\infty}^{\infty}|F_j(x,y)|^2|F_k(x,y)|^2\,dxdy}{\left(\iint_{-\infty}^{\infty}|F_j(x,y)|^2\,dxdy\right)\left(\iint_{-\infty}^{\infty}|F_k(x,y)|^2\,dxdy\right)}. \tag{2.75}$$

The differences among the overlap integrals can be significant in multi-mode fibres if the two waves propagate in different fibre modes. Even in single-mode fibres, f_{12}, f_{22} and f_{21} differ from each other because of the frequency dependence of the modal distribution $F_j(x,y)$. The difference is small, however, and can be neglected in practice. In that case, Eq. (2.74) can be written as the following set of two coupled NLS equations [4, 5]:

$$\frac{\partial A_1}{\partial z}+\frac{1}{v_{g1}}\frac{\partial A_1}{\partial t}+\frac{i\beta_{21}}{2}\frac{\partial^2 A_1}{\partial t^2}+\frac{\alpha_1}{2}A_1 = i\gamma_1(|A_1|^2+2|A_2|^2)A_1, \tag{2.76}$$

$$\frac{\partial A_2}{\partial z}+\frac{1}{v_{g2}}\frac{\partial A_2}{\partial t}+\frac{i\beta_{22}}{2}\frac{\partial^2 A_2}{\partial t^2}+\frac{\alpha_2}{2}A_2=i\gamma_2(|A_2|^2+2|A_1|^2)A_2, \qquad (2.77)$$

where the nonlinear parameter is defined as (j = 1, 2):

$$\gamma_j=n_2\omega_j/(cA_{eff}), \qquad (2.78)$$

and A_{eff} is the effective core area ($A_{eff}=1/f_{11}$), assumed to be the same for both optical waves. Typically $A_{eff}=50\mu m^2$ in the 1.55-μm wavelength region. The corresponding values of γ_1 and γ_2 are $\sim 1W^{-1}/km$ depending on the frequencies ω_1 and ω_2. Generally, the two pulses not only have different GVD coefficients but also propagate at different speeds because of the difference in their group velocities. The group-velocity mismatch plays an important role as it limits the XPM interaction as pulses walk off from each other. One can define the walk-off length L_W, as a measure of the fibre length during which two overlapping pulses separate from each other as a result of the group-velocity mismatch.

In a birefringent fibre, the state of polarization of both wave changes with propagation. The orthogonally polarized components of each wave are then mutually coupled through XPM. The total optical field can be written as:

$$\mathbf{E}(\mathbf{r},t)=\frac{1}{2}\left[(\hat{x}E_{1x}+\hat{y}E_{1y})e^{-i\omega_1 t}+(\hat{x}E_{2x}+\hat{y}E_{2y})e^{-i\omega_2 t}\right]+\text{c.c.}. \qquad (2.79)$$

The slowly varying amplitudes A_{1x}, A_{1y}, A_{2x} and A_{2y} can be introduced similarly to Eq. (2.73) and the coupled amplitude equations for them are obtained by following the same method. These equations are quite complicated in the general case that includes the coherent-couplings terms. However, they are considerably simplified in the case of high-birefringence fibres because such terms can then be neglected. The resulting set of four coupled NLS equations becomes [6]:

$$\frac{\partial A_{1p}}{\partial z}+\frac{1}{v_{g1p}}\frac{\partial A_{1p}}{\partial t}+\frac{i\beta_{21}}{2}\frac{\partial^2 A_{1p}}{\partial t^2}+\frac{\alpha_1}{2}A_{1p} = i\gamma_1\left(\left|A_{1p}\right|^2+2\left|A_{2p}\right|^2+B\left|A_{1q}\right|^2+B\left|A_{2q}\right|^2\right)A_{1p}, \tag{2.80}$$

$$\frac{\partial A_{2p}}{\partial z}+\frac{1}{v_{g2p}}\frac{\partial A_{2p}}{\partial t}+\frac{i\beta_{22}}{2}\frac{\partial^2 A_{2p}}{\partial t^2}+\frac{\alpha_2}{2}A_{2p} = i\gamma_2\left(\left|A_{2p}\right|^2+2\left|A_{1p}\right|^2+B\left|A_{1q}\right|^2+B\left|A_{2q}\right|^2\right)A_{2p}, \tag{2.81}$$

where $p = x, y$ and $q = x, y$ such that $p \neq q$. The parameter B is defined as:

$$B=\frac{2+2\sin^2\theta}{2+\cos^2\theta}, \tag{2.82}$$

where θ is the ellipticity angle. B equals 2/3 for linearly birefringent fibres. Equations (2.80) and (2.81) reduce to Eqs. (2.76) and (2.77) when both waves are polarized along a principal axis ($A_{1y} = A_{2y} = 0$).

2.5 Four-wave mixing (FWM)

2.5.1 Coupled amplitude equations

Four-wave mixing (FWM) transfers energy from a strong pump wave to two sideband waves, upshifted and downshifted in frequency from the pump frequency. Consider four optical waves oscillating at frequencies ω_1, ω_2, ω_3, and ω_4 and linearly polarized along the same axis x. The total electric field can be written as:

$$\mathbf{E} = \frac{1}{2}\hat{x}\sum_{j=1}^{4} E_j \exp[i(k_j z - \omega_j t)] + \text{c.c.}, \tag{2.83}$$

where the propagation constant $k_j = n_j\omega_j / c$, n_j is the refractive index, and all four waves are assured to be propagating in the same direction. The induced nonlinear polarization can be given as:

$$\mathbf{P}_{NL} = \frac{1}{2}\hat{x}\sum_{j=1}^{4} P_j \exp[i(k_j z - \omega_j t)] + \text{c.c.}, \tag{2.84}$$

we find that P_j (j = 1 to 4) consists of a large number of terms involving the products of three electric fields. For example, P_4 can be expressed as:

$$\begin{aligned} P_4 = \frac{3\varepsilon_0}{4}\chi^{(3)}_{xxxx}\Big[&|E_4|^2 E_4 + 2\left(|E_1|^2 + |E_2|^2 + |E_3|^2\right)E_4 \\ &+ 2E_1E_2E_3\exp(i\theta_+) + 2E_1E_2E_3^*\exp(i\theta_-) + \cdots\Big] \end{aligned} \tag{2.85}$$

where θ_+ and θ_- are defined as:

$$\theta_+ = (k_1 + k_2 + k_3 - k_4)z - (\omega_1 + \omega_2 + \omega_3 - \omega_4)t\,, \tag{2.86}$$

$$\theta_- = (k_1 + k_2 - k_3 - k_4)z - (\omega_1 + \omega_2 - \omega_3 - \omega_4)t\,. \tag{2.87}$$

The first four terms containing E_4 in Eq. (2.85) are responsible for the SPM and XPM effects. The remaining terms result from FWM. How many of these are effective in producing a parametric coupling depends on the phase mismatch between E_4 and P_4 governed by θ_+ and θ_-, or a similar quantity.

Significant FWM occurs only if the phase mismatch nearly vanishes. There are two types of FWM terms in Eq. (2.85). The term containing θ_+ corresponds to the case in which three photons transfer their energy to a single photon at the frequency $\omega_4 = \omega_1 + \omega_2 + \omega_3$. This term is responsible for the phenomena such as third-harmonic generation ($\omega_1 = \omega_2 = \omega_3$), or frequency conversion when $\omega_1 = \omega_2 \neq \omega_3$. In general, it is difficult to satisfy the phase-matching condition for such processes to occur in optical fibres with high efficiencies. The term containing θ_- in Eq. (2.85) corresponds to the case in which two photons at frequencies ω_1 and ω_2 are annihilated with simultaneous creation of two photons at frequencies ω_3 and ω_4 such that:

$$\omega_3 + \omega_4 = \omega_1 + \omega_2\,. \tag{2.88}$$

The phase-matching requirement for this process to occur is:

$$\begin{aligned}\Delta k &= k_3 + k_4 - k_1 - k_2 \\ &= (n_3\omega_3 + n_4\omega_4 - n_1\omega_1 - n_2\omega_2)/c = 0.\end{aligned} \tag{2.89}$$

It is relatively easy to satisfy $\Delta k = 0$ in the specific case $\omega_1 = \omega_2$. This partially degenerate case is most relevant for optical fibres. A strong pump wave at ω_1 creates two sidebands located symmetrically at frequencies ω_3 and ω_4 with a frequency shift:

$$\Omega_s = \omega_1 - \omega_3 = \omega_4 - \omega_1, \tag{2.90}$$

where we assumed for definiteness $\omega_3 < \omega_4$. The low-frequency sideband at ω_3 and the high-frequency sideband at ω_4 are referred to as the Stokes and anti-Stokes bands.

If only the pump wave is incident at the fibre, and the phase-matching condition is satisfied, the Stokes and anti-Stokes waves at the frequency ω_3 and ω_4 can be generated from noise by the stimulated scattering processes. On the other hand, if a weak signal at ω_3 is also launched into the fibre together with the pump, the signal is amplified while a new wave at ω_4 is generated simultaneously. The gain responsible for such amplification is called the parametric gain.

We substitutes Eqs. (2.83) and (2.84) in the wave equation, together with a similar expression for the linear part of the polarization, and neglect the time dependence of the field components E_j (j = 1 to 4) assuming quasi-CW conditions. Their spatial dependence is included using:

$$E_j(\mathbf{r}) = F_j(x,y)A_j(z), \tag{2.91}$$

where $F_j(x,y)$ is the spatial distribution of the fibre mode in which the j-th field propagates inside the fibre. Evolution of the amplitude $A_j(z)$ inside a multimode fibre is governed by a set of four coupled equations which, in the paraxial approximation, can be written as:

$$\frac{dA_1}{dz} = \frac{in_2'\omega_1}{c}\left[(f_{11}|A_1|^2 + 2\sum_{k\neq 1} f_{1k}|A_k|^2)A_1 + 2f_{1234}A_2^* A_3 A_4 e^{i\Delta kz}\right], \tag{2.92}$$

$$\frac{dA_2}{dz} = \frac{in_2'\omega_2}{c}\left[(f_{22}|A_2|^2 + 2\sum_{k\neq 2} f_{2k}|A_k|^2)A_2 + 2f_{2134}A_1^* A_3 A_4 e^{i\Delta kz}\right], \tag{2.93}$$

$$\frac{dA_3}{dz} = \frac{in_2'\omega_3}{c}\left[(f_{33}|A_3|^2 + 2\sum_{k\neq 3} f_{3k}|A_k|^2)A_3 + 2f_{3412}A_1 A_2 A_4^* e^{i\Delta kz}\right], \tag{2.94}$$

$$\frac{dA_4}{dz} = \frac{in_2'\omega_4}{c}\left[(f_{44}|A_4|^2 + 2\sum_{k\neq 4} f_{4k}|A_k|^2)A_4 + 2f_{4312}A_1 A_2 A_3^* e^{i\Delta kz}\right], \tag{2.95}$$

where the wave-vector mismatch Δk is given by:

$$\Delta k = (\tilde{n}_3\omega_3 + \tilde{n}_4\omega_4 - \tilde{n}_1\omega_1 - \tilde{n}_2\omega_2)/c. \tag{2.96}$$

The refractive indices $\tilde{n}_1$ to $\tilde{n}_4$ stand for the effective indices of the fibre modes. Note that $\tilde{n}_1$ and $\tilde{n}_2$ can differ from each other when the pump waves A_1 and A_2 propagate in different fibre modes even if they are degenerate in frequencies. The overlap integral f_{ijkl} is given by:

$$f_{ijkl} = \frac{\left\langle F_i^* F_j^* F_k F_l \right\rangle}{\left[\left\langle |F_i|^2 \right\rangle \left\langle |F_j|^2 \right\rangle \left\langle |F_k|^2 \right\rangle \left\langle |F_l|^2 \right\rangle \right]^{1/2}} \tag{2.97}$$

where angle brackets denote integration over the transverse coordinates x and y.

2.5.2 Approximate solution

Equations (2.92)–(2.95) are quite general in the sense that they include the effects of SPM, XPM, and pump depletion on the FWM process; a numerical approach is necessary to solve them exactly. Considerable physical insight is gained if the pump waves are assumed to be much intense compared with the Stokes and anti-Stokes waves and to remain undepleted during the parametric interaction. As a further simplification, we assume that all overlap integrals are nearly the same, that is:

$$f_{ijkl} \approx f_{ij} \approx 1/A_{eff} \qquad (i, j = 1, 2, 3, 4), \tag{2.98}$$

where A_{eff} is the effective core area. This assumption is valid for single-mode fibres. The analysis can easily be extended to include differences in the overlap integrals.

We can now introduce the nonlinear parameter γ_j using the definition:

$$\gamma_j = n_2' \omega_j / (cA_{eff}) \approx \gamma, \tag{2.99}$$

where γ is an average value if we ignore relatively small differences in optical frequencies of four waves. Equations (2.92) and (2.93) for the pump fields are easily solved to obtain:

$$A_1(z) = \sqrt{P_1}\exp[i\gamma(P_1 + 2P_2)z], \tag{2.100}$$

$$A_2(z) = \sqrt{P_2}\exp[i\gamma(P_2 + 2P_1)z], \tag{2.101}$$

where $P_j = |A_j(0)|^2$, and P_1 and P_2 are the incident pump powers at $z = 0$. This solution shows that, in the undepleted-pump approximation, the pump waves only acquire a phase shift occurring as a result of SPM and XPM.

Substituting Eqs. (2.100) and (2.101) in Eqs. (2.94) and (2.95), we obtain two linear coupled equations for the signal and idler fields:

$$\frac{dA_3}{dz} = 2i\gamma[(P_1 + P_2)A_3 + \sqrt{P_1P_2}e^{-i\theta}A_4^*], \tag{2.102}$$

$$\frac{dA_4^*}{dz} = -2i\gamma[(P_1 + P_2)A_4^* + \sqrt{P_1P_2}e^{-i\theta}A_3], \tag{2.103}$$

where:

$$\theta = [\Delta k - 3\gamma(P_1 + P_2)]z. \tag{2.104}$$

To solve these equations, we introduce:

$$B_j = A_j\exp[-2i\gamma(P_1 + P_2)z], \quad (j = 3, 4). \tag{2.105}$$

Using Eqs. (2.102)–(2.105), we then obtain:

$$\frac{dB_3}{dz} = 2i\gamma\sqrt{P_1P_2}\exp(-i\kappa z)B_4^*, \tag{2.106}$$

$$\frac{dB_4^*}{dz} = -2i\gamma\sqrt{P_1P_2}\exp(i\kappa z)B_3, \tag{2.107}$$

where the net phase mismatch is given by:

$$\kappa = \Delta k + \gamma(P_1 + P_2). \tag{2.108}$$

Equations (2.106) and (2.107) govern growth of the signal and idler waves occurring as a result of FWM. Their general solution is of the form:

$$B_3(z) = (a_3e^{gz} + b_3e^{-gz})\exp(-i\kappa z/2), \tag{2.109}$$

$$B_4^*(z) = (a_4e^{gz} + b_4e^{-gz})\exp(-i\kappa z/2), \tag{2.110}$$

where a_3, b_3, a_4 and b_4 are determined from the boundary conditions. The parametric gain g depends on the pump power and is defined as:

$$g = \sqrt{(\gamma P_0 r)^2 - (\kappa/2)^2}, \tag{2.111}$$

where we have introduced the parameters r and P_0 as:

$$r = 2(P_1P_2)^{1/2}/P_0, \qquad P_0 = P_1 + P_2. \tag{2.112}$$

The solution given by Eqs. (2.109) and (2.110) is valid only when the conversion efficiency of the FWM process is relatively small so that the pump waves remain largely undepleted. Pump depletion can be included by solving the complete set of four equations (2.92)–(2.95).

2.6 Stimulated Brillouin scattering (SBS)

The high transmitter power is required for long distance WDM optical fibre transmission. When high transmitter power is launched into an optical fibre, a nonlinear effect, i.e. Stimulated Brillouin scattering (SBS), causes most of the launched power to be reflected back towards the transmitter, once the Brillouin threshold is reached, causing a severe degradation of the optical pulses at the receiver.

The attention has been focused upon the consequences of the SBS effect in long distance WDM transmission systems because of the uses of high power and narrowband transmitters (high transmitter power input compensates the fibre loss and narrowband transmitter reduces the effect of fibre dispersion). In this section, the analytical model for SBS effect is described. The Brillouin gain and SBS threshold are given for both CW and modulated pump. The methods to increase SBS threshold and suppress the SBS are also summarised.

When low transmitter power launched into an optical fibre, the reflected and transmitted power increases linearly with the transmitter power, in which the ratio between transmitter power and reflected/transmitted powers are determined by the Rayleigh backscattering coefficient and fibre loss. If the transmitter power is increased above a certain level (the

SBS threshold), SBS occurs in the fibre, i.e. the reflected power is increasing rapidly, whereas the transmitted power is flattening off. This is because most of the input light is converted into the backward-travelling Stokes light during optical transmission. As a result, the forward-travelling input (signal) light suffers additional nonlinear loss.

The process of SBS can be described classically as a parametric interaction among the pump wave, the Stokes wave, and an acoustic wave. The pump wave generates acoustic waves through the process of electrostriction which in turn causes a periodic modulation of the refractive index. The pump-induced index grating scatters the pump light through Bragg diffraction. The scattered light is downshifted in frequency because of the Doppler shift associated with a grating moving at the acoustic velocity v_A. This frequency shift is given by [1, 7]:

$$\omega_B = \frac{2n_0 v_A}{\lambda}, \tag{2.113}$$

where n_0 is the fibre refractive index and λ is the wavelength of the pump. Taking the following values for fused silica: $v_A = 5960 ms^{-1}$, $\lambda = 1550 nm$, $n_0 = 1.44$ gives $\omega_B = 11.1 GHz$ [7].

The pump wave I_P and the backscattered Stokes wave I_S can be described by the two coupled differential equations [1]:

$$\frac{dI_S}{dz} = -G_B(\omega) I_P I_S + \alpha I_S, \tag{2.114}$$

$$\frac{dI_P}{dz} = -G_B(\omega) I_P I_S + \alpha I_P , \qquad (2.115)$$

where I_P and I_S are the intensity of the pump and Stokes wave respectively, α is the fibre loss, and $G_B(\omega)$ is the Brillouin gain coefficient which is given by [1, 8]:

$$G_B(\omega) = G_{BGP}(\omega) g_B , \qquad (2.116)$$

where $G_{BGP}(\omega)$ is the Brillouin gain profile, and g_B is the peak value of the Brillouin gain coefficient occurring at $\omega = \omega_B$ which is given by [1]:

$$g_B = \frac{2\pi n_0^7 p_{12}^2}{c\lambda^2 \rho v_A \Delta\omega_B} , \qquad (2.117)$$

where p_{12} is the longitudinal elasto-optic coefficient ($p_{12} = 0.286$ for fused silica [7]), c is light velocity in vacuum, ρ is material density ($\rho = 2.21 \times 10^3 kg.m^{-3}$ for fused silica [7]), and $\Delta\omega_B$ is the Brillouin linewidth (FWHM) which is related to the acoustic phonon lifetime by [7]:

$$\Delta\omega_B = \Gamma/\pi \text{ (FWHM).} \qquad (2.118)$$

The Brillouin linewidth depends on the intrinsic physical parameters of the medium. For fused silica $\Delta\omega_B$ is found to be 16 MHz at wavelength λ =1550 nm [7]. Taking the previous parameter values g_B is found to be $4.3 \times 10^{-11} m/W$.

By solving the coupled differential equations (2.114) and (2.115), the Stokes intensity $I_S(\omega_S, z)$ at z in the fibre is found to grow exponentially in the backward direction according to the following relation [8, 9]:

$$I_S(\omega_S, z) = I_S(\omega_S, L)\exp\left\{\frac{\pi g_B p_0 L_{eff} \Delta\omega_B}{2A_{eff}} \int_{-\infty}^{+\infty} G_{BGP}(\omega_S + \omega_A - \omega) P_{PS}(\omega) d\omega - \alpha L\right\}, \quad (2.119)$$

where p_0 is the signal (pump) power, A_{eff} is the effective core area of fibre, $P_{PS}(\omega)$ is the modulated LD (pump) spectrum, L is the fibre length, and L_{eff} is the effective length which is defined as:

$$L_{eff} = \frac{1 - \exp(-\alpha L)}{\alpha}. \quad (2.120)$$

The Brillouin gain $G(\omega)$, which is defined by $I_S(0) = I_S(L)\exp(G - \alpha L)$, along a fibre of length L is given by [1, 8, 9]:

$$G(\omega_S) = \frac{\pi g_B p_0 L_{eff} \Delta\omega_B}{2A_{eff}} \int_{-\infty}^{+\infty} G_{BGP}(\omega_S + \omega_A - \omega) P_{PS}(\omega) d\omega. \quad (2.121)$$

Assuming that the power spectrum density (PSD) of the modulated LD signal, $P_{PS}(\omega)$, can be expressed as the convolution integral between the PSD of the signal, $S(\omega)$, normalised by the power of the carrier, with negligible linewidth and the spectral profile of the LD, $G_{LDSP}(\omega)$, we have:

$$P_{PS}(\omega) = \int S(\omega - \xi) G_{LDSP}(\xi) d\xi . \qquad (2.122)$$

Assuming that the $G_{BGP}(\omega)$ and $G_{LDSP}(\omega)$ are Lorentzian spectral profiles and substituting Eq. (2.122) into Eq. (2.121), the Brillouin gain is given by [8]:

$$G(\omega_S) = G_{CW}(\Delta\omega_P = 0) \frac{\Delta\omega_B/2}{\Delta\omega_B/2 + \Delta\omega_P/2} \int_{-\infty}^{+\infty} \frac{S(\omega)}{1 + \left(\frac{\omega - \omega_S - \omega_A}{\Delta\omega_B/2 + \Delta\omega_P/2} \right)^2} d\omega , \qquad (2.123)$$

where $\Delta\omega_P$ is the LD (pump) linewidth (FWHM) and $G_{CW}(\Delta\omega_P = 0)$ is the Brillouin gain for unmodulated LD (CW) with negligible linewidth which is given by [9]:

$$G_{CW}(\Delta\omega_P = 0) = \frac{g_B L_{eff} p_0}{A_{eff}} . \qquad (2.124)$$

The SBS threshold for a CW pump is given by [7-11]:

$$P_{th}^{CW} = 21 \frac{K A_{eff}}{g_B L_{eff}} , \qquad (2.125)$$

where K is the polarisation factor $(1 \le K \le 2)$ [12], K=1 for the polarisation of the pump wave and the Stokes wave maintaining throughout fibre, and K=2 for the complete polarisation scrambling as in SSMF. As an example, the CW SBS threshold for SSMF with $A_{eff} = 80 \mu m^2$ and $\alpha = 0.2 dB / km$ is 3.3 mW (+5.3 dBm).

It is reasonable for SBS to occur when $G_{\max} = G_{CW}(\Delta\omega_P = 0)$, where $G_{\max}$ is the maximum SBS gain for the modulated LD (pump) signal [13]. Thus the SBS threshold for the modulated LD (pump) signal is expressed by [8]:

$$P_{th} = \frac{21Kp_0}{G_{\max}}. \tag{2.126}$$

By using the Brillouin gain for CW pump with negligible linewidth, the SBS threshold is given by:

$$P_{th} = P_{th}^{CW} \frac{G_{CW}(\Delta\omega_P = 0)}{G_{\max}}. \tag{2.127}$$

This is the equation to estimate the SBS threshold for the modulated LD (pump) signal by calculating the maximum SBS gain for modulated pump in Eq. (2.123) and the SBS gain for CW pump in Eq. (2.124).

To suppress the SBS, several approaches have been presented and demonstrated [14-20]. A brief summarization is given below.

If the backward travelling Stokes waves are blocked and the build-up of the Stokes wave is prevented, arbitrary high SBS threshold can be, in theory, obtained. A method was proposed by inserting isolators in the fibre span [16]. However, it leads to increased complexity, cost, and loss, and a potential decrease in reliability.

It shows from Eqs. (2.123) and (2.127) that the SBS threshold can be increased by changing fibre parameters to reduce the maximum SBS gain. In this way the Brillouin bandwidth or acoustic frequency along fibre is changed. By using non-uniform fluorine doping of single-mode fibre, a 6 dB increase in SBS threshold was obtained [14]. By making the core radius nonuniform along the fibre, a 3.5 dB reduce of the effective Brillouin gain was achieved [15]. By concatenation of different types of fibres, a 1.8 dB increase in SBS threshold was realised [16]. By using a fibre with periodically induced residual-strain, a 3 dB increase in SBS threshold was obtained [17]. However, the methods by changing the fibre parameters are considered less feasible in a commercial system because of the careful fibre manufacturing, increasing cost and potentially decreasing reliability.

It shows from Eqs. (2.123) and (2.127) that the SBS threshold can be increased by reducing the maximum SBS gain for the modulated LD (pump) signal. Using phase-modulation superposed intensity-modulation technique [18, 21] the SBS threshold can be increased greatly by changing the input signal PSD in Eq. (2.123). By using a phase modulator following the amplitude modulator and applying one or more radio-frequency (RF) signals, a phase-modulation of the amplitude-modulated optical signal is generated. In theory the SBS threshold can be increased almost infinitely in principle and a +23.2 dBm of SBS threshold has been demonstrated [21]. However, the technique makes the transmitter more complex and expensive due to the requirements of an additional modulator and electronics to generate the RF signal.

Using alternative modulation schemes such as FSK, CPFSK and PSK, the input signal PSD is changed and the SBS threshold can be increased [8, 9, 11, 19, 20] further compared with

ASK. For a CW, ASK, FSK, and PSK signal the SBS thresholds are about +6, +9, +12, and +10 dBm respectively [11, 20]. For CPFSK signal the highest power up to +21 dBm is possible [22].

The technique of low frequency bias current amplitude modulation (dither) is the simplest and most easily realisable way to increase the SBS threshold and is the most feasible way for commercial systems. A large number of experiments have been reported by using this technique [23-27]. The SBS threshold up to +24 dBm is obtained [27].

2.7 Summary

In this chapter, the pulse propagation in optical fibres is investigated. The NLS equation is presented, several numerical approaches to the NLSE are introduced, among which the split-step Fourier method is the most widely used approach.

The theoretic model of GVD is presented. Optical fibre nonlinear effects including SPM, XPM, FWM and SBS are investigated. Analytical models for these effects are presented, which will be the foundation of the following chapters, and provide theoretical guidance for WDM system design.

Chapter 3

Numerical Simulation of WDM Transmission Systems

The design of photonic systems has reached a stage where simulation is no longer a luxury, but a necessity. This situation has arisen over only a few years, because systems performance has reached a number of limits. Until the last decade, optical communications systems were chiefly limited by loss, dispersion, and transmitter & receiver performance. However, loss is easy to calculate on the back of an envelope, and dispersion can be estimated by rule of thumb, aided by experience. It is the advent of optical amplifiers, enabling high powers and long un-regenerated distances that have caused significant fibre nonlinearity that necessitated the use of numerical modeling: to calculate the spectral broadening caused by SPM, amplitude modulation due to XPM, crosstalk due to FWM, and the interplay of nonlinearity and dispersion.

To achieve optimized transmission on optical links, equipment-makers and system integrators are assessing trade-offs between design variables including power range,

fibre nonlinearities, temperature stability, gain-shaping and dispersion management. At the same time, component manufacturers are expected to deliver significant annual price decreases even as the development of multi-port, wavelength specified components (such as add-drop multiplexers, transmitters, and wavelength routers) becomes increasingly complex, quality standards increase and tolerances grow tighter.

Many of these problems can be addressed with the help of automated software design tools. Just as Electronic Design Automation (EDA) tools have become an essential part of semiconductor and electronics industry development, Photonic Design Automation (PDA) tools can advance telecommunications infrastructure development.

In this chapter, we first introduce the typical WDM system and discuss the technology directions along which WDM systems can evolve to meet bandwidth capacity demands. Then the expressions of signal and noise for the Optical Pre-amplifiers (OPRs) at the decision point are derived. A method to evaluate average Q-factor from the eye diagrams and amplitude histograms, and thus evaluate BER through the Q-factor, is also introduced. Finally the implementation of simulations is presented.

3.1 Typical WDM system

Wavelength Division Multiplexing (WDM) has provided the scalability to cope with the capacity demands of data-driven communications. A typical point-to-point WDM system comprises:

- A number of transmitters, which can be either:
  - a directly-modulated laser
  - a laser operated CW with an external modulator

Each transmitter produces an *Optical Channel* which is a single optical carrier.

- A multiplexer, which can be:
  - wavelength selective, giving low excess loss
  - flat-passband giving a loss proportional to the number of inputs

The multiplexer combines Optical Channels into an *Optical Multiplexer Section* (*OMS*). The OMS ends at the demultiplexer that regains the individual optical channels. That is it includes the optical amplifier sections between the two multiplexers.

- Optical fibre plant, comprising
  - transmission fibre
  - (optional) dispersion compensating devices (e.g. fibre or grating)
  - in-line optical amplifier

- (optional) Optical Add-Drop multiplexer (OADM)
- Optical demultiplexer
- Optical receivers for each channel.

Figure 3.1 shows a schematic showing the layout of components in a typical WDM transmission system.

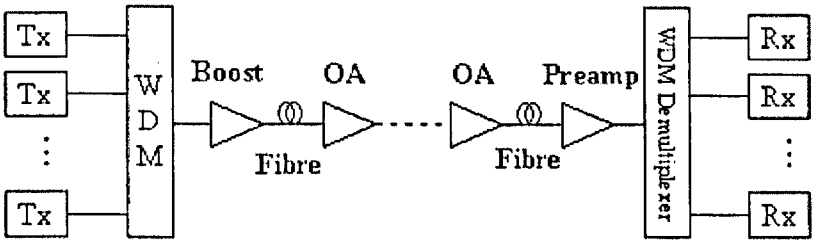

Figure 3.1: Typical structure of WDM transmission system

Ideally WDM channels do not interact (there is no optical crosstalk), and as many channels can be added and required, each operating at a high data rate. In practice, interaction occurs, and the number of channels is limited by the performance of the components [1].

We can identify three orthogonal requirements for providing a higher bit rate WDM link:

- higher total optical bandwidths (using more of the fibre's low-loss regions to get 80nm of optical bandwidth or more) [2, 3];
- higher bit rates per channel (say from 2.5 Gbit/s to 40 Gbit/s) [4, 5]; and
- higher density of individual channels (thus, reduced channel spacing, say from 100 to 20 GHz) [6, 7].

These requirements can be arranged as the axes [B, C, D] of a cube (Figure 3.2). The total capacity of the system is the cube's volume B·C·D.

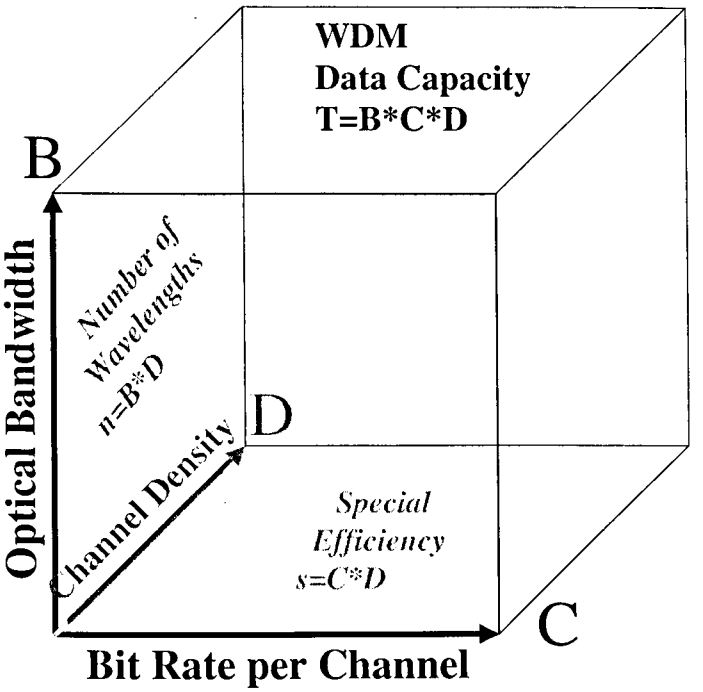

Figure 3.2: WDM capacity cube

3.2 Expressions of signal and noise

Now we start the derivations of the expressions of signal and noise at the decision point for the Optical Pre-amplifiers (OPRs). The configuration of the OPRs is shown in Fig. 3.3.

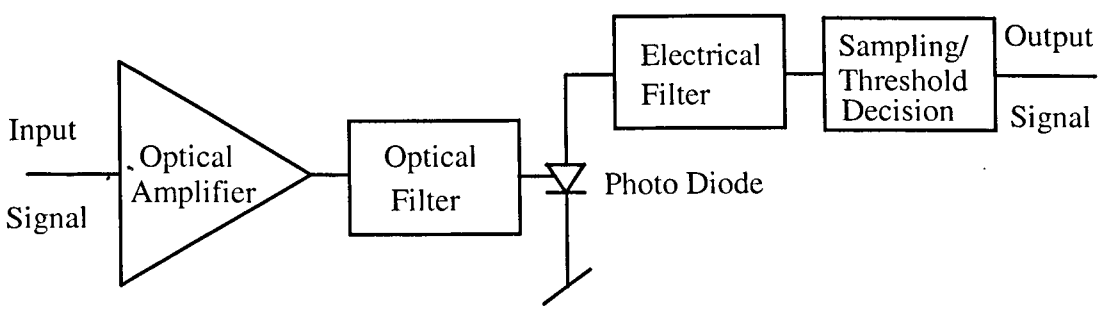

Figure 3.3: Configuration of the OPRs

The received signal for this model can be amplitude and/or frequency modulated, with arbitrary pulse shape (including frequency chirp). It can be deteriorated by optical fibre transmission including fibre dispersion and SPM. When the received signal is a FM signal, a FM/AM converter is inserted between optical preamplifier and PIN diode. Its frequency response can be combined with the transfer function of optical bandpass filter.

The optical amplifier is modelled by assuming that the input signal power is instantaneously amplified by a constant optical gain and that the noise due to spontaneous emission is assumed to be an additive, wide-sense stationary Gaussian noise process [8].

The generation of photo current is assumed to be an instantaneous process due to a simple ideal square law detection performed by the PIN diode. The analysis of the shot noise in the receiver is according to the theory in [9]. The PIN detector is assumed to be ideal with a unity intrinsic frequency transfer function because the frequency responses of the detector and the electrical amplifiers in the baseband receiver can be combined with the transfer function of the electrical filter.

For simplicity, all noise contributions to the baseband receiver are assumed to be mutually statistically independent noise processes. This is the ordinary treatment in the most of receiver models in the literature. Actually, there is some degree of correlation for the noise samples when non-ideal lowpass filtering is considered. In [10], it is possible to include this noise correlation to account for ISI effects and some

degradation in sensitivity due to the correlation effects have been reported for CPFSK systems. But the theory for the noise correlation is very complicated, especially for numerical calculation. In order to simplify the receiver model, the noise correlation effects are not considered in our accurate model.

The following results are derived from the bandpass signal theory which means that any reference frequency must be sufficiently high so that the spectral bandwidth of any arbitrary function in concern relative to the reference frequency is less than 200% [11]. This restriction, however, has no practical impact in optical communication systems due to the extremely high optical carrier frequency.

The electrical field of the received signal is resolved in two orthogonal polarisation states as shown in Fig. 3.4. We can define:

$$\vec{e}_s(t) = \sum_{k=1}^{2} e_{s,k}(t) \cdot \vec{e}_k, \qquad k = 1,2 \tag{3.1}$$

$$e_{s,k}(t) = \mathrm{Re}\left\{\tilde{e}_{s,k}(t) e^{j2\pi f_k t}\right\} \tag{3.2}$$

$$\tilde{e}_{s,k}(t) = \sqrt{\alpha_k}\, \tilde{s}_k(t) e^{j2\pi f_{s,k} t} \tag{3.3}$$

$$\tilde{s}_k(t) = \sigma_k(t) e^{j\theta_k(t)} \tag{3.4}$$

$$f_{s,k} = f_s - f_k \tag{3.5}$$

where $\vec{e}_s(t)$ is the instantaneous electrical field vector of the input signal to the optical preamplifier. $\vec{e}_k$ (k=1,2) are the mutually orthogonal unit vectors. $e_{s,k}(t)$ are the polarisation components of $\vec{e}_s(t)$ as shown in Fig. 3.4. $\tilde{e}_{s,k}(t)$ is the complex

envelope of $e_{s,k}(t)$. f_k is a reference frequency associated with the polarisation states of optical bandpass filters. f_s is the signal carrier frequency. $f_{s,k}$ is the detuning of the optical filter. α_k ($\alpha_1 + \alpha_2 = 1$) denotes the coupling coefficient of signal power into each of the two orthogonal polarisation components. $\tilde{s}_k(t)$ is the total modulation of the input signal and $\sigma_k(t)$ and $\theta_k(t)$ are respectively the amplitude modulation and the phase modulation of the input signal. The detuning of the optical filter is shown in Fig. 3.5 schematically. The reference frequency f_k is selected as the central frequency of optical bandpass filter. For a CPFSK signal, it is optically demodulated by a Mach-Zehnder FM/AM converter. The demodulation curve is periodical (as shown in Fig. 3.5) with a period of the reciprocal of the delay t_d of the FM/AM converter. The offset of the central frequency between optical demodulation and optical filter is represented by the reference phase v_{kd}. For an ASK signal, the optical demodulation is not required, so the reference frequency f_k is the signal carrier frequency and then $f_{s,k} = 0$.

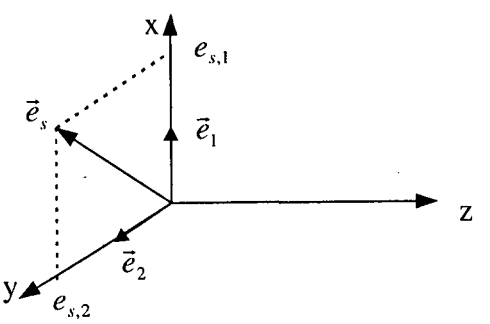

Figure 3.4: The schematic of the electrical field vectors of the input signal

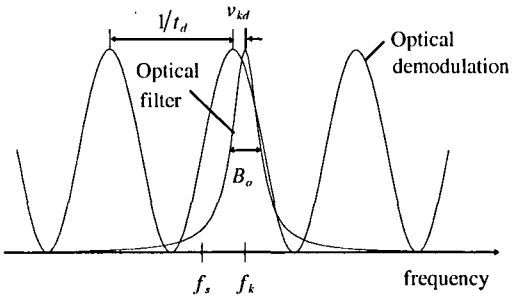

Figure 3.5: The schematic of the detuning of optical bandpass filter

In the frequency domain, Eqs. (3.1) - (3.3) become:

$$\vec{E}_s(f) = \sum_{k=1}^{2} E_{s,k}(f) \cdot \vec{e}_k \tag{3.6}$$

$$E_{s,k}(f) = \frac{1}{2}\left[\tilde{E}_{s,k}(f - f_k) + \tilde{E}^*_{s,k}(-f - f_k)\right] \tag{3.7}$$

$$\tilde{E}_{s,k}(f) = \sqrt{\alpha_k}\,\tilde{S}_k(f - f_{s,k}) \tag{3.8}$$

Now, consider the spontaneous emission generated by the optical preamplifier. The two polarisation states of the spontaneous emission are assumed to be identical, mutually statistical independent, additive, and wide-sense stationary Gaussian noise process [12]. Since the optical amplifier has a finite bandwidth and the optical bandpass filter is used in the OPRs, the spontaneous emission is band-limited. Thus the spectral noise density of the spontaneous emission for each polarisation state, as shown in Fig. 3.6 schematically, can be written as:

$$S_{sp}(f) = N_{sp}(f - f_{sp}) + N_{sp}(-f - f_{sp}) \tag{3.9}$$

where f_{sp} is the centre frequency of the positive frequency contents of the spontaneous emission. $N_{sp}(f)$ is the lowpass spectral noise density of the spontaneous emission.

The instantaneous electrical field of the spontaneous emission can be defined as:

$$\vec{e}_{sp}(t) = \sum_{k=1}^{2} e_{sp,k}(t) \cdot \vec{e}_k \tag{3.10}$$

$$e_{sp,k}(t) = \mathrm{Re}\left\{\tilde{e}_{sp,k}(t) e^{j2\pi f_k t}\right\} \tag{3.11}$$

$$\tilde{e}_{sp,k}(t) = e_{i,k}(t) + j e_{q,k}(t) \tag{3.12}$$

where $\vec{e}_{sp}(t)$ is the instantaneous electrical field vector of the spontaneous emission, $e_{sp,k}(t)$ and $\tilde{e}_{sp,k}(t)$ are the polarisation components and corresponding complex envelope of the spontaneous emission electrical field, respectively. $e_{i,k}(t)$ and $e_{q,k}(t)$ are, respectively, the inphase and quadrature modulation components of the spontaneous emission electrical field with respect to the reference frequency f_k.

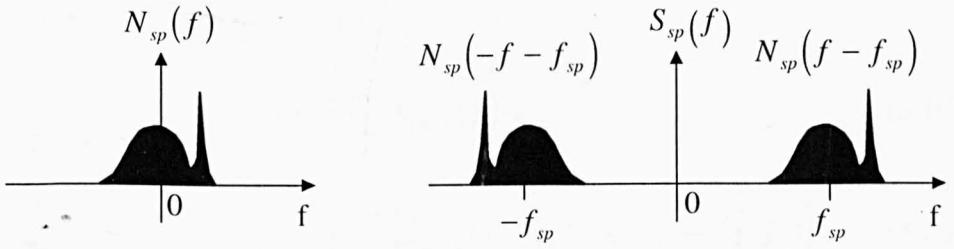

Figure 3.6: Illustration of $N_{sp}(f)$ and $S_{sp}(f)$ for an optical amplifier.

According to the signal theory in [13, 14], an arbitrary random process can be represented by its Fourier transform. The properties of the Fourier transform of a random process can be found in [13, 14]. Thus, from Eqs. (3.10) - (3.12) the spontaneous emission of the optical amplifier can be expressed in the frequency domain as the following forms:

$$\vec{E}_{sp}(f) = \sum_{k=1}^{2} E_{sp,k}(f) \cdot \vec{e}_k \tag{3.13}$$

$$E_{sp,k}(f) = \frac{1}{2}\left[\tilde{E}_{sp,k}(f - f_k) + \tilde{E}^{*}_{sp,k}(-f - f_k)\right] \tag{3.14}$$

$$\tilde{E}_{sp,k}(f) = E_{i,k}(f) + jE_{q,k}(f) \tag{3.15}$$

The output signal of the optical preamplifier can be written as:

$$\vec{E}_{OA}(f) = \sum_{k=1}^{2} E_{OA,k}(f) \cdot \vec{e}_k \tag{3.16}$$

$$E_{OA,k}(f) = \frac{1}{2}\left[\tilde{E}_{OA,k}(f - f_k) + \tilde{E}^{*}_{OA,k}(-f - f_k)\right] \tag{3.17}$$

$$\tilde{E}_{OA,k}(f) = \sqrt{G}\tilde{E}_{s,k}(f) + \tilde{E}_{sp,k}(f) \tag{3.18}$$

where G is the power gain of the optical preamplifier. The output signal of the optical bandpass filter is given by:

$$\vec{E}_{OF}(f) = \sum_{k=1}^{2} E_{OF,k}(f) \cdot \vec{e}_k \tag{3.19}$$

$$E_{OF,k}(f) = \frac{1}{2}\left[\tilde{E}_{OF,k}(f - f_k) + \tilde{E}^{*}_{OF,k}(-f - f_k)\right] \tag{3.20}$$

$$\tilde{E}_{OF,k}(f) = \tilde{H}_k(f)\left[\sqrt{G}\tilde{E}_{s,k}(f) + \tilde{E}_{sp,k}(f)\right] \tag{3.21}$$

where $\tilde{H}_k(f)$ is the complex envelope of the transfer function of the optical filter for each polarisation state.

For convenience the factor of one-half is omitted in Eq. (3.21). This is due to a common practice of referring to a unity power transfer function of the envelope of lossless optical filters. The applied convention implies that an optical bandpass filter with a frequency transfer function $H_k(f)$ is represented by the complex envelope $\tilde{H}_k(f)$, with respect to the reference frequency f_k, defined as:

$$\tilde{H}_k(f) = \begin{cases} H_k(f+f_k), & |f| < f_k \\ 0, & |f| > f_k \end{cases} \tag{3.22}$$

Since the two polarisation states of the total electrical field incident on the PIN diode are orthogonal, the equivalent (i.e. noise free) photo current generated by the detection can be represented by:

$$i^{(PD)}(t) = \sum_{k=1}^{2} i_k^{(PD)}(t) \tag{3.23}$$

$$i_k^{(PD)}(t) = \frac{1}{2}\frac{\eta e}{h\nu}\left|\tilde{e}_{OF,k}(t)\right|^2 \tag{3.24}$$

where η is the quantum efficiency of PIN diode, h is the Planck's constant, ν is the optical signal frequency and e is the electron unity charge. In the frequency domain, Eqs. (3.23) and (3.24) become:

$$I^{(PD)}(f) = \sum_{k=1}^{2} I_k^{(PD)}(f) \tag{3.25}$$

$$I_k^{(PD)}(f) = \frac{1}{2}\frac{\eta e}{h\nu}\tilde{E}_{OF,k}(f) \otimes \tilde{E}^*_{OF,k}(-f) \tag{3.26}$$

where $I_k^{(PD)}(f)$ is the Fourier transform of the equivalent photo current $i_k^{(PD)}(t)$ generated by the detection of each polarisation component. Substituting Eq. (3.21) into Eq. (3.26), we have:

$$\begin{aligned} I_k^{(PD)}(f) = & \frac{1}{2}\frac{\eta e}{h\nu} G\left[\tilde{H}_k(f)\tilde{E}_{s,k}(f)\right] \otimes \left[\tilde{H}_k^*(-f)\tilde{E}_{s,k}^*(-f)\right] \\ & + \frac{1}{2}\frac{\eta e}{h\nu}\sqrt{G}\left\{\left[\tilde{H}_k(f)\tilde{E}_{s,k}(f)\right] \otimes \left[\tilde{H}_k^*(-f)\tilde{E}_{sp,k}^*(-f)\right]\right. \\ & \left. + \left[\tilde{H}_k^*(-f)\tilde{E}_{s,k}^*(-f)\right] \otimes \left[\tilde{H}_k(f)\tilde{E}_{sp,k}(f)\right]\right\} \\ & + \frac{1}{2}\frac{\eta e}{h\nu}\left[\tilde{H}_k(f)\tilde{E}_{sp,k}(f)\right] \otimes \left[\tilde{H}_k^*(-f)\tilde{E}_{sp,k}^*(-f)\right] \end{aligned} \tag{3.27}$$

From Eq. (3.27) we can define the detected signal and noise as follows:

The Fourier transform of the equivalent instantaneous optical signal power at the input of the PIN diode is:

$$P_s(f) = \sum_{k=1}^{2} P_{s,k}(f) \tag{3.28}$$

$$P_{s,k}(f) = \frac{1}{2} G\left[\tilde{H}_k(f)\tilde{E}_{s,k}(f)\right] \otimes \left[\tilde{H}_k^*(-f)\tilde{E}_{s,k}^*(-f)\right] \tag{3.29}$$

The Fourier transform of the equivalent instantaneous signal photo-current at the output of the PIN diode is:

$$I_s^{(PD)}(f) = \sum_{k=1}^{2} I_{s,k}^{(PD)}(f) \tag{3.30}$$

$$\begin{aligned} I_{s,k}^{(PD)}(f) &= \frac{1}{2}\frac{\eta e}{h\nu} G\left[\tilde{H}_k(f)\tilde{E}_{s,k}(f)\right] \otimes \left[\tilde{H}_k^*(-f)\tilde{E}_{s,k}^*(-f)\right] \\ &= \frac{\eta e}{h\nu} P_{s,k}(f) \end{aligned} \tag{3.31}$$

The Fourier transform of the equivalent instantaneous signal-spontaneous emission beat noise current at the output of PIN diode is:

$$I_{s-sp}^{(PD)}(f)=\sum_{k=1}^{2} I_{s-sp,k}^{(PD)}(f) \tag{3.32}$$

$$I_{s-sp,k}^{(PD)}(f)=\frac{1}{2}\frac{\eta e}{h\nu}\sqrt{G}\left\{\left[\tilde{H}_k(f)\tilde{E}_{s,k}(f)\right]\otimes\left[\tilde{H}_k^*(-f)\tilde{E}_{sp,k}^*(-f)\right]+\left[\tilde{H}_k^*(-f)\tilde{E}_{s,k}^*(-f)\right]\otimes\left[\tilde{H}_k(f)\tilde{E}_{sp,k}(f)\right]\right\} \tag{3.33}$$

The Fourier transform of the average optical spontaneous emission power incident on the PIN diode is:

$$\overline{P_{sp}}(f)=\sum_{k=1}^{2}\overline{P_{sp,k}}(f) \tag{3.34}$$

$$P_{sp,k}(f)=\frac{1}{2}\left[\tilde{H}_k(f)\tilde{E}_{sp,k}(f)\right]\otimes\left[\tilde{H}_k^*(-f)\tilde{E}_{sp,k}^*(-f)\right] \tag{3.35}$$

and the Fourier transform of the corresponding equivalent DC current is:

$$\overline{I_{sp}^{(PD)}}(f)=\sum_{k=1}^{2}\overline{I_{sp,k}^{(PD)}}(f) \tag{3.36}$$

$$\overline{I_{sp,k}^{(PD)}}(f)=\frac{\eta e}{h\nu}\overline{P_{sp,k}}(f) \tag{3.37}$$

The Fourier transform of the equivalent spontaneous-spontaneous emission beat current at the output of PIN diode is:

$$I_{sp-sp}^{(PD)}(f)=\sum_{k=1}^{2} I_{sp-sp,k}^{(PD)}(f) \tag{3.38}$$

$$I_{sp-sp,k}^{(PD)}(f)=\frac{1}{2}\frac{\eta e}{h\nu}\left[\tilde{H}_k(f)\tilde{E}_{sp,k}(f)\right]\otimes\left[\tilde{H}_k^*(-f)\tilde{E}_{sp,k}^*(-f)\right]-\overline{I_{sp,k}^{(PD)}}(f) \quad (3.39)$$

In Eq. (3.27) the last term includes the spontaneous shot noise and the spontaneous-spontaneous beat noise. We have defined the spontaneous shot noise in Eq. (3.37), so we have the form of the spontaneous-spontaneous beat noise as Eq. (3.39).

For simplicity, all noise contributions are assumed to be mutually statistically independent noise processes (i.e. the variance of the total noise current is the sum of the variances for each noise current contributing to the total noise). Since the time impulse response of the electrical filter is real, its transfer function has the following property:

$$H_e^*(-f)=H_e(f) \quad (3.40)$$

The signal and noise at the output of the baseband receiver (i.e. the decision point) can be written as follows:

The equivalent signal current is:

$$i_s(t)=\sum_{k=1}^{2} i_{s,k}(t) \quad (3.41)$$

$$i_{s,k}(t)=\frac{\eta e}{h\nu}h_e(t)\otimes p_{s,k}(t) \quad (3.42)$$

where $h_e(t)$ is the time impulse response of the electrical filter. By using Eq. (3.31) and Fourier transforms, Eq. (3.42) becomes:

$$i_{s,k}(t) = \frac{\eta e}{h\nu} F_f^{-1}\{H_e(f)P_{s,k}(f)\} \tag{3.43}$$

The mean square current of the shot noise due to the signal current is:

$$\overline{i_s^2}(t) = \sum_{k=1}^{2} \overline{i_{s,k}^2}(t) \tag{3.44}$$

$$\overline{i_{s,k}^2}(t) = e\frac{\eta e}{h\nu} h_e^2(t) \otimes p_{s,k}(t) \tag{3.45}$$

By using Fourier transforms, Eq. (3.45) becomes:

$$\overline{i_{s,k}^2}(t) = e\frac{\eta e}{h\nu} F_f^{-1}\{[H_e(f) \otimes H_e(f)]P_{s,k}(f)\} \tag{3.46}$$

The mean square current of the signal-spontaneous emission beat noise is:

$$\overline{i_{s-sp}^2}(t) = \sum_{k=1}^{2} \overline{i_{s-sp,k}^2}(t) \tag{3.47}$$

$$\overline{i_{s-sp,k}^2}(t) = \left\langle \left[h_e(t) \otimes i_{s-sp,k}^{(PD)}(t)\right]^2 \right\rangle \tag{3.48}$$

By using Fourier transforms, Eq. (3.48) becomes:

$$\overline{i_{s-sp,k}^2}(t) = F_f^{-1}\left\{\left\langle \left[H_e(f)I_{s-sp,k}^{(PD)}(f)\right] \otimes \left[H_e(f)I_{s-sp,k}^{(PD)}(f)\right] \right\rangle\right\} \tag{3.49}$$

The mean square current of the shot noise due to the average spontaneous emission power incident on the PIN diode is:

$$\overline{i_{sp}^2} = \sum_{k=1}^{2} \overline{i_{sp,k}^2} \tag{3.50}$$

$$\overline{i_{sp,k}^2} = \left\langle e\frac{\eta e}{h\nu} h_e^2(t) \otimes p_{sp,k} \right\rangle \tag{3.51}$$

By using Fourier transforms, Eq. (3.51) becomes:

$$\overline{i_{sp,k}^2} = e\frac{\eta e}{h\nu} F_f^{-1}\left\{ [H_e(f) \otimes H_e(f)] \overline{P_{sp,k}}(f) \right\} \tag{3.52}$$

The mean square current of the spontaneous-spontaneous emission beat noise is:

$$\overline{i_{sp-sp}^2} = \sum_{k=1}^{2} \overline{i_{sp-sp,k}^2} \tag{3.53}$$

$$\overline{i_{sp-sp,k}^2} = \left\langle \left[h_e(t) \otimes i_{sp-sp,k}^{(PD)} \right]^2 \right\rangle \tag{3.54}$$

By using Fourier transforms, Eq. (3.54) becomes:

$$\overline{i_{sp-sp,k}^2} = F_f^{-1}\left\{ \left\langle \left[H_e(f) I_{sp-sp,k}^{(PD)}(f) \right] \otimes \left[H_e(f) I_{sp-sp,k}^{(PD)}(f) \right] \right\rangle \right\} \tag{3.55}$$

After long and complicated derivations, we can get the expressions of signal and noise at the output of the baseband receiver as follows:

The equivalent optical signal power at the input of the PIN diode is given by:

$$p_s(t) = \sum_{k=1}^{2} p_{s,k}(t) \tag{3.56}$$

$$p_{s,k}(t) = \frac{1}{2}\alpha_k G F_f^{-1}\left\{\left[\tilde{H}_k(f)\tilde{S}_k(f - f_{s,k})\right] \otimes \left[\tilde{H}_k^*(-f)\tilde{S}_k^*(-f - f_{s,k})\right]\right\} \tag{3.57}$$

The equivalent signal current is given by:

$$i_s(t) = \sum_{k=1}^{2} i_{s,k}(t) \tag{3.58}$$

$$i_{s,k}(t) = \frac{1}{2}\frac{\eta e}{h\nu}\alpha_k G F_f^{-1}\left\{H_e(f)\left[\left[\tilde{H}_k(f)\tilde{S}_k(f - f_{s,k})\right] \otimes \left[\tilde{H}_k^*(-f)\tilde{S}_k^*(-f - f_{s,k})\right]\right]\right\} \tag{3.59}$$

The mean square current of the shot noise due to the signal current is given by:

$$\overline{i_s^2}(t) = \sum_{k=1}^{2} \overline{i_{s,k}^2}(t) \tag{3.60}$$

$$\begin{aligned}\overline{i_{s,k}^2}(t) = \frac{1}{2} e \frac{\eta e}{h\nu}\alpha_k G F_f^{-1}\Big\{&\left[H_e(f) \otimes H_e(f)\right] \\ &\cdot \left[\left[\tilde{H}_k(f)\tilde{S}_k(f - f_{s,k})\right] \otimes \left[\tilde{H}_k^*(-f)\tilde{S}_k^*(-f - f_{s,k})\right]\right]\Big\}\end{aligned} \tag{3.61}$$

The mean square current of the signal-spontaneous emission beat noise is given by:

$$\overline{i_{s-sp}^2}(t) = \sum_{k=1}^{2} \overline{i_{s-sp,k}^2}(t) \tag{3.62}$$

$$\overline{i_{s-sp,k}^2}(t) = 2\alpha_k \left(\frac{\eta e}{h\nu}\right)^2 GF_f^{-1} \left\{ \int_{-\infty}^{+\infty} dy \left[\left[H_e(f+y) H_e^*(y) \right] \otimes \left[\left| \tilde{H}_k(y) \right|^2 N_{sp}(f_{k,sp}+y) \right] \right] \right.$$
$$\left. \cdot \tilde{H}_k(f+y) \tilde{H}_k^*(y) \tilde{S}_k(f+y-f_{s,k}) \tilde{S}_k^*(y-f_{s,k}) \right\} \tag{3.63}$$

The mean square current of the shot noise due to the average spontaneous emission power incident on the PIN diode is given by:

$$\overline{i_{sp}^2} = \sum_{k=1}^{2} \overline{i_{sp,k}^2} \tag{3.64}$$

$$\overline{i_{sp,k}^2} = 2e \frac{\eta e}{h\nu} \int_{-\infty}^{+\infty} dx \left| \tilde{H}_k(x) \right|^2 N_{sp}(f_{k,sp}+x) \int_{-\infty}^{+\infty} dy \left| H_e(y) \right|^2 \tag{3.65}$$

The mean square current of the spontaneous-spontaneous emission beat noise is given by:

$$\overline{i_{sp-sp}^2} = \sum_{k=1}^{2} \overline{i_{sp-sp,k}^2} \tag{3.66}$$

$$\overline{i_{sp-sp,k}^2}$$
$$= 4 \left(\frac{\eta e}{h\nu}\right)^2 \int_{-\infty}^{+\infty} dy \left| H_e(y) \right|^2 \left\{ \left[\left| \tilde{H}_k(y) \right|^2 N_{sp}(f_{k,sp}+y) \right] \otimes \left[\left| \tilde{H}_k(-y) \right|^2 N_{sp}(f_{k,sp}-y) \right] \right\} \tag{3.67}$$

Eqs. (3.56) to (3.67) are the basic formulas to calculate the signal and the noise for the simulation.

3.3 System performance estimation

As far as WDM signal waveforms (and thus the eye diagrams) can be reconstructed in electrical domain, it is not always necessary to use optical method to obtain WDM transmission quality information. Several reports have evaluated amplitude histograms, Q-factors and bit error rate (BER) obtained by the electrical technique [15, 16, 17]. Reference [15] confirmed that the degradation of an optical signal due to noise, crosstalk and chromatic dispersion can be detected from amplitude histograms. However, it is difficult to evaluate signal-to-noise ratio (SNR) degradation quantitatively because the mark level peak in the histograms is not clear when the chromatic dispersion is large. Reference [16] defined a method to evaluate average Q-factor from the eye diagrams and amplitude histograms. This method has sensitivity to both the SNR degradation and pulse distortion of optical signals influenced by chromatic dispersion in transmission fibre. Reference [17] introduced a technique to evaluate BER through the Q-factor.

As described in Fig. 3.7, the average Q-factor (Q_{avg}) is expressed by [16]:

$$Q_{avg} = \frac{\left|\mu_{1,avg} - \mu_{0,avg}\right|}{\sigma_{1,avg} + \sigma_{0,avg}} \tag{3.68}$$

where $\mu_{i,avg}$ and $\sigma_{i,avg}$ are the mean and standard deviation of the mark ($i = 1$) and space ($i = 0$) levels of all sampled data, respectively. μ is set to the difference of the

mean of the mark and the space levels. Two thresholds are defined with coefficient α lies between 0 and 0.5:

$$D_{0,1} = \mu_{0,1} \pm \alpha\mu, \qquad 0 < \alpha < 0.5 \tag{3.69}$$

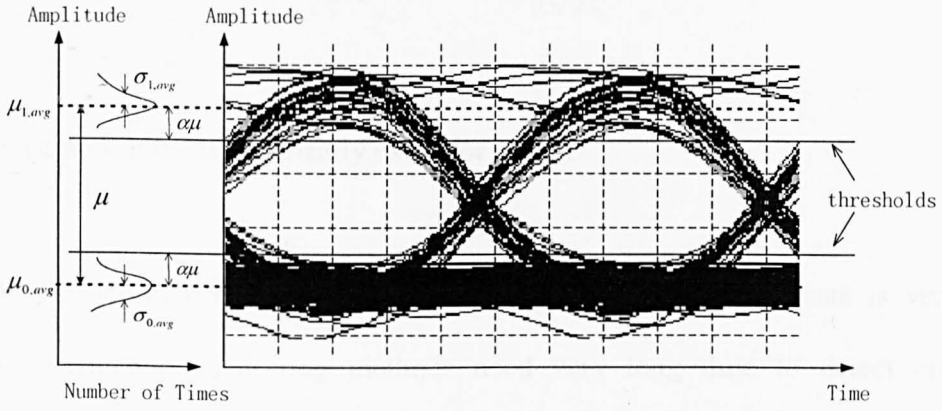

Figure 3.7: Definition of averaged Q-factor

Histograms with amplitudes larger than $\mu_1 - \alpha\mu$ are regarded as mark level distributions, while histograms with amplitudes smaller than $\mu_0 + \alpha\mu$ are regarded as space level distributions. This masking process removes the cross-point data and improves measurement accuracy [18].

While the exact probability density function for optical noise is not exactly Gaussian, a Gaussian approximation can lead to good BER estimates [17]:

$$BER(D) = \frac{1}{2}\left\{ erfc\left(\frac{|\mu_1 - D|}{\sigma_1}\right) + erfc\left(\frac{|\mu_0 - D|}{\sigma_0}\right)\right\} \tag{3.70}$$

where $\mu_{0,1}$ and $\sigma_{0,1}$ are the mean and standard deviation of the mark and space data rails, D is the decision level, and $erfc(x)$ is a form of the complementary error function given by:

$$erfc(x) = \frac{1}{\sqrt{2\pi}} \int_x^{\infty} e^{-\beta^2/2} d\beta \approx \frac{1}{x\sqrt{2\pi}} e^{-x^2/2} \tag{3.71}$$

where the approximation is nearly exact for $x > 3$.

In a high-performance optical transmission system, the bit error rate is very low, traditional quality monitoring methods need very long time to detect errors in transmission. Eqs. (3.68) and (3.70) provide fast and simple evaluations of WDM optical transmission quality with acceptable accuracy, as demonstrated in the following chapters.

3.4 Implementation of simulation

In this section the implementation of the simulation is presented. The generation of the pseudo random binary sequence (PRBS) with different sequence length is described. The procedure of the implementation of the system-level simulation is given. The method to calculating the signal-spontaneous emission beat noise, which is more complicated and time consuming than any other calculations, is described.

1. PRBS

A n-stage shift register PRBS generator, which produces a $2^n - 1$ PRBS, is shown in Fig. 3.8. The number of possible PRBS obtainable from an n-stage shift register is listed in table 3.1 [19]. As an exception, for an 8-stage shift register more than 1 tap registers have to be used to produce a PRBS. The sequence length of the PRBS produced by the 8-stage shift register is 255 and the number of the possible PRBS is 16. As an example, the tap register can be 4, 5 and 6.

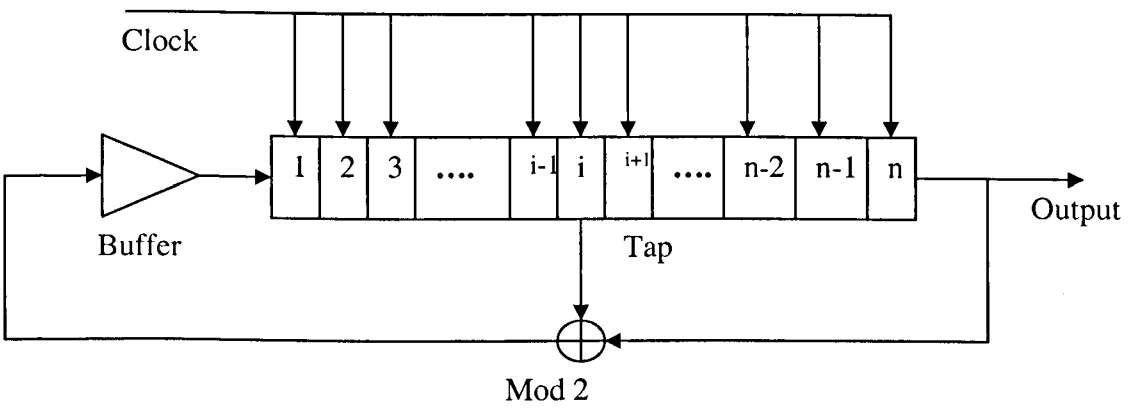

Figure 3.8: A n-stage shift register PRBS generator

The FFT is an efficient tool for the calculations of signal and noise. The FFT with the sample number of 2^n is much more efficient than that with any other sample numbers. To speed up the calculations, the sequence length of the PRBS is selected as 2^n instead of $2^n - 1$. Since the PRBS sequence has 2^{n-1} bits of one and $2^{n-1} - 1$ bits of zero, the extra bit, a zero, is inserted in the sequence. The largest number of the consecutive bits of one in the sequence is n whereas the largest number of the consecutive bits of zero is n-1. So the extra bit of zero is included after the last zero of the longest group of zeros.

Table 3.1: Number of PRBS obtainable from an n-stage shift register

Number of Stages	Sequence Length	Number of PRBS	Example Tap Register
3	7	2	2
4	15	2	3
5	31	6	3
6	63	6	5
7	127	18	6
9	511	48	5
10	1024	60	7
11	2047	176	9

In this thesis, a 128-bits PRBS is used for trading off of the implementation time and the accuracy of the simulations in the optical nonlinear transmission and the accurate model. The bit numbers per sample used is usually chosen as 32 bit/sample. But when the optical nonlinear transmissions are considered and the transmitter power is very high, the bit number per sample has to increase to ensure the calculation accuracy. For example, when the peak power is larger than 25 dBm, the bit number per sample should be increased to 64 and when it is larger than 30 dBm, the bit number per sample should be increased to 128.

2. Procedure for calculation of signal-spontaneous emission beat noise

It is easy to see from the expressions of signal and noise that the signal-spontaneous emission beat noise is the most complicated term and the most time consuming for the calculations of signal and noise. The implementation time of the whole system is highly dependent on the calculation speed of this term.

Since the noise is real at the decision point of the baseband receiver, its Fourier transform has a symmetry with its complex conjugate as the form: $F^*(f) = F(-f)$. By using this symmetry, only half of the spectrum needs to be calculated. Since the amplitude of the Fourier transform approaches zero with the increasing frequency, the integral in Eq. (3.63) only needs to be calculated to the frequency where the integral satisfies a given accuracy of the calculations. Therefore, the calculation of this term can be greatly speeded up compared to the calculation over the whole sampling frequency range.

The procedure of the calculation of the signal-spontaneous emission beat noise is shown in Fig. 3.9.

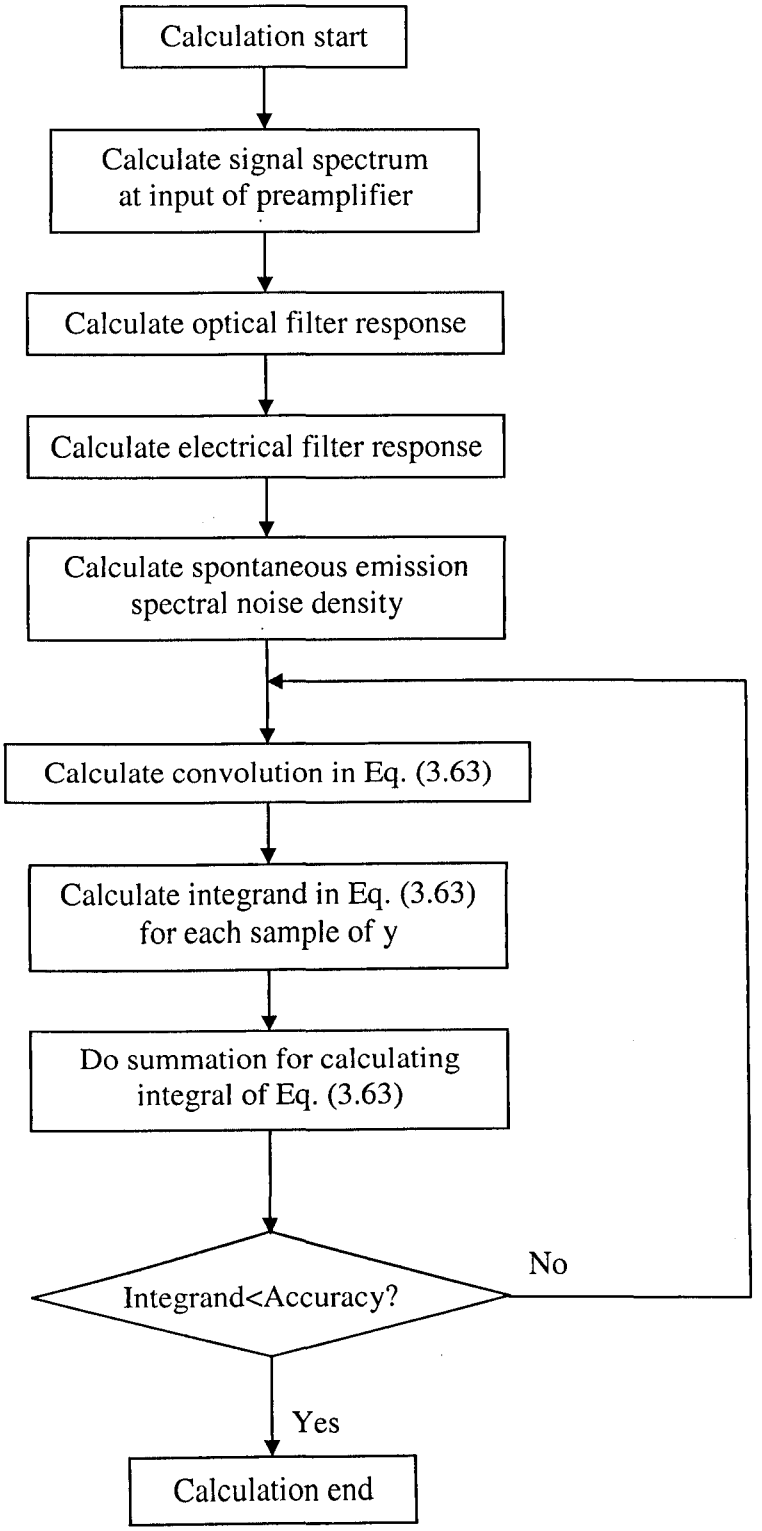

Figure 3.9: Procedure to calculate signal-spontaneous emission beat noise

3. Procedure of implementation of simulation

To calculate the BER and the receiver sensitivity of the OPRs, the signal and noise have to be calculated efficiently. When the input signal is a long sequence such as a long PRBS, the FFT is a very efficient tool for the calculations. By using Eqs. (3.56) to (3.67), the signal and noise can be calculated. Then by using Eqs. (3.68) and (3.70) the BER can be obtained. The procedure of the calculations is described in Fig. 3.10.

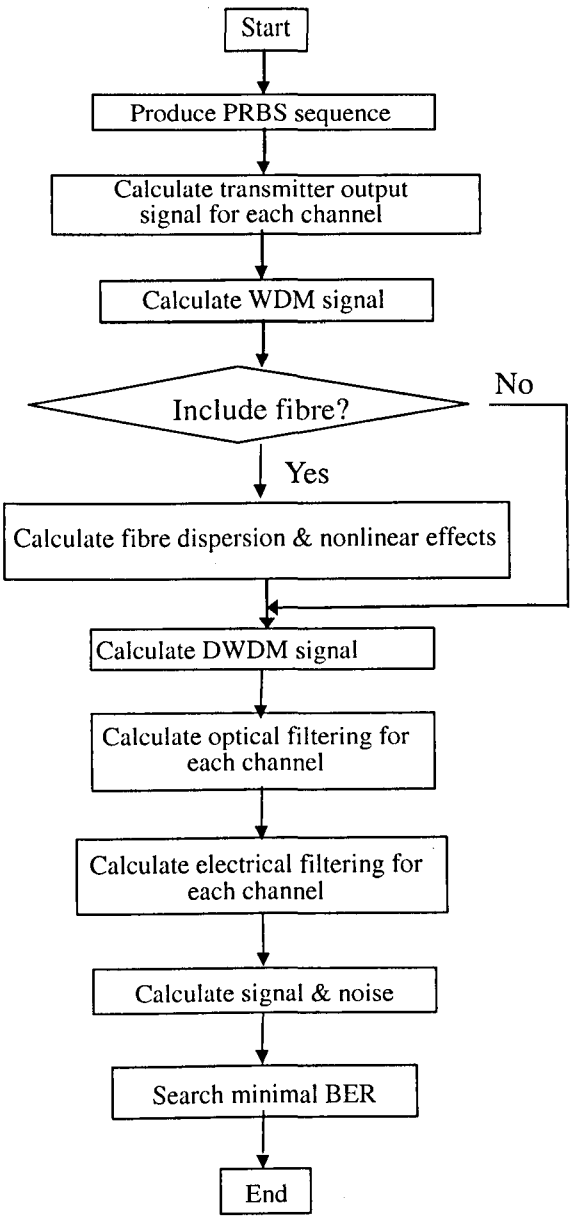

Figure 3.10: Procedure of the implementation of the simulation.

3.5 Summary

In this chapter, typical WDM system is introduced, three technology directions are identified for providing a higher bit rate WDM link: higher total optical bandwidths, higher bit rates per channel, and higher density of individual channels.

The expressions of signal and noise at the decision point for the Optical Pre-amplifiers (OPRs) are derived. It is easy to see from the expressions of signal and noise that the signal-spontaneous emission beat noise is the most complicated term and the most time consuming for the calculations of signal and noise. The implementation time of the whole system is highly dependent on the calculation speed of this term.

A method to evaluate average Q-factor from the eye diagrams and amplitude histograms, and thus evaluate BER through the Q-factor, is introduced. This method provides fast and simple evaluations of WDM optical transmission quality with acceptable accuracy.

The implementation of the numerical simulation is presented. The generation of the pseudo random binary sequence (PRBS) with different sequence length is described. The procedure of the implementation of the system-level simulation is given. The method to calculate the signal-spontaneous emission beat noise, which is more complicated and time consuming than any other calculations, is described.

Chapter 4

Receiver Analysis – 100 / 150 km WDM Transmission

From the previous chapter, the nonlinear effect denoted SPM is present in the optical fibre due to power dependence of the refractive index of fibre. SPM-induced frequency chirp has an opposite sign to that of the dispersion-induced frequency chirp and is proportional to the peak-power of optical pulses. Hence, some amount of dispersion compensation is expected. Using prechirp, the dispersion-induced chirp can also be compensated partially. It is shown in this chapter that the receiver sensitivity can be improved by using a favourable extinction ratio of the input signal. In this chapter, the influence of variations in fibre dispersion, fibre loss and effective core area on system performance is investigated. Then the effects of prechirp, extinction ratio and rise time of the input signal on system performance are studied. Finally, the influence of the sequence length used in simulations is discussed.

In this chapter, investigations are based on an 8×10Gb/s WDM System. The fibre parameters used in simulations are the fibre loss of 0.2 dB/km, fibre dispersion of 17 ps/km/nm, higher order dispersion of 0.06 $ps/km/nm^2$ and nonlinearity coefficient of 1.37 $W^{-1}km^{-1}$. The Optical Pre-amplified Receiver (OPR) parameters used in simulations are the optical gain of 40 dB, noise figure of 3 dB, reference sensitivity of the baseband receiver of -15.5 dBm, a Lorentzian shaped optical filter of 20 GHz bandwidth and a 5th order Bessel electrical filter of 7 GHz bandwidth. The transmitter parameters used in simulations are a chirp-free 128-bits PRBS with raised-cosine pulse (rise time of 20 ps) and extinction ratio of infinity (corresponding to the normalised bias voltage of -1, modulation depth of 1 and asymmetry factor of 0). These values are used throughout this chapter except that those parameters are investigated.

4.1 Influence of variation in fibre parameters

In this section, the influence on system performance in optical transmission of variation in fibre parameters is investigated. The eye closure penalty and the receiver sensitivity of the receivers are calculated with the varying transmitter power.

4.1.1 Variation of fibre loss

Fig. 4.1 shows the eye closure penalty (a) and receiver sensitivity of the OPRs (b) for 100 km transmission versus the average transmitter power for 3 different fibre loss (0.2, 0.25 and 0.3 dB/km). At very high transmitter power, the sensitivity has a rapid increase in penalty. The curves have similar shapes for different fibre losses but the optimum

transmitter power increases with an increasing fibre loss. The optimum sensitivities are nearly the same for different fibre losses. The sensitivity has a ripple when the transmitter power exceeded a certain level which increases with an increasing fibre loss. The allowable transmitter power range increases rapidly with an increasing fibre loss.

Fig. 4.2 shows the eye closure penalty (a) and receiver sensitivity of the OPRs (b) for 150 km transmission versus the average transmitter power for 3 different fibre loss (0.2, 0.25 and 0.3 dB/km). At very high transmitter power, the sensitivity has a rapid increase in penalty. The eye closes completely for low transmitter power and high transmitter power which is dependent on the fibre loss. The curves have similar shapes for different fibre losses but the optimum transmitter power increases with an increasing fibre loss. The optimum sensitivity increases in penalty with an increasing fibre loss. The allowable transmitter power range decreases rapidly with an increasing fibre loss.

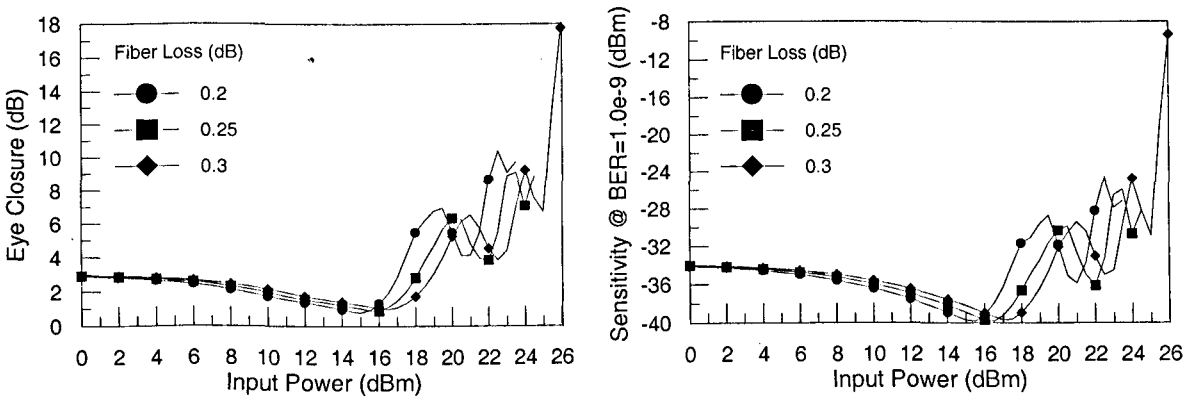

(a) (b)

Figure 4.1: (a) Eye closure penalty and (b) receiver sensitivity for 100 km transmission versus average transmitter power with fibre loss as a parameter.

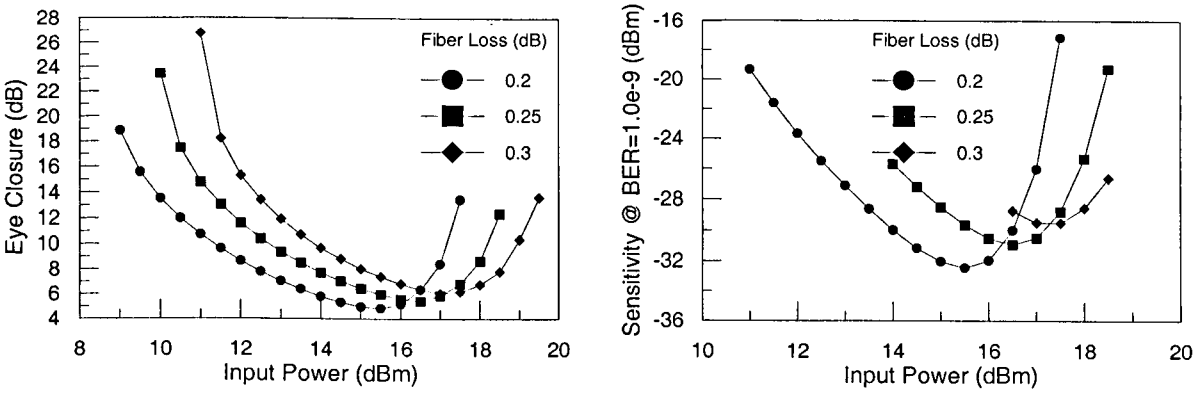

(a) (b)

Figure 4.2: (a) Eye closure penalty and (b) receiver sensitivity for 150 km transmission versus average transmitter power with fibre loss as a parameter.

4.1.2 Variation of fibre effective core area

Fig. 4.3 shows the (a) eye closure penalty, and (b) receiver sensitivity of the OPRs for 100 km transmission versus the average transmitter power for 5 different fibre effective core area (70, 75, 80, 85 and 90 μm^2). At very high transmitter power, the sensitivity has a rapid increase in penalty. The curves have similar shapes for different fibre effective core areas but the optimum transmitter power increases with an increasing fibre effective core area. The optimum sensitivities are nearly the same for different fibre effective core area. The sensitivity has a ripple when the transmitter power exceeded a certain level which increases with an increasing fibre effective core area. The allowable transmitter power range increases with an increasing fibre effective core area.

Fig. 4.4 shows the eye closure penalty (a) and receiver sensitivity of the OPRs (b) for 150 km transmission versus the average transmitter power for 5 different fibre effective core area (70, 75, 80, 85 and 90 μm^2). At very high transmitter power, the sensitivity has

a rapid increase in penalty. The eye closes completely for high transmitter power which depends on the fibre effective core area. The curves have similar shapes for different fibre effective core areas but the optimum transmitter power increases with an increasing fibre effective core area. The optimum sensitivities and allowable transmitter power ranges are very close for different fibre effective core areas.

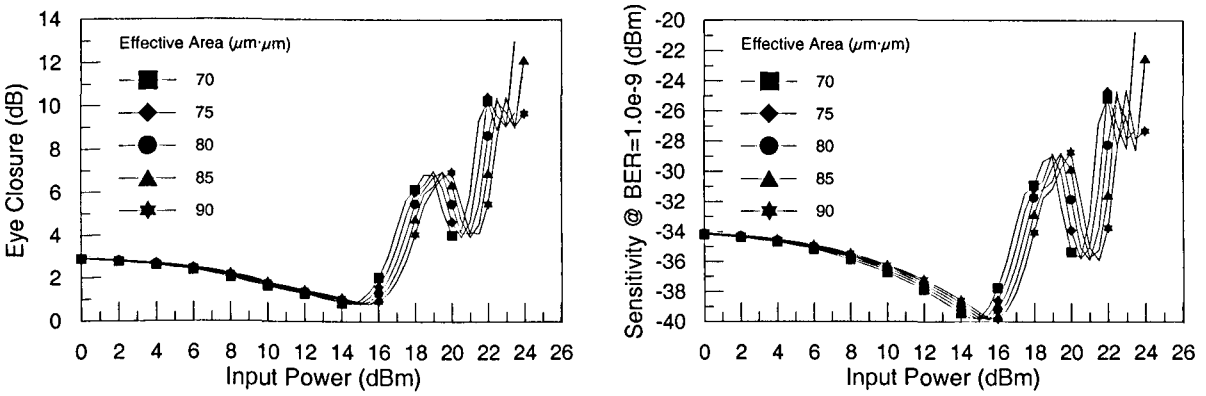

(a) (b)

Figure 4.3: (a) Eye closure penalty, and (b) receiver sensitivity for 100 km transmission versus average transmitter power with fibre effective core area as a parameter.

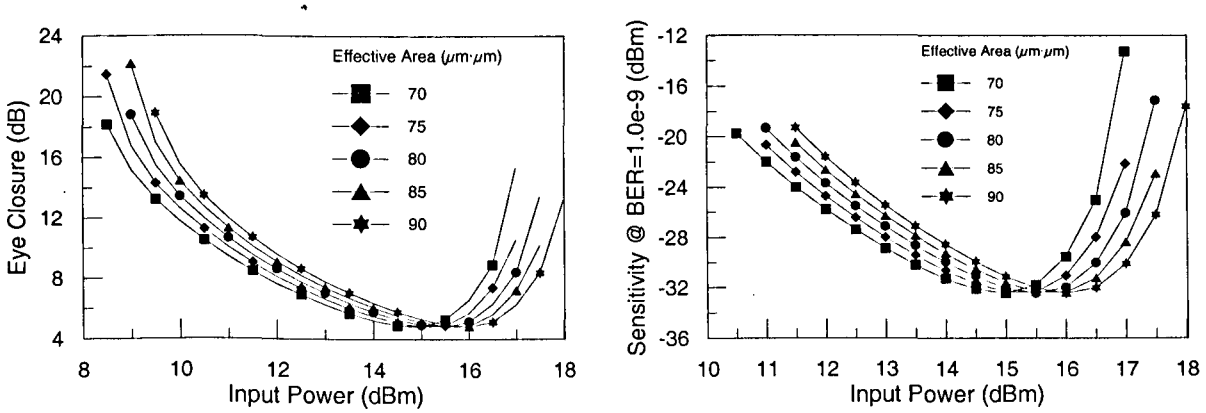

(a) (b)

Figure 4.4: (a) Eye closure penalty, and (b) receiver sensitivity for 150 km transmission versus average transmitter power with fibre effective core area as a parameter.

4.1.3 Variation of fibre dispersion

Fig. 4.5 shows the eye closure penalty (a) and receiver sensitivity of the OPRs (b) for 100 km transmission versus the average transmitter power for 3 different fibre dispersion (15, 17, and 19 ps/nm/km). At very high transmitter power, the sensitivity has a rapid increase in penalty. The curves have similar shapes for different fibre dispersions but the optimum sensitivity increases in penalty with an increasing fibre dispersion. The optimum transmitter powers for different fibre dispersions are very close, around 15.5 dBm. The sensitivity has a ripple when the transmitter power exceeded about 19 dBm. The allowable transmitter power ranges are very close for different fibre dispersions.

Fig. 4.6 shows the eye closure penalty (a) and receiver sensitivity of the OPRs (b) for 150 km transmission versus the average transmitter power for 3 different fibre dispersion (15, 17, and 19 ps/nm/km). At very high transmitter power, the sensitivity has a rapid increase in penalty. The eye closes completely for low transmitter power and high transmitter power which is critically dependent on the fibre dispersion. The optimum sensitivity increases in penalty fast and the allowable transmitter power range decreases fast with an increasing fibre dispersion. The optimum transmitter powers are close, around 15.5 dBm for different fibre dispersions.

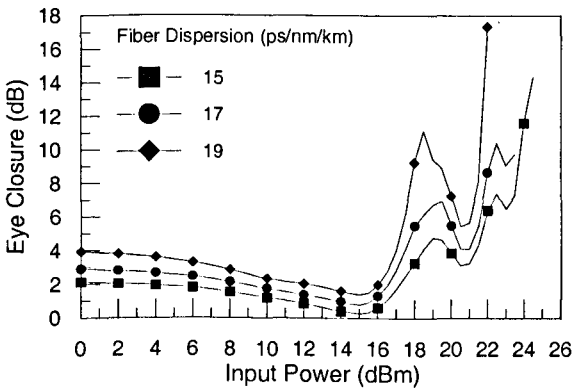

(a)

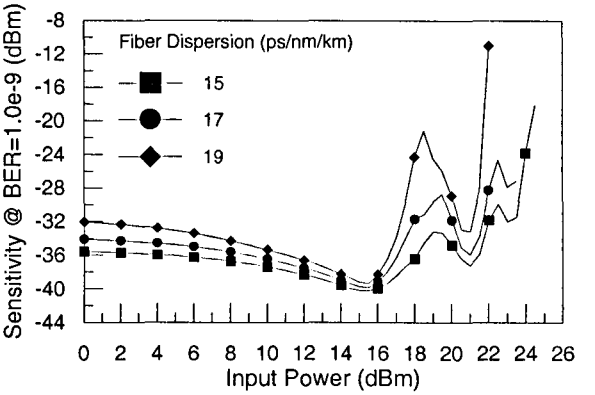

(b)

Figure 4.5: Eye closure penalty (a) and receiver sensitivity (b) for 100 km transmission versus average transmitter power with fibre dispersion as a parameter.

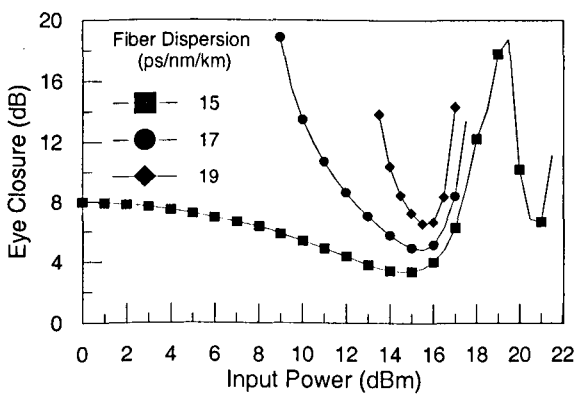

(a)

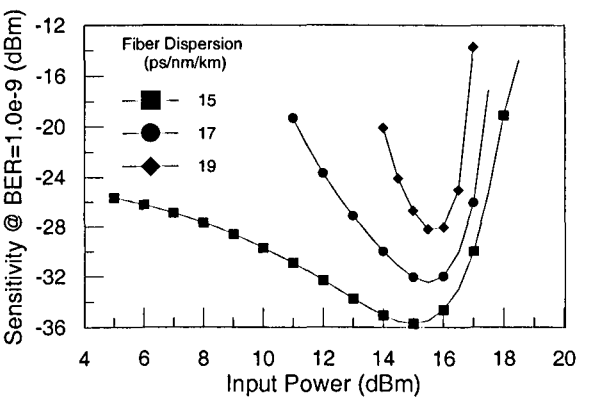

(b)

Figure 4.6: Eye closure penalty (a) and receiver sensitivity (b) for 150 km transmission versus average transmitter power with fibre dispersion as a parameter.

4.2 Influence of prechirp

In this section, it will be shown that the fibre dispersion can be partially compensated by the negative prechirp. The influence of prechirp in optical transmission is studied by varying the chirp parameter from -1.0 to 1.0 and the transmitter power from 0 to where the eye closes completely.

The chirp parameter used corresponds to the degree of asymmetry of the frequency chirp of an optical pulse. The frequency chirp mentioned in this section is simulated as the chirp from an asymmetrically driven Mach-Zehnder modulator, where the obtainable values of chirp parameter is limited to the range from -1 to +1, corresponding to the two situations with single-ended modulation. A negative chirp (i.e. negative chirp parameter) corresponds to a blueshift on the leading edge of the pulse and a redshift on the trailing edge of the pulse, i.e., the frequency chirp is positive on the leading edge and negative on the trailing edge. For a positive chirp (i.e. positive chirp parameter), the frequency chirp is just opposite to that for a negative chirp. Fig. 4.7 shows the super-Gaussian pulses (M=1 and 3) and raised-cosine pulse (rise time of 20 and 40 ps) and the corresponding frequency chirp for two opposite chirp parameters (+1.0 and -1.0) respectively. It is shown from the figures that the steep edge produces more frequency chirp.

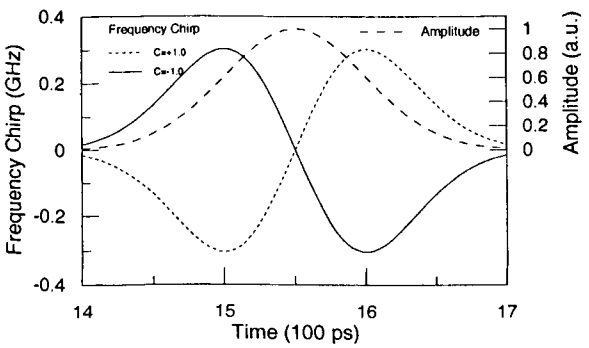

(a)

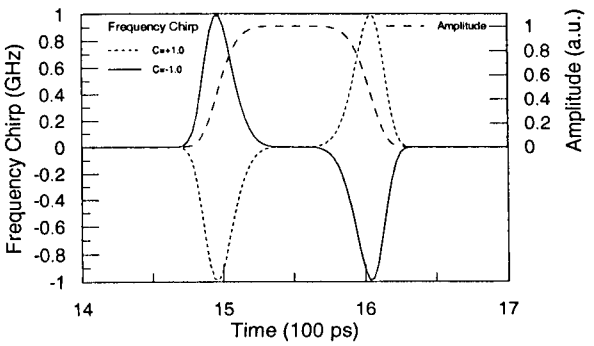

(b)

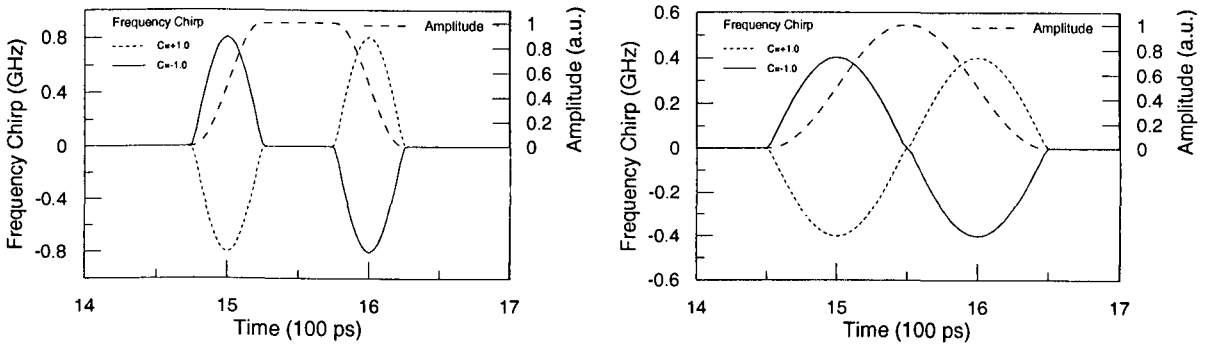

Figure 4.7: Input amplitude and frequency chirp of Mach-Zehnder modulator for super-Gaussian pulses ((a) for M=1 and (b) for M=3) and raised-cosine pulses ((c) for rise time of 20 ps and (d) for rise time of 40 ps)

Fig. 4.8 shows the eye closure penalty (a) and receiver sensitivity of the OPRs (b) for 100 km transmission versus the average transmitter power for 5 different chirp parameters (-1.0, -0.4, 0, 0.4 and 1.0). Fig. 4.9 shows the contour curves of eye closure penalty (a) and receiver sensitivity of the OPRs (b) for 100 km transmission versus the average transmitter power and chirp parameter. The optimum transmitter power increases with a decreasing chirp parameter. For the transmitter power lower than the optimum, the better sensitivity is obtained by the larger chirp parameter. For the transmitter power higher than the optimum, the sensitivity penalty increases fast with an increasing transmitter power. The sensitivity has a ripple when the transmitter power exceeded a certain level which depends on the chirp parameter. The optimum sensitivity is -39.9 dBm at the transmitter power of 15.5 dBm and chirp parameter of 0, but the largest system gain of 56.2 dB is obtained at the transmitter power of 17 dBm and chirp parameter of -0.8. The optimum receiver sensitivity occurs around the chirp parameter of 0 because the SPM-induced frequency chirp is small and the prechirp is not expected for short distance transmission. The allowable transmitter power range increases with an increasing chirp parameter.

The BER curves of the optimum sensitivity for 100 km transmission and the corresponding back-to-back case is shown in Fig. 4.12. The sensitivity for 100 km transmission is 1.4 dB worse than that for back-to-back with the same transmitter and receiver parameters.

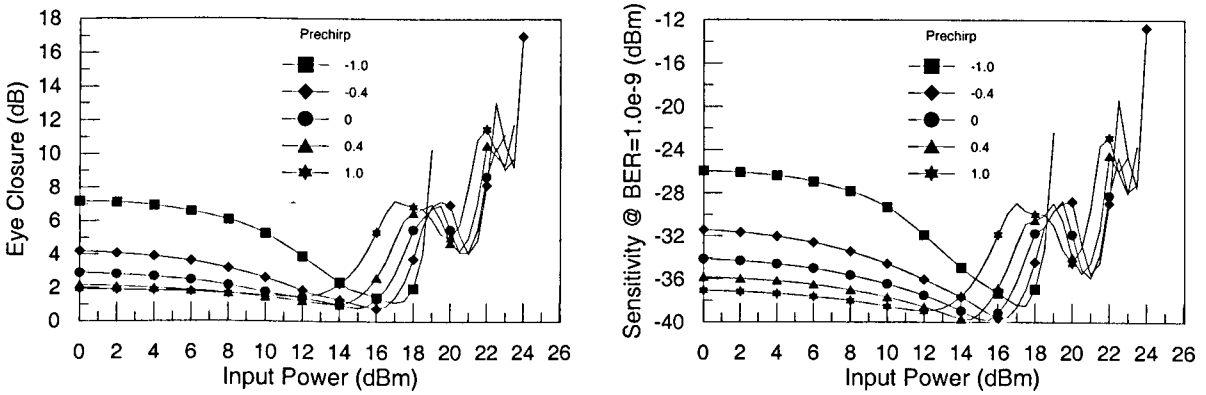

(a) (b)

Figure 4.8: Eye closure penalty (a) and receiver sensitivity of the OPR (b) for 100 km transmission versus average transmitter power with chirp parameter as a parameter.

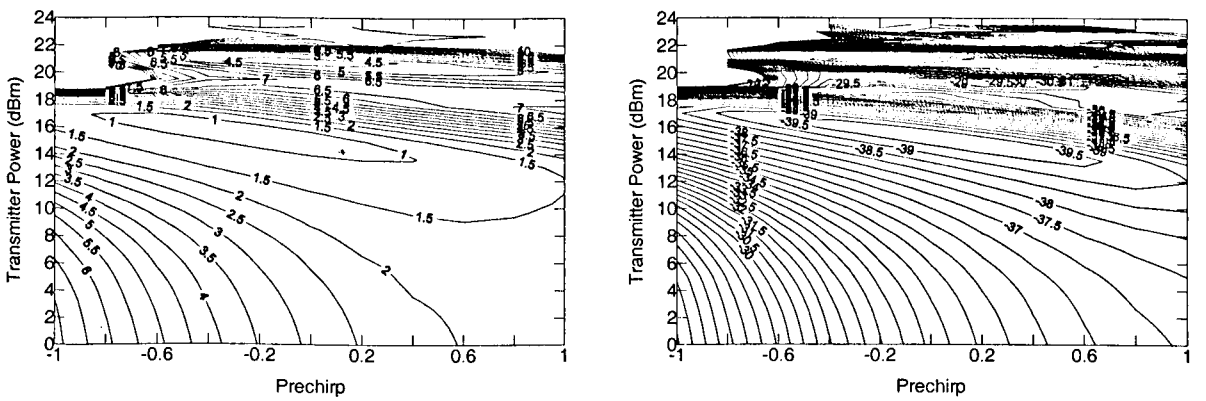

(a) (b)

Figure 4.9: Contour curves of eye closure penalty (a) and receiver sensitivity of the OPR (b) for 100 km transmission versus chirp parameter and average transmitter power.

Fig. 4.10 shows the eye closure penalty (a) and receiver sensitivity of the OPRs (b) for 150 km transmission versus the average transmitter power for 5 different chirp parameters (-1.0, -0.4, 0, 0.4 and 1.0). Fig. 4.11 shows the contour curves of eye closure penalty (a) and receiver sensitivity of the OPRs (b) for 150 km transmission versus the

average transmitter power and chirp parameter. The optimum transmitter power increases with a decreasing chirp parameter. A great sensitivity improvement is obtained by using a negative prechirp. For the transmitter power lower than the optimum the sensitivity penalty increases not very fast with a decreasing transmitter power. For the transmitter power higher than the optimum the sensitivity penalty decreases fast with an increasing transmitter power. The optimum sensitivity and the largest system gain of are obtained to be -34.7 dBm and 52.2 dB, respectively, at the transmitter power of 17.5 dBm and chirp parameter of -1.0. The optimum transmitter power becomes higher and the optimum chirp parameter becomes negative for 150 km transmission because the transmission distance is long and more chirp compensation is expected. The allowable transmitter power range increases with an increasing chirp parameter.

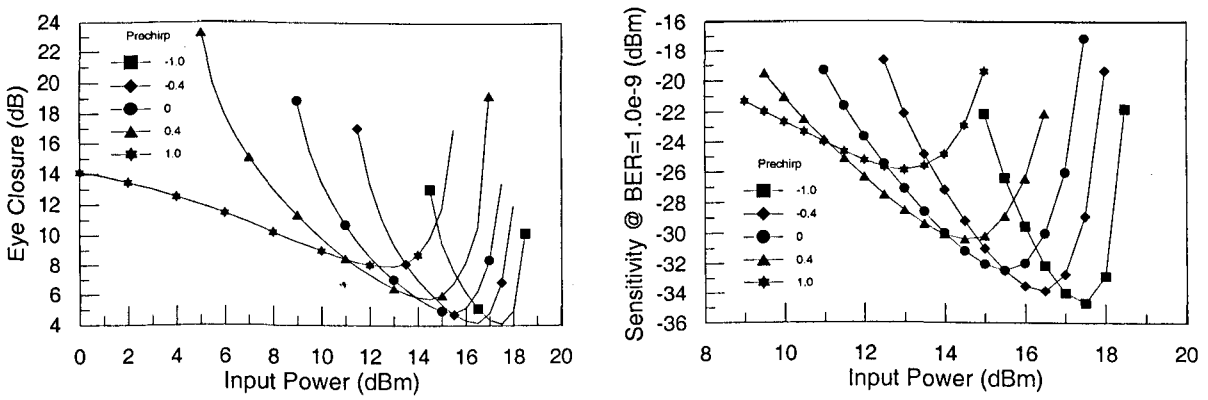

(a) (b)

Figure 4.10: Eye closure penalty (a) and receiver sensitivity of the OPR (b) for 150 km transmission versus average transmitter power with chirp parameter as a parameter.

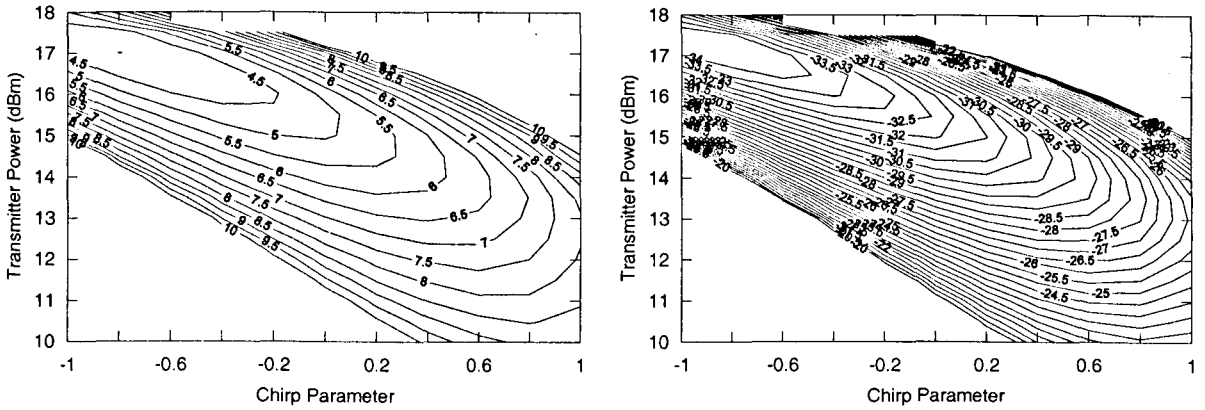

Figure 4.11: Contour curves of eye closure penalty (a) and receiver sensitivity of the OPR (b) for 150 km transmission versus chirp parameter and average transmitter power.

The BER curves of the optimum sensitivity for 150 km transmission and the corresponding back-to-back case is shown in Fig. 4.12. It shows that the slope of the BER curve for long distance transmission is slightly different from the back-to-back case. The sensitivity for 150 km transmission is 6.5 dB worse than that for back-to-back with the same transmitter and receiver parameters.

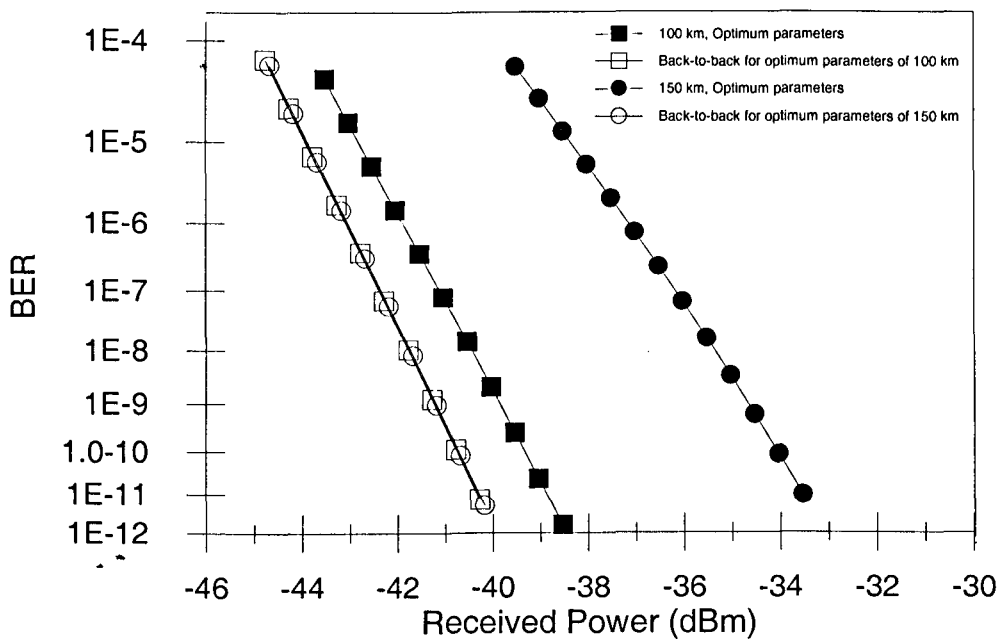

Figure 4.12: BER curves for the optimum sensitivity of 100 km and 150 km transmissions and the corresponding back-to-back cases, calculated for the optimum prechirp and the optimum transmitter power.

It is shown from the simulations carried out in this section that the prechirp is not necessary for the short distance transmission but for long distance transmission the big sensitivity improvements are obtained by using negative prechirp. The optimum transmitter power increases a great deal but the allowable transmitter power range decreases with a decreasing chirp parameter.

4.3 Influence of rise time

To clarify the influence of rise time, the simulations are carried out for varying transmitter power and rise time from 10 to 40 ps. The maximum rise time for a perfect raised-cosine pulse is around 41 ps. The investigation is performed by chirp-free pulses. Fig. 4.13 shows the eye closure penalty (a) and receiver sensitivity of the OPRs (b) versus the average transmitter power for 4 different rise times (10, 20, 30 and 40 ps) for 100 km transmission and a chirp-free input. Fig. 4.14 shows the contour curves of eye closure penalty (a) and receiver sensitivity of the OPR (b) versus the average transmitter power and rise time for 100 km transmission and a chirp-free input. The optimum sensitivities and the optimum transmitter powers are very close for different rise times. For the transmitter power lower than the optimum, the sensitivity difference is small for different rise times and the better sensitivity is obtained for shorter rise time. For the transmitter power higher than the optimum, the sensitivity penalty increases fast with an increasing transmitter power. The sensitivity has a ripple when the transmitter power exceeds a certain level, around 19 dBm, and the rise time is less than 30 ps. No sensitivity ripple is found for the rise time of 40 ps. The optimum sensitivity is -40.1 dBm at the transmitter power of 15 dBm and rise time of 40 ps.

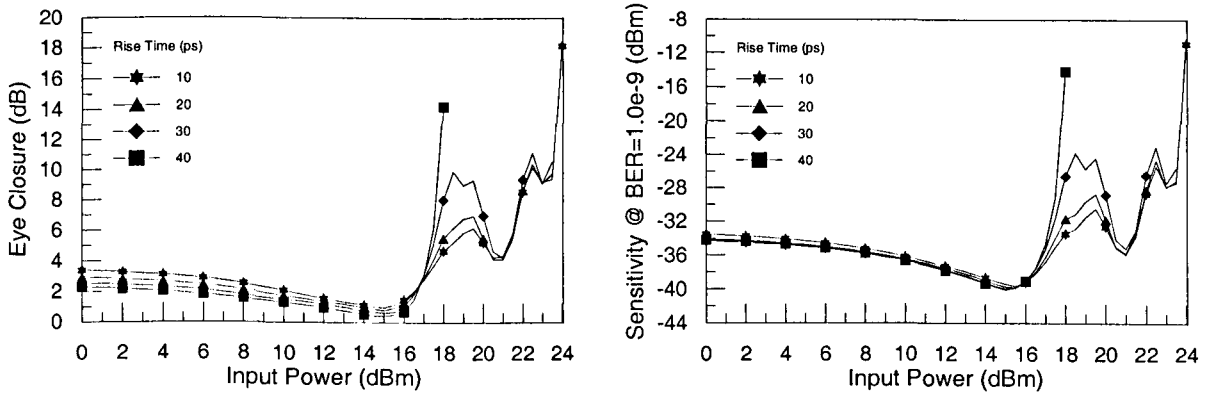

(a) (b)

Figure 4.13: Eye closure penalty (a) and receiver sensitivity (b) for 100 km transmission versus average transmitter power with rise time as a parameter for chirp-free input.

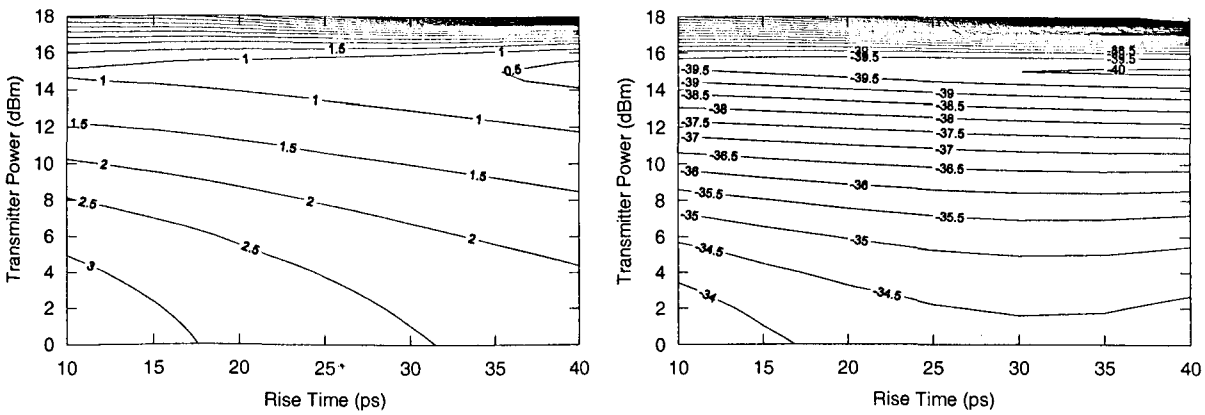

(a) (b)

Figure 4.14: Contour of eye closure penalty (a) and receiver sensitivity (b) for 100 km transmission versus transmitter power and rise time for a chirp-free input.

The BER curves of the optimum sensitivity for 100 km transmission and the corresponding back-to-back case is shown in Fig. 4.17. The sensitivity for 100 km transmission is 0.3 dB worse than that for back-to-back with the same transmitter and receiver parameters.

Fig. 4.15 shows the eye closure penalty (a) and receiver sensitivity of the OPRs (b) versus the average transmitter power for 4 different rise times (10, 20, 30 and 40 ps) for 150 km transmission and a chirp-free input. Fig. 4.16 shows the contour curves of eye closure penalty (a) and receiver sensitivity of the OPR (b) versus the average transmitter power and rise time for 150 km transmission and a chirp-free input. The optimum sensitivity becomes better for larger rise time. The optimum transmitter power decreases slightly with an increasing rise time. For the transmitter power lower than the optimum, the sensitivity penalty increases, not very fast, with a decreasing transmitter power and the better sensitivity is obtained for larger rise time. For the transmitter power higher than the optimum, the sensitivity penalty increases fast with an increasing transmitter power. The eye closes completely for low transmitter powers and high transmitter powers which are dependent on different rise time. The optimum sensitivity is -35.5 dBm at the transmitter power of 15 dBm and rise time of 40 ps. The allowable transmitter power range increases with an increasing rise time.

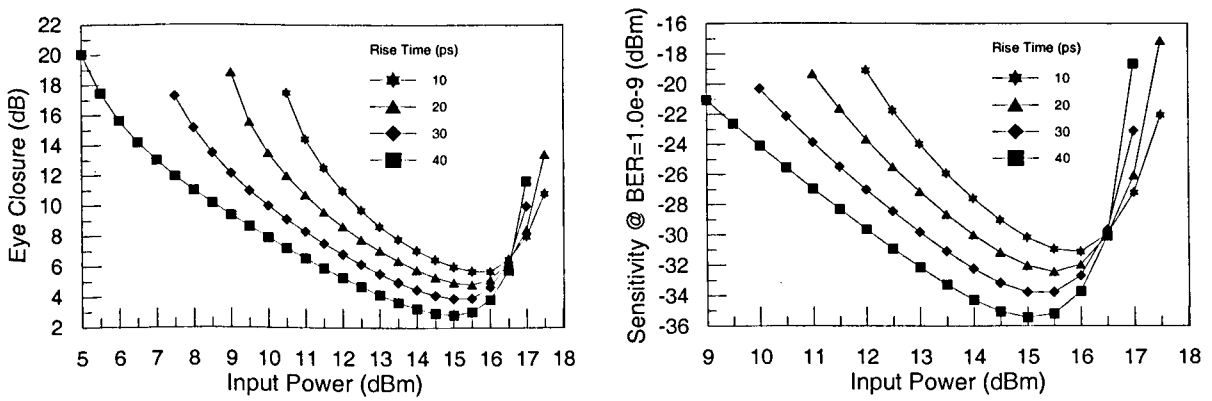

(a) (b)

Figure 4.15: Eye closure penalty (a) and receiver sensitivity (b) for 150 km transmission versus average transmitter power with rise time as a parameter for chirp-free input.

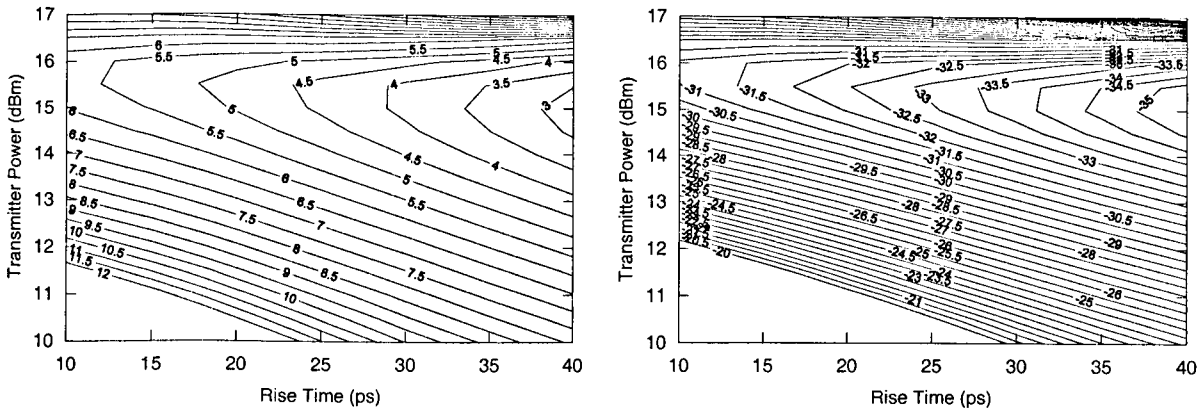

(a) (b)

Figure 4.16: Contour of eye closure penalty (a) and receiver sensitivity (b) for 150 km transmission versus transmitter power and rise time for a chirp-free input.

The BER curves of the optimum sensitivity for 150 km transmission and the corresponding back-to-back case is shown in Fig. 4.17. It shows that the slope of the BER curve is slightly different from the back-to-back case. The sensitivity for 150 km transmission is 4.9 dB worse than that for back-to-back with the same transmitter and receiver parameters.

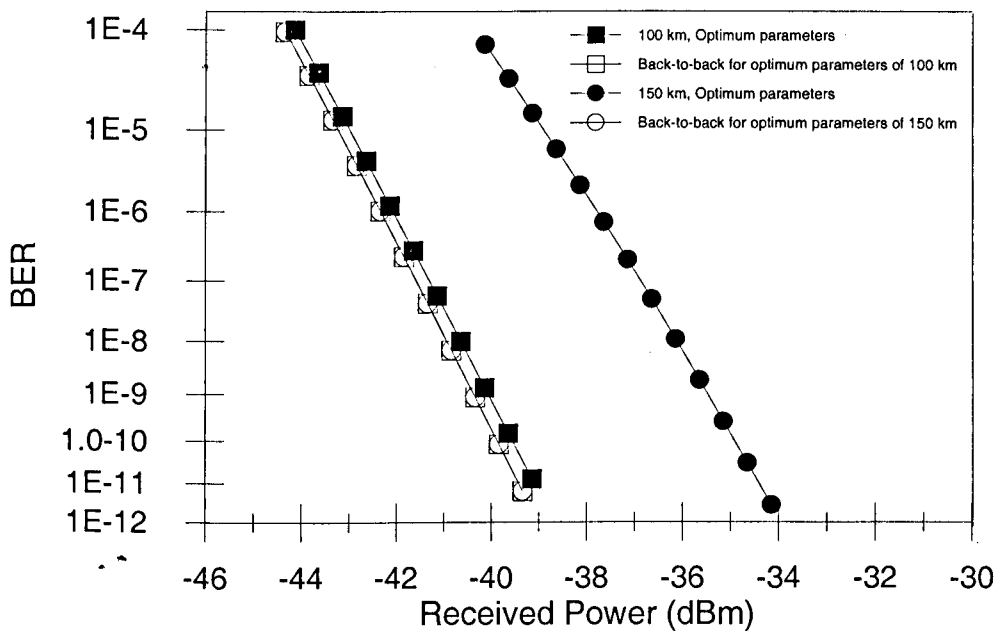

Figure 4.17: BER curves for the optimum sensitivity of 100 km and 150 km transmissions and the corresponding back-to-back cases, calculated for a chirp-free input, optimum rise time and optimum transmitter power

For a short transmission distance, the influence on sensitivity of the rise time is not serious, the optimum sensitivity and the optimum transmitter power have very slight difference for different rise times. For a long transmission distance, a serious influence on sensitivity of the rise time is found. For a chirp-free input, the optimum sensitivity becomes much better but the optimum transmitter power decreases when rise time increases. The better sensitivity is obtained by larger rise times for low transmitter power (than the optimum). The allowable transmitter power range increases with an increasing rise time.

4.4 Influence of extinction ratio

The extinction ratio were fixed to be infinite for the previous simulations in this chapter. When we consider nonlinear transmission in optical fibre, the input signal with a finite extinction ratio can provide a receiver sensitivity improvement due to SPM effect [1,2]. This is because a certain amount of energy is presented in the zero's bits for the input signal with a finite extinction ratio. When it transmits in fibre, SPM causes a compression of the one's bits, while the energy of the zero's bits is transferred into the neighbouring bits, effectively causing the energy level of the zero's bits to be decreased, and the energy level of the one's bits to be increased at the same time. Then, the eye opening of the received signal can be improved, even better than the input in some cases. Consequently, the receiver sensitivity is improved.

The amount of SPM generated frequency chirp is proportional to the difference in power between zero's and one's bits. The average power is given by:

$$P_{av} = \frac{P_1 + P_0}{2} = P_1 \frac{1+r}{2r} \tag{4.1}$$

where P_1 and P_0 are the power level of the one's bit and zero's bit respectively. The difference in power between the one's and zero's is then given by:

$$\Delta P = P_1 - P_0 = 2P_{av} \frac{r-1}{r+1} \tag{4.2}$$

Therefore, the SPM-induced maximum frequency chirp Δf_{max} has [3]:

$$\Delta f_{max} \propto \frac{r-1}{r+1} \tag{4.3}$$

It shows that the amount of SPM is decreased with a decreasing extinction ratio.

For discussing the influence of the extinction ratio, the simulations of an ASK system are carried out. The ASK modulator is Mach-Zehnder modulator. The extinction ratio is varied by the asymmetrical parameter, switching voltage, and modulation voltage of the modulator [4].

The influence of extinction ratio is respectively investigated by varying the transmitter power and the extinction ratio from 3 dB to 20 dB. The investigations are performed by the input signals with chirp-free pulses.

Fig. 4.18 shows the sensitivity for chirp free as a function of transmission distance for the extinction ratio of infinity and 10 dB. It shows that the sensitivity is better for infinite extinction ratio than for the extinction ratio of 10 dB when transmission distance is less than 110 km and it gives opposite result for longer distance. The sensitivity penalty increases with an increasing distance for infinite extinction ratio and this increase is very fast after 120 km transmission. For the extinction ratio of 10 dB the sensitivity penalty is

less than 1 dB for the distance within 140 km and the penalty increases very fast after 150 km transmission. It shows that the sensitivity can be improved by the finite extinction ratio input after a certain distance transmission, e.g. 110 km for this case.

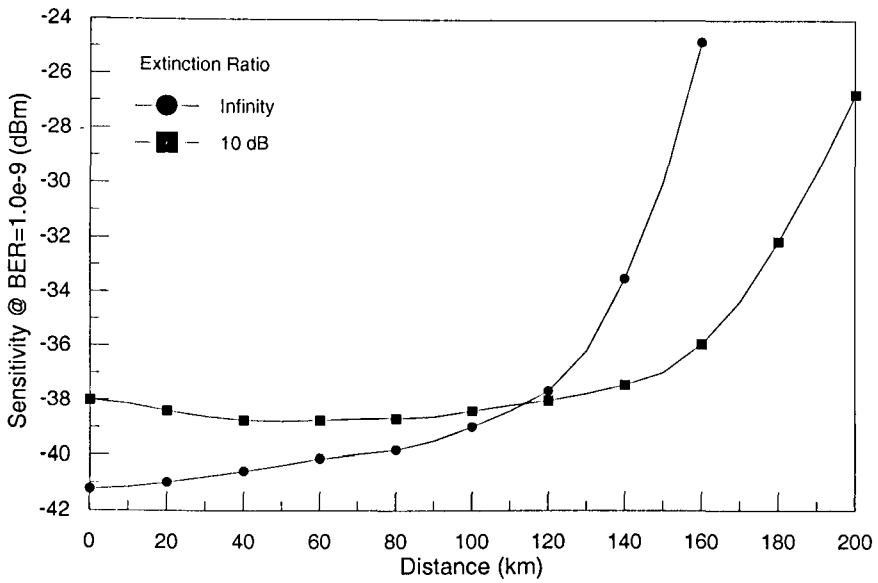

Figure 4.18: Sensitivity as a function of transmission distance for extinction ratio of infinity and 10 dB with a chirp-free input, calculated for transmitter power of 14 dBm.

Fig. 4.19 shows the contour of receiver sensitivity versus the average transmitter power and extinction ratio for a chirp-free input signal, in which (a) and (b) are respectively for 100 km and 150 km transmissions.

For 100 km transmission, the optimum sensitivity is -40.3 dBm at the extinction ratio of 16 dB and the transmitter power of 15.5 dBm. The optimum sensitivity is nearly the same for extinction ratio larger than 15 dB. This is because this transmission distance is shorter and the effect of extinction ratio is small. The sensitivity is very sensitive to the low extinction ratio. The allowable transmitter power range increases with an increasing extinction ratio.

For 150 km transmission, the optimum sensitivity is -38.2 dBm at the extinction ratio of 11 dB and the transmitter power of 15 dBm. The sensitivity is sensitive to extinction ratio and transmitter power. This is caused by SPM and the effect of extinction ratio. It shows the optimum extinction ratio decreases when the transmission distance is longer. The maximum allowable transmitter power range shifts to a certain extinction ratio which is dependent on the transmission distance.

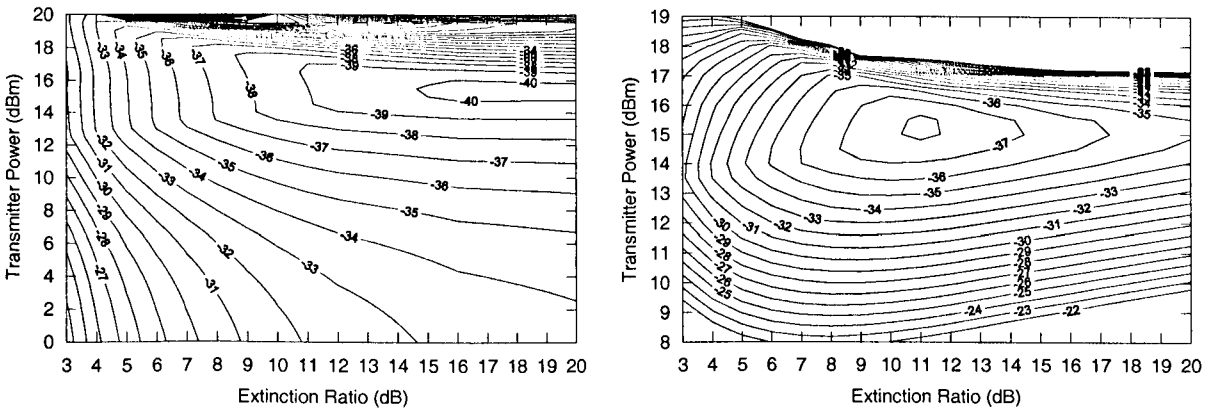

(a) (b)

Figure 4.19: Contour of receiver sensitivity versus transmitter power and extinction ratio for a chirp-free input signal and 100 km (a) and 150 km (b) transmissions.

Fig. 4.20 shows the eye-diagrams for back-to-back (a) and 100 km transmission (b), simulated by the system parameters corresponding to the optimum sensitivity in Fig. 4.19(a). The eye closure penalty is 0.3 dB compared to the back-to-back case.

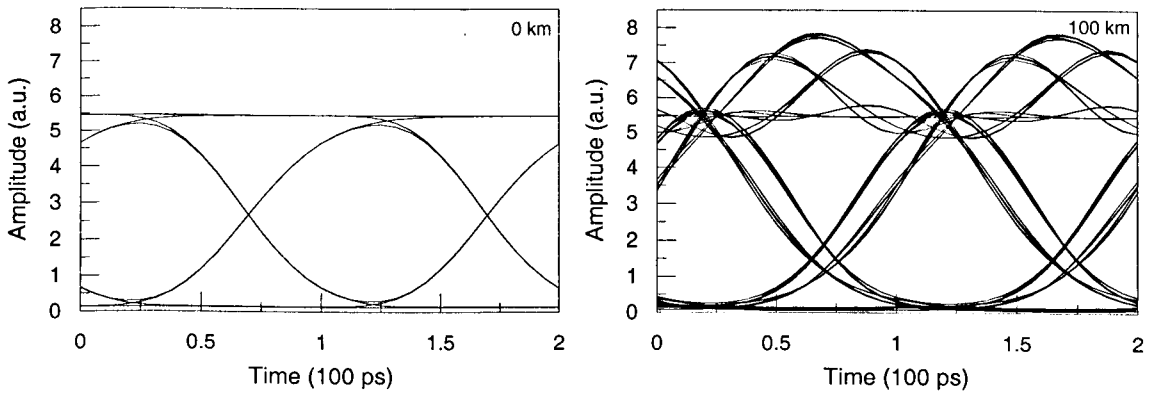

(a) (b)

Fig. 4.20: Eye-diagrams for back-to-back (a) and 100 km transmission (b), simulated by the system parameters corresponding to the optimum sensitivity in Fig. 5.3.37(a).

Fig. 4.21 shows the eye-diagrams for back-to-back (a) and 150 km transmission (b) simulated by the system parameters corresponding to the optimum sensitivity in Fig. 4.19(b). The eye closure penalty is 1.1 dB compared to the back-to-back case.

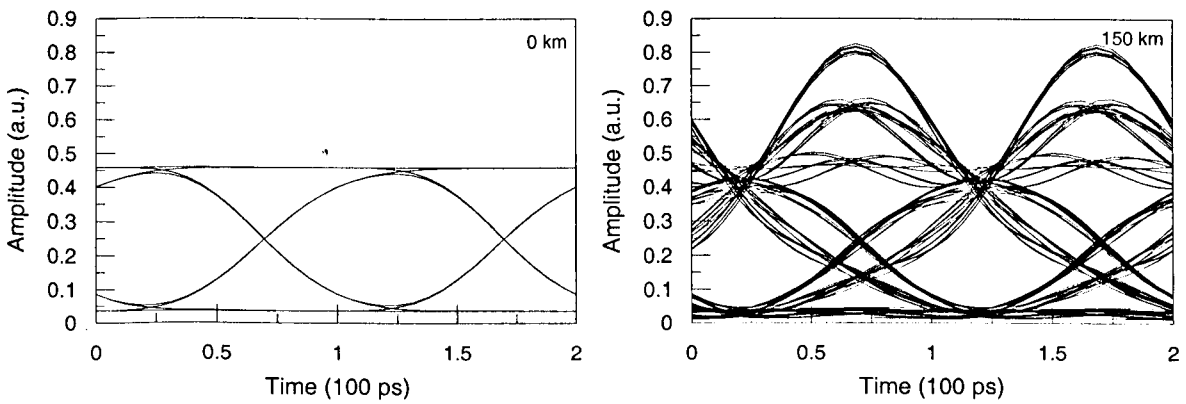

(a) (b)

Fig. 4.21: Eye-diagrams for back-to-back (a) and 150 km transmission (b), simulated by the system parameters corresponding to the optimum sensitivity in Fig. 5.3.37(b).

Fig. 4.22 shows the BER curves of the optimum sensitivity for 100 km transmission and the corresponding back-to-back case, calculated by the same system parameters as Fig. 4.20. The sensitivity for 100 km transmission is 0.3 dB better than that for the back-to-

back case. The BER curves of the optimum sensitivity for 150 km transmission and the corresponding back-to-back case are also shown in Fig. 4.22, calculated by the same system parameters as Fig. 4.21. It shows that the slope of the BER curve is slightly different for long transmission distance. The sensitivity for 150 km transmission is 0.3 dB worse than that for the back-to-back case.

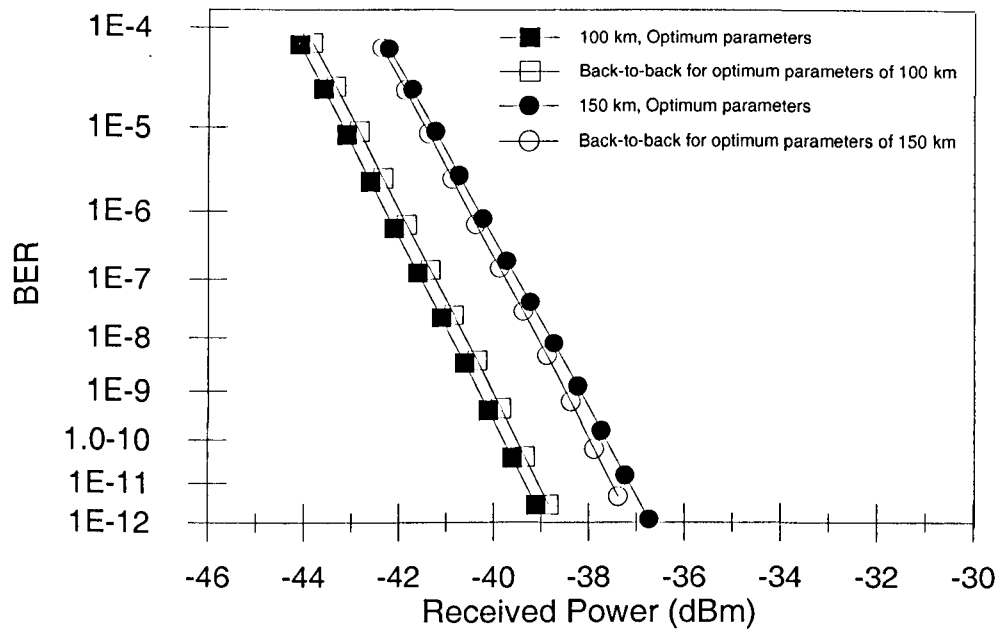

Figure 4.22: BER curves for the optimum sensitivity of 100 km and 150 km transmissions and the corresponding back-to-back cases, calculated for a chirp-free input, optimum extinction ratio and optimum transmitter power

4.5 Influence of sequence length

In this section, a serial of simulations are carried out to investigate the influence of the sequence length of the input signal used in the simulations of optical nonlinear transmission.

Fig. 4.23 shows the sensitivity as a function of the sequence length of the input signal with prechirp of -0.5, 0 and +0.5 for 100 km (a) and 150 km (b) transmissions. The 5th order Bessel electrical filter and the 5th order Butterworth electrical filter are used in simulations, respectively. For 100 km transmission, the inputs with prechirp of 0, -0.5 and +0.5 have transmitter powers of 15.4, 16.5 and 14 dBm and extinction ratio of infinity, respectively. For 150 km transmission, the inputs with prechirp of -0.5, 0 and +0.5 have transmitter powers of 16.5, 15 and 13 dBm and extinction ratios of 12, 11 and 10 dB, respectively.

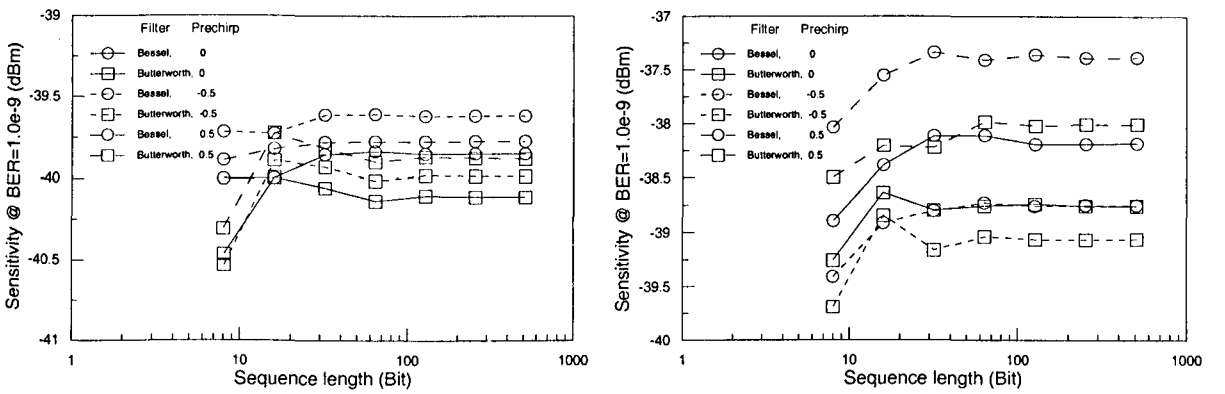

(a) (b)

Figure 4.23: Receiver sensitivity as a function of sequence length for the 5th order Bessel filter and the 5th order Butterworth filter for 100 km (a) and 150 km (b) transmissions.

It shows that the influence on the receiver sensitivity of the sequence length is much more serious than the back-to-back case because of fibre dispersion and SPM. The sensitivity difference for different sequence length increases with an increasing transmission distance. The difference for the 5th order Bessel filter is smaller than the 5th order Butterworth filter since the latter has a large group delay variation. For all the cases in Fig. 4.23, the sensitivity difference for different sequence lengths is very small when the sequence length used is longer than 128-bits. This means that a 128-bits PRBS is reasonable for the simulations when accuracy and calculation time are traded off.

4.6 Summary

In this chapter, the influence of the variation in fibre parameters including fibre loss, dispersion and fibre effective core area are investigated. The results are important for the system designer.

Prechirp is not necessary for the short distance transmission but for a long distance transmission a big sensitivity improvement is obtained by using negative prechirp. The optimum transmitter power increases greatly but the allowable transmitter power range decreases with a decreasing chirp parameter.

The influence on sensitivity of the rise time is not serious for the short transmission distances. The optimum sensitivity and the optimum transmitter power have very slight difference for different rise times. For a long transmission distance, a serious influence on sensitivity of the rise time is found. The optimum sensitivity becomes much better, the optimum transmitter power decreases and the allowable transmitter power range increases with an increasing rise time for a chirp-free input.

The receiver sensitivity can be improved by an input with finite extinction ratio after a certain distance transmission. For a short transmission distance, the sensitivity nearly keeps constant for the extinction ratio over a certain value. For a long transmission distance, the optimum extinction ratio decreases when the transmission distance is longer. The maximum allowable transmitter power range shifts to a certain extinction ratio which is dependent on the transmission distance.

The influence of the sequence length used in simulations is studied by using a 5th order Bessel electrical filter and a 5th order Butterworth electrical filter for 100 km and 150 km transmissions. It shows that a big receiver sensitivity difference is caused by short sequence length used but the sensitivity difference is very small when the sequence length used is longer than 128-bits. Thus, a 128-bits PRBS is reasonable for the transmission simulations when accuracy and calculation time are compromised.

Chapter 5

Dispersion Management for WDM Systems

In an optical fibre communication system, information is transmitted over a fibre by using a coded sequence of optical pulses whose width is determined by the bit rate B of the system. Dispersion-induced broadening of pulses is undesirable as it interferes with the detection process and leads to errors if the pulse spreads outside its allocated bit slot ($T_B = 1/B$). Due to GVD-induced limitations, 10 Gb/s WDM transmissions over ITU-T G.652 fibre (CSMF) at the wavelength of 1.55 μm are very difficult with the fibre length longer than 100 km; Due to FWM effect, ITU-T G.653 fibre (DSF) is not suitable for WDM transmission at its zero-dispersion wavelength, 1.55μm; ITU-T G.655 fibre (NZDF) shifts its zero-dispersion wavelength to either under 1540nm or over 1565nm, can be divided into two catalogues: NZDF(D>0) and NZDF(D<0), distinguished by the sign of its dispersion at the wavelength of 1550 nm. The applying of NZDF suppresses the FWM crosstalk in WDM systems, but is not sufficient to compensate the GVD and its interplay with XPM and SPM, without further dispersion

managing schemes. Thus, dispersion management is a key-technique for WDM transmissions at bit rate of 10 Gb/s or even higher over long fibre length.

In this chapter, the GVD-induced limitations are investigated. Several dispersion management schemes are presented. The influence of XPM and SPM effects on WDM transmission systems applying dispersion management are investigated. The noise amplification in a dispersion-managed WDM transmission system induced by modulation instability (MI) is investigated. Finally, example of dispersion management for 16-channel WDM transmission systems is presented.

5.1 GVD-induced limitations

The dispersion problem becomes quite serious when optical amplifiers are used to compensate for fibre losses because transmission distance L can exceed thousands of kilometres for long-haul systems. A useful measure of the information-transmission capacity is the bit rate-distance product BL. This section discusses how the BL product is limited by fibre dispersion.

Consider first the case in which pulse broadening is dominated by the large spectral width σ_ω of the source. For a Gaussian pulse, the broadening factor is given by [1]:

$$\frac{\sigma^2}{\sigma_0^2}=\left(1+\frac{C\beta_2 z}{2\sigma_0^2}\right)^2+(1+V_\omega^2)\left(\frac{\beta_2 z}{2\sigma_0^2}\right)^2+(1+C^2+V_\omega^2)^2\frac{1}{2}\left(\frac{\beta_3 z}{4\sigma_0^3}\right)^2, \quad (5.1)$$

where σ_0 is the initial root-mean-square (RMS) width of the Gaussian pulse, $V_\omega = 2\sigma_\omega\sigma_0$ and σ_ω is the RMS width of the Gaussian source spectrum. Assuming that the contribution of the β_3 term is negligible together with $C = 0$ and $V_\omega >> 1$, the RMS pulse width σ is given by:

$$\sigma = [\sigma_0^2 + (\beta_2 L\sigma_\omega)^2]^{1/2} = [\sigma_0^2 + (DL\sigma_\lambda)^2]^{1/2}, \qquad (5.2)$$

where L is the fibre-link length and σ_λ is the RMS spectral width of the source in wavelength units. The dispersion parameter D is related to the GVD parameter β_2 as $D = -\frac{2\pi c}{\lambda_2}\beta_2$.

One can relate σ to the bit rate B by using the criterion that the broadened pulse should remain confined to its own bit slot ($T_B = 1/B$). A commonly used criterion is $4\sigma < T_g$ [2]; for a Gaussian pulse, at least 95% of the pulse energy remains within the bit slot when this condition is satisfied. The limiting bit rate is obtained using $4B\sigma < 1$. Assuming $\sigma_0 << \sigma$, this condition becomes:

$$BL|D|\sigma_\lambda < 1/4. \qquad (5.3)$$

As an illustration, consider the case of multimode semiconductor lasers [3] for which $\sigma_\lambda \approx 2$ nm. If the system is operating near $\lambda = 1.55$ μm using CSMF, $D \approx 17$ ps/km/nm. With these parameter values, Eq. (5.3) requires BL < 8 (Gb/s)·km. For a 100-km-long fibre, GVD restrict the bit rate to relatively low

values of only 80 Mb/s. However, if the system is designed to operate near the zero-dispersion wavelength (occurring near 1.3 μm) such that $D < 1$ ps/km/nm, the BL product increase to beyond 100 (Gb/s)·km.

Modern fibre-optic communication systems operating near 1.55 μm reduce the GVD effects using dispersion-shifted fibres (DSF) designed such that the minimum-loss wavelength and the zero-dispersion wavelengths nearly coincide. At the same time, lasers designed to operate in a single longitudinal mode are used such that the source spectral width is well below 100 MHz [3]. Under such conditions, $V_\omega << 1$ in Eq. (5.1). If we neglect the β_3 term and set $C = 0$, Eq. (5.1) can be approximated by:

$$\sigma = [\sigma_0^2 + (\beta_2 L / 2\sigma_0)^2]^{1/2}. \qquad (5.4)$$

A comparison with Eq. (5.2) reveals a major difference: Dispersion-induced broadening now depends on the initial width σ_0. In fact, σ can be minimized by choosing an optimum value of σ_0. The minimum value of σ is found to occur for $\sigma_0 = (|\beta_2| L/2)^{1/2}$ and is given by $\sigma = (|\beta_2| L)^{1/2}$. The limiting bit rate is obtained by using $4B\sigma < 1$ or the condition:

$$B(|\beta_2| L)^{1/2} < 1/4. \qquad (5.5)$$

The main difference from Eq. (5.3) is that B scales as $L^{-1/2}$ rather than L^{-1}. Figure 5.1 compares the decrease in the bit rate with increasing L by choosing D = 16 ps/km/nm and $\sigma_\lambda = 0$, 1 and 5 nm. Equation (5.5) was used in the case $\sigma_\lambda = 0$.

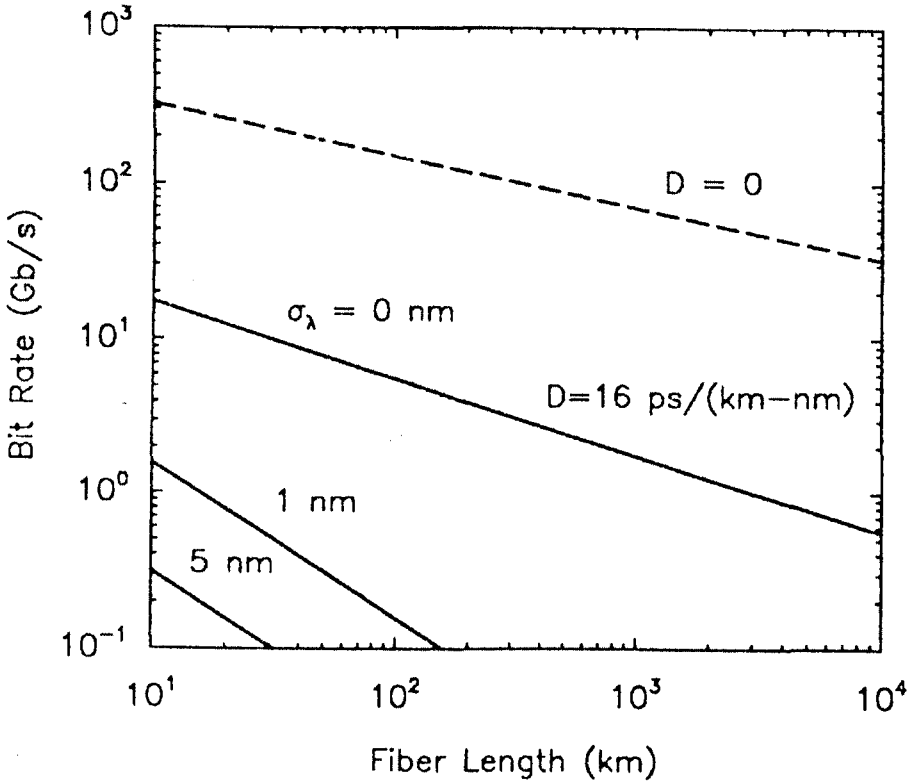

Figure 5.1: Limiting bit rate as a function of the fibre length for $\sigma_\lambda = 0$, 1 and 5 nm. The case $\sigma_\lambda = 0$ corresponds to an optical source whose spectral width is much smaller than the bit rate. Dashed line shows the case $\beta_2 = 0$.

For a lightwave system operating exactly at the zero-dispersion wavelength, $\beta_2 = 0$ in Eq. (5.1). Assuming $V_\omega << 1$ and $C = 0$, the pulse width is given by:

$$\sigma = [\sigma_0^2 + \frac{1}{2}(\beta_3 L / 4\sigma_0^2)^2]^{1/2}. \qquad (5.6)$$

Similar to the case of Eq. (5.4), σ can be minimized by optimising the input pulse width σ_0. The minimum value of σ_0 is found to occur for $\sigma_0 = (|\beta_3| L/4)^{1/3}$. The limiting bit rate is obtained by using the condition $4B\sigma < 1$ and is given by [2]:

$$B(|\beta_3|L)^{1/3} < 0.324 . \qquad (5.7)$$

The dispersive effects are most forgiving in this case. For a typical value $\beta_3 = 0.1\,\text{ps}^3/\text{km}$, the bit rate can be as large as 150 Gb/s for L = 100 km. It decreases to only 70 Gb/s even when L increases by a factor of 10 because of the $L^{-1/3}$ dependence of the bit rate on the fibre length. The dashed line in Fig. 5.1 shows this dependence using Eq. (5.7) with $\beta_3 = 0.1\,\text{ps}^3/\text{km}$. Clearly, the performance of a lightwave system can be considerably improved by operating it close to the zero-dispersion wavelength of the fibre.

5.2 Dispersion management schemes

The general approaches to dispersion management are through combination of positive and negative dispersion fibres. For dispersion management of C-band (1530 ~ 1565 nm) WDM transmission, there are four fibre-combination schemes:

(i) NZDF (D > 0) + DCF, (ii) CSMF + DCF

(iii) NZDF (D < 0) + CSMF, (iv) NZDF (D > 0) + NZDF (D < 0)

DCF used in schemes (i) and (ii) are dispersion compensation fibres with massive negative dispersion [4, 5, 6]. These two schemes use positive dispersion fibres for transmission, DCF's are inserted in transmitter, receiver, and line amplifiers, the length of which is not counted into the transmission distance. In scheme (iii), CSMF

takes part in transmission, and is normally cascaded before NZDF. This scheme helps suppressing the fibre nonlinear effects, but on the other hand, it introduces complexities in fibre laying-down, as two different fibres have to be distinguished in one transmission span. Scheme (iv) encounters the same advantage and disadvantage.

It is a comprehensive problem to choose a proper fibre-combination scheme for dispersion management, which has important influence on the selecting of fibre-type for a newly designed WDM transmission system. Comparing two catalogues of NZDF's, NZDF (D < 0) has the following shortcomings: (a) with the same manufacturing conditions and similar refractive index shapes, fibres with larger zero-dispersion wavelength have bigger fibre loss and smaller effective area A_{eff} [7]; (b) The zero-dispersion wavelength falls into the L band (1570 ~ 1610 nm) of EDFA, which is disadvantageous for the WDM transmission in this band; (c) SPM effect causes pulse broadening in negative dispersion fibres, for transmission systems without dispersion management (e.g., low bit-rate or short distance transmission), NZDF (D < 0) system has a worse performance than NZDF (D > 0). Long haul WDM transmission experiments demonstrate that, schemes (i) and (iv) have better performance than schemes (ii) and (iii), but scheme (iv) suffers the complexities of fibre laying-down. Thus, the author regards NZDF (D > 0) + DCF as generally the best fibre-combination scheme for dispersion management in WDM transmission systems.

Besides DCF, chirped optical fibre Bragg gratings can produce large negative dispersion as well. The major advantages of DCF are its wide compensating band (exceeding 40 nm), and its stability; the disadvantages are its large fibre loss and

enormous nonlinear effects, and the massive size of DCF rolls. The outstanding advantages of chirped Bragg grating are its tight construction and small loss, can be looked as ideal linear dispersion compensator; the major disadvantage is its narrow compensating band. From the author's point of view, DCF compensation is more suitable for NZDF transmission systems. As the compensation quantity needed in such systems is normally less than 800 ps/nm, the influence of DCF-induced loss and nonlinear effects is not serious.

In the following contents of this chapter, we only consider NZDF (D > 0) + DCF as the dispersion management scheme of WDM transmission systems. The dispersion parameter *D* of transmission fibres can vary from 1 to 20 ps/km/nm. Generally, distributed dispersion management systems are applied to obtain the best performance, as demonstrated in Fig. 5.2. DCF's are placed in the transmitter, the receiver, and the line amplifiers. A_T and Tx' are the amplifier and other components of transmitter, including CW lasers, modulators, and multiplexer; A_R and Rx' are the amplifier and other components of receiver, including de-multiplexer, optical filters, and electrical receivers.

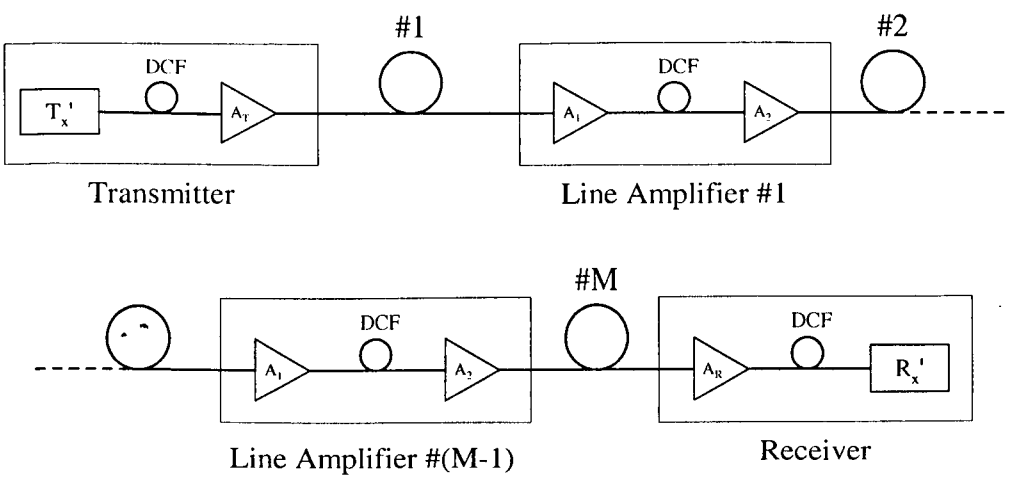

Figure 5.2: WDM transmission system using the combination of NZDF (D > 0) and DCF as dispersion management.

Currently, the dispersion parameter of DCF's used in commercial WDM transmission systems is around –80 ~ -150 ps/km/nm, the dispersion-loss ratio (so-called "DCF optimising factor") is about 200 ps/nm/dB. To reduce the OSNR decrease introduced by the DCF loss, the DCF in a line amplifier are normally placed between two optical amplifiers, as shown in Fig. 5.2. Thus, the ASE noise factor (*NF*) of the line amplifier can be described as: $NF = NF_1 + NF_2 /(G_1 \cdot ls)$, where NF_1 and NF_2 are the noise factors of the pre-DCF amplifier and post-DCF amplifier, respectively, G_1 is the optical gain of the pre-DCF amplifier, and $ls < 1$ is the loss of DCF.

As shown in Fig. 5.2, we investigate a dispersion-managed WDM transmission system contains *M* sections of transmission fibres, the length of each fibre span is *L*. The parameters of DCF's and transmission fibres are distinguished by the apostrophe. To simplify the problem, the length of DCF's in the line amplifiers are all set to L', in-line dispersion compensation ratio (DCR) is $\rho = |D'L'|/DL$; the length of DCF's in the optical receiver and transmitter are L'_R and L'_T, and the corresponding DCR are $\rho_{Rx} = |D'L'_R|/DL$ and $\rho_{Tx} = |D'L'_T|/DL$, respectively. Refer to the analytical models of SPM/XPM and their interplay with GVD introduced in chapter 2, it is not difficult to understand that the system performance is most sensitive to the variation of ρ_{Rx}, and its sensitivity to the variation of in-line DCR's decreases from the (*M*-1)th line amplifier to the 1st line amplifier.

In WDM transmission systems, due to the influence of fibre dispersion slope, the DCR's for different wavelength channels are different:

$$\frac{d\rho}{d\lambda} = -\frac{\rho}{|D'|}\left(\frac{|D'|}{D}\frac{dD}{d\lambda} + \frac{dD'}{d\lambda}\right). \tag{5.8}$$

In the following simulation experiments of this chapter, we suppose the WDM transmission system contains M = 6 spans of transmission fibre, the length of each span is L = 100 km, bit rate R_b = 10 Gb/s, fibre parameters are shown in table 5.1. The transmitter outputs are chirp-free NRZ signals, with rise time of 35 ps and extinction ratio of 17 dB. The optical filter used in the receiver is with bandwidth of 40 GHz, electrical filter is 4th order Bessel filter with 7.5 GHz 3dB bandwidth. Unless stated, the amplified WDM signal gets into CSMF or NZDF fibre has average power of $\overline{P}$ = 6 dBm for each channel, and $\overline{P}'$ = 0 dBm for WDM signal gets into DCF.

Table 5.1: Optical fibre parameters used in simulation (at 1550 nm wavelength)

FIBRE	α (dB/km)	**D** (ps/km/nm)	$dD/d\lambda$ (ps/km/nm^2)	γ (1/W/km)
NZDF	0.25	3.5	0.1	1.4
CSMF	0.25	17	0.06	1.2
DCF	0.5	-100	-0.2	5.0

5.3 Influence of XPM

From the analytical model of XPM effect introduced in section 2.4, ignore the XPM induced by DCF's and erbium-doped fibres in the EDFA's, and assume the EDFA's compensate fibre loss ideally, the relative amplitude interference to the CW wave

located at wavelength λ_j, from XPM effect caused by wave located at λ_k, can be described in frequency domain as:

$$\hat{I}_{kj}(f) = 4\gamma \cdot \hat{P}_k(f) \cdot \sum_{n=1}^{M} X_{kj,n} \exp(ifw_{kj,n}) \tag{5.9}$$

$$X_{kj,n} = \int_0^L e^{-(\alpha - ifd_{kj})z} \sin[-\frac{1}{2} f^2 (B_{j,n} - \beta_{2j} z)] dz \tag{5.10}$$

$$B_{j,n} = \beta_{2j} L \cdot [(1-\rho_j)(M-n) + (1-\rho_{\mathrm{Rx},j})] \tag{5.11}$$

$$w_{kj,n} = (n-1)(d_{kj}L + d'_{kj}L') \approx (n-1)(d_{kj}L)(1-\rho_j) \tag{5.12}$$

as $e^{-\alpha L} << 1$,

$$X_{kj,n} = \frac{\frac{1}{2} f^2 \beta_{2j} \cos(\frac{1}{2} f^2 B_{j,n}) - (\alpha - ifd_{kj}) \sin(\frac{1}{2} f^2 B_{j,n})}{(\alpha - ifd_{kj})^2 + (\frac{1}{2} f^2 \beta_{2j})^2} \tag{5.13}$$

where $B_{j,n}$ is the accumulative GVD from the n-th transmission fibre to the photo-detector at the wavelength of λ_j. As the channel frequency space is by far larger than the bit rate, in the frequency range of $0 < f/2\pi < 2R_b$, we always have $\left|\alpha - ifd_{kj}\right|^2 >> \left(\frac{1}{2} f^2 \beta_{2j}\right)^2$. If $\rho_j = 1$, for $n = 1, \cdots M$ we have $B_{j,n} = B_{j,M} = \beta_{2j} L \cdot (1-\rho_{\mathrm{Rx},j})$ and $w_{kj,n} = 0$, then

$$\hat{I}_{kj}(f) = 4\gamma \cdot \hat{P}_k(f) \cdot M \cdot X_{kj,M} \tag{5.14}$$

Let $\hat{I}_k(f) = \hat{P}_k(f)/\overline{P}_k$, and set $\overline{P}_k = 6\,\text{dBm}$, the amplitude transfer function of XPM-induced amplitude modulation, $\left|\hat{I}_{kj}(f)/\hat{I}_k(f)\right|$, can be plotted as Fig. 5.3 and Fig. 5.4, with NZDF and CSMF as the transmission fibre respectively. If $\rho_j = \rho_{\text{Rx},j} = 1$, the XPM-induced amplitude modulation can be hugely reduced, but can not be completely removed. While $\rho_j = 1$, the XPM accumulates along the transmission; if $\rho_{\text{Rx},j} \neq 1$, the interaction between XPM and the remaining dispersion will bring in remarkable amplitude modulation. Thus, while $\rho_{\text{Rx},j} \neq 1$, ρ_j should deviate from 1 to reduce the influence of XPM.

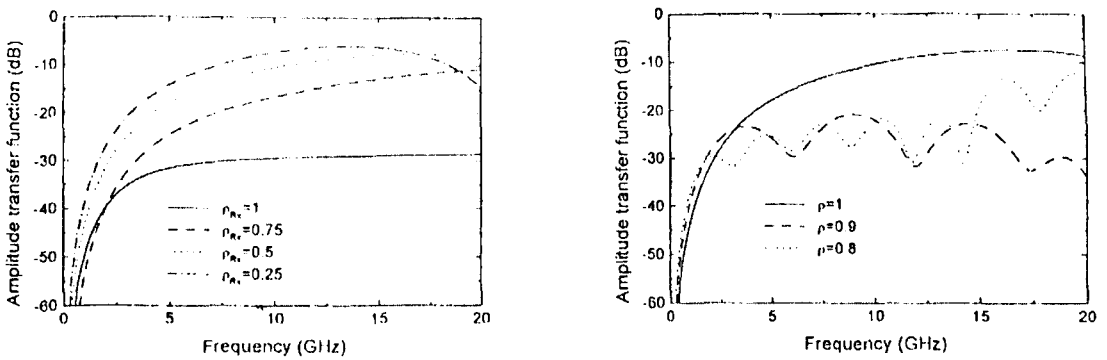

(a) (b)

Figure 5.3: Amplitude transfer function of XPM-induced amplitude modulation, in WDM transmission system with dispersion management. System contains 6 spans of 100 km NZDF, with $D_j = 3.5\,\text{ps/km/nm}$, $\Delta\lambda_{kj} = 0.8\,\text{nm}$. (a) in-line dispersion compensation ratio $\rho = 1$; (b) receiver dispersion compensation ratio $\rho_{\text{Rx}} = 0.5$.

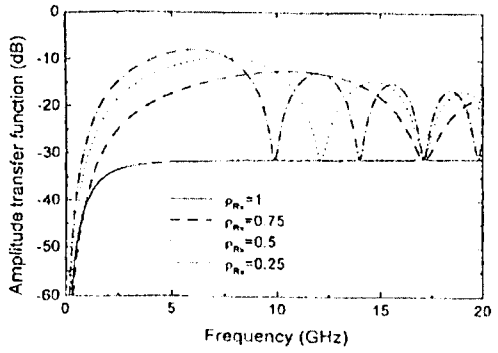

(a)

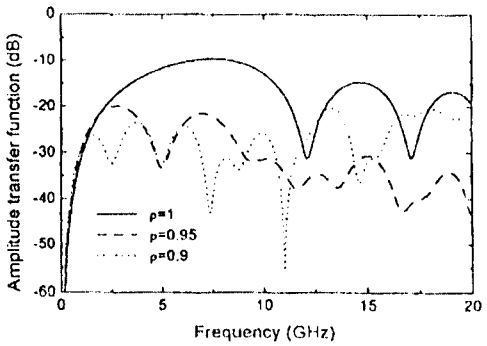

(b)

Figure 5.4: Amplitude transfer function of XPM-induced amplitude modulation, in WDM transmission system with dispersion management. System contains 6 spans of 100 km CSMF, with $D_j = 17\,\text{ps/km/nm}$, $\Delta\lambda_{kj} = 0.4\,\text{nm}$. (a) in-line dispersion compensation ratio $\rho = 1$; (b) receiver dispersion compensation ratio $\rho_{\text{Rx}} = 0.5$.

5.4 Noise amplification induced by Modulation Instability (MI)

From the pulse propagation model introduced in Chapter 2, if the accumulation of SPM and GVD from the n-th optical in-line amplifier to the photo-detector is negative, the Modulation Instability (MI) will amplify the ASE-signal beat noise. For optical fibre transmission system with positive dispersion (negative GVD), the MI-induced noise amplification becomes remarkable while the system is in-sufficiently compensated. The noise amplification factor can be described as [8]:

$$\kappa = \sqrt{\frac{\sigma_{RIN}^2}{B_e/(SNR_0 B_0)}} \tag{5.15}$$

where σ_{RIN}^2 is the square deviation of the relative intensity noise. Ignore the phase noise of the CW source, we can plot the contour of κ versus ρ and ρ_{Rx} with ρ_{Tx} set to be 0.5, as shown in Fig. 5.5. It reflects the influence of MI to the signal-ASE beat noise. In the simulations the gain of the in-line amplifiers and the pre-amplifier are all set to be 25 dB, the noise factors of all amplifiers are set to be 6 dB. If the phase noise of CW source is taken into consideration, the contour can be re-plotted as Fig. 5.6. Compare with Fig. 5.5, we find out that the influence of phase noise is unconspicuous.

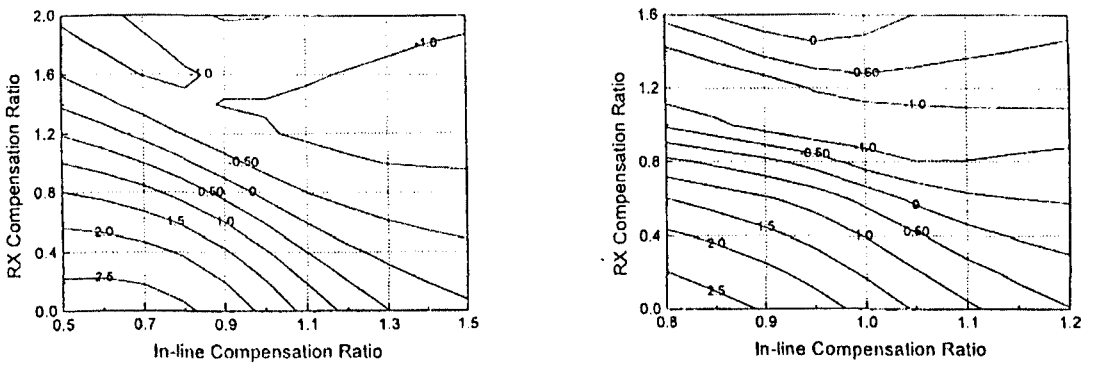

(a) (b)

Figure 5.5: Contour of noise amplification factor κ (dB) versus ρ and ρ_{Rx}, with phase noise of CW source ignored. (a) NZDF + DCF, $D = 3.5$ ps/km/nm; (b) CSMF + DCF, $D = 17$ ps/km/nm.

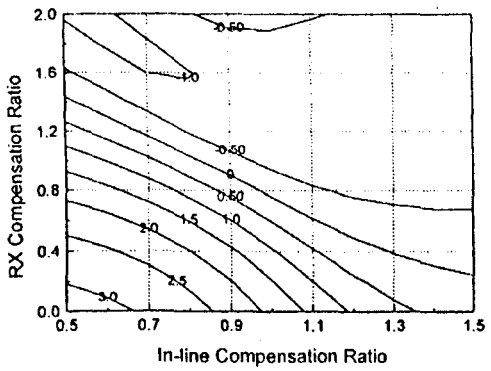

(a)

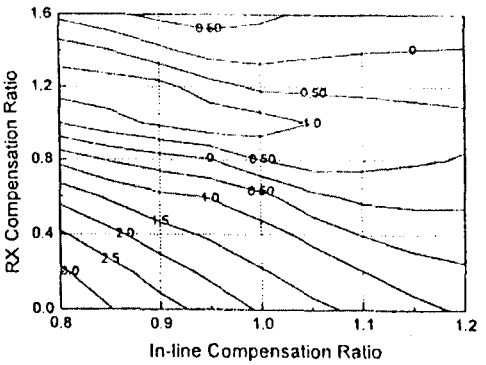

(b)

Figure 5.6: Contour of noise amplification factor κ (dB) versus ρ and ρ_{Rx}, with 10Mhz of CW source line-width. (a) NZDF + DCF, $D = 3.5\,\mathrm{ps/km/nm}$; (b) CSMF + DCF, $D = 17\,\mathrm{ps/km/nm}$.

5.5 Influence of SPM

In a dispersion management system, the accumulation of SPM and GVD, F_{SPM}, can be described as [8]:

$$(F_{\mathrm{SPM}} / 16.6T_b^{-2}) = [\frac{(M-1)(M-2)}{2}(1-\rho) + (M-1)(1-\rho_{\mathrm{Rx}})]\cdot\Phi_0 + (M-1)\cdot\Phi_1 + \Phi_2 \qquad (5.16)$$

$$\Phi_0 = \beta_2 L(\gamma\overline{P}L_{\mathrm{eff}} + \gamma\overline{P}'L'_{\mathrm{eff}})$$

$$\Phi_1 = \gamma\overline{P}\beta_2(L - L_{\mathrm{eff}})/\alpha + \gamma\overline{P}'\beta'_2(L' - L'_{\mathrm{eff}})/\alpha - (\gamma\overline{P}L_{\mathrm{eff}}\beta_2 L)\rho$$

$$\Phi_2 = \gamma\overline{P}\beta_2(L - L_{\mathrm{eff}})/\alpha + \gamma\overline{P}'\beta'_2(L'_{\mathrm{Rx}} - L'_{\mathrm{Rx,eff}})$$

Fig. 5.7 gives the contour of Eye-diagram Open Penalty (EOP) versus ρ and ρ_{Rx} with only dispersion and SPM taken into consideration, and ρ_{Tx} is set to be 0.5. The dotted line corresponds to $F_{SPM} = 0$. It shows that, appropriate in-sufficient compensation results in $F_{SPM} < 0$, thus reduces or even eliminates the interference caused by pulse broadening.

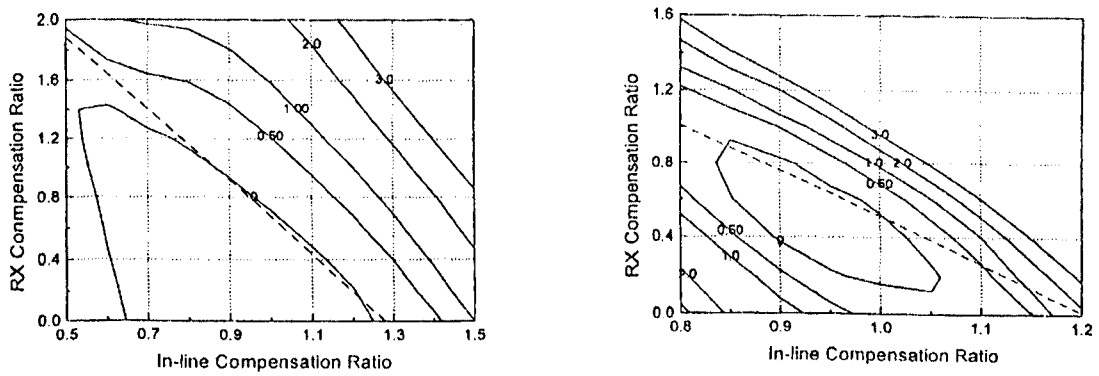

(a) (b)

Figure 5.7: Contour of EOP (dB) versus ρ and ρ_{Rx}, in the case of single channel transmission with noise ignored. (a) NZDF + DCF, $D = 3.5$ ps/km/nm; (b) CSMF + DCF, $D = 17$ ps/km/nm.

5.6 Dispersion management: 16 x 10 Gb/s transmission system

Let us suppose a 16x10 Gb/s WDM transmission system located at 193.8 ~ 192.3 THz (1546.9 ~ 1559.0 nm), the channel space is 100 GHz. Fig. 5.8 shows the contour of maximum Q-factor penalty of all channels versus ρ and ρ_{Rx} with ρ_{Tx} set to be 0.5, the dispersion management scheme is NZDF + DCF. Fig. 5.9 is the simulation result

of CSMF + DCF system. We can see from the figures that, with dispersion management, the Q-factor penalty of optimized NZDF + DCF system is 2 dB, which of optimized CSMF + DCF system is 1 dB. There are 2 reasons for which NZDF + DCF system can realize smaller Q-factor penalty: first, the large dispersion of CSMF increases the dispersing of channels, which benefits restraining the effect of XPM, while XPM has serious influence on NZDF system; second, CSMF + DCF system has much better dispersion slope compensation than NZDF + DCF system. It is very difficult to realize optimum dispersion management for different wavelengths simultaneously with the existence of dispersion slope, so it has very serious influence on WDM transmission. At the same time, CSMF + DCF system has its disadvantage: it applies much more DCF than NZDF + DCF system, which worsens the noise factor of line amplifier.

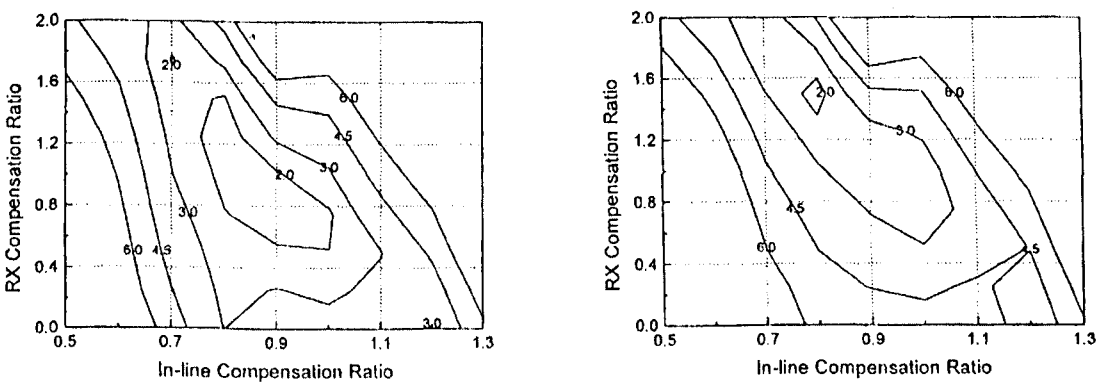

(a) (b)

Figure 5.8: Contour of maximum Q-factor penalty of all channels versus ρ and ρ_{Rx} with ρ_{Tx} set to be 0.5, for a 16x10Gb/s NZDF + DCF transmission with 100GHz channel spacing. (a) ignore, (b) consider noise amplification factor κ.

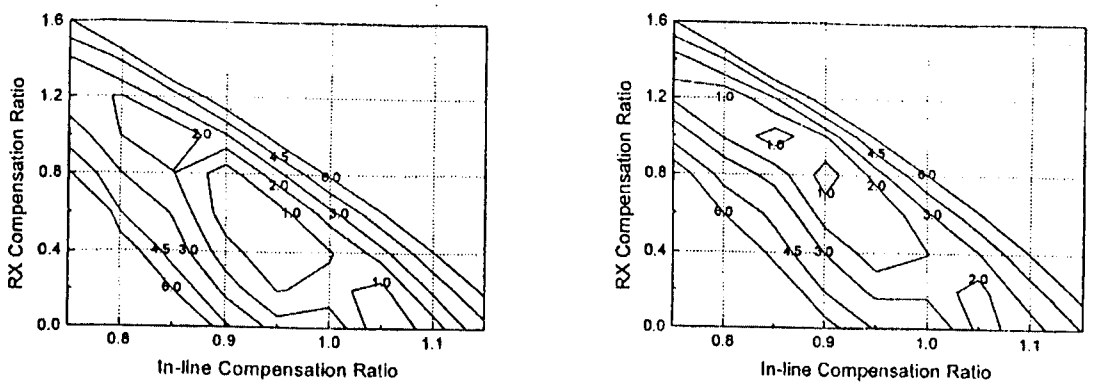

(a) (b)

Figure 5.9: Contour of maximum Q-factor penalty of all channels versus ρ and ρ_{Rx} with ρ_{Tx} set to be 0.5, for a 16x10Gb/s CSMF + DCF transmission with 100GHz channel spacing. (a) ignore, (b) consider noise amplification factor κ.

5.7 Summary

In this chapter, the GVD-induced influences on an optical fibre transmission system are investigated, these influences can be remarkably restrained by applying proper dispersion management scheme.

For C-band WDM transmission, four dispersion management schemes are presented. Comparing the advantages and disadvantages of different schemes, the author regards NZDF (D > 0) + DCF as generally the best fibre-combination scheme for dispersion management in WDM transmission systems.

The influence of XPM effect on WDM transmission systems applying dispersion management is investigated. If $\rho_j = \rho_{Rx,j} = 1$, the XPM-induced amplitude

modulation can be hugely reduced, but can not be completely removed. While $\rho_{\mathrm{Rx},j} \neq 1$, ρ_j should deviate from 1 to reduce the influence of XPM.

The noise amplification in a dispersion-managed WDM transmission system induced by modulation instability (MI) is investigated. For optical fibre transmission system with positive dispersion (negative GVD), the MI-induced noise amplification becomes remarkable while the system is in-sufficiently compensated.

The influence of SPM effect on WDM transmission systems applying dispersion management is investigated. Appropriate in-sufficient compensation reduces or even eliminates the interference caused by pulse broadening.

Dispersion management schemes are implemented in a 16x10Gb/s WDM transmission system. Simulation results show that the CSMF + DCF fibre-combination scheme has better performance in this case.

Chapter 6

WDM Channel Monitoring Through Blind Signal Separation

For the proper management of WDM transmission systems and particularly optical networks that use OADM and OXC, it is essential to monitor a variety of channel performance parameters such as SNR, BER, Q-factor, etc., without compromising transparency. Traditional methods for WDM channel monitoring use tunable optical filters, phased array demultiplexers, or photo-diode arrays with diffraction gratings [1]. The disadvantage of these methods is that complex (expensive) optical components are involved.

In a bid to reduce the number of expensive optical components, cost-effective monitoring solutions aim to perform most of the processing electronically. The (spatial) independence between the transmitted WDM channels has been exploited in recent works [2, 3, 4].

In this chapter, an effective technique to monitor the quality of WDM channels is presented. This process uses a blind signal separation (BSS) method based on higher-order-statistics (HOS), and an optical-loop structure, to extract the baseband channels from the WDM transmission. From the reconstructed baseband waveforms, a series of WDM transmission quality parameters can be evaluated. The HOS-based BSS procedure provides an approximate optimal solution (in the maximum-likelihood sense) for the case of two channels, and entails a computational cost of $O(N^{5/2})L$ when processing L-sample blocks of an N-channel WDM signal. Relative to previously proposed methods [5, 6, 7], the optical-loop structure presented in this chapter has further cost-effective features, especially when WDM signals are composed of a large number of channels.

6.1 Blind signal separation (BSS)

Blind signal separation (BSS) is the process of recovering independent signals that correspond to the individual source signals using only observed linear mixture of these. The term 'blind' emphasized the fact that no a priori assumptions on the structure of the mixing matrix and the source signals are made, in contrast to ordinary array processing techniques. Approaches to the BSS are based on the hypothesis that the source signals are statistically independent.

6.1.1 Modeling of BSS problems

Consider the set of q source signals $\{x_i(k), i = 1,2,..., q\}$ which generate the set of p observations or measurements $\{y_i(k), i = 1,2,..., p\}$ at the sensor output, where k represents a time index. In the general case, the measurements can be regarded as mixtures of transformed versions of the sources, contaminated by some additive noise $\{n_i(k), i = 1,2,..., p\}$:

$$y_i(k) = \sum_{j=1}^{q} H_{ij}\{x_j(k)\} + n_i(k), \qquad i = 1,2,..., p, \tag{6.1}$$

where $H_{ij}\{\cdot\}$ denotes the transformation undergone by j-th source contributing to the i-th sensor signal. In the linear case, $H_{ij}\{\cdot\}$ is a linear time-invariant (LTI) system operating over $x_j(k)$, $H_{ij}\{x_j(k)\} = h_{ij}(k) * x_j(k)$, symbol $*$ denoting the convolution operator. Then, the i-th measurement becomes:

$$y_i(k) = \sum_{j=1}^{q} h_{ij}(k) * x_j(k) + n_i(k), \qquad i = 1,2,..., p. \tag{6.2}$$

This is called the convolutive mixture BSS model [8, 9, 10, 11], can also be written in Matrix form as:

$$\begin{bmatrix} y_1(k) \\ \vdots \\ y_p(k) \end{bmatrix} = \begin{bmatrix} h_{11}(k) & \cdots & h_{1q}(k) \\ \vdots & \ddots & \vdots \\ h_{p1}(k) & \cdots & h_{pq}(k) \end{bmatrix} * \begin{bmatrix} x_1(k) \\ \vdots \\ x_q(k) \end{bmatrix} + \begin{bmatrix} n_1(k) \\ \vdots \\ n_p(k) \end{bmatrix} \quad \Rightarrow$$

$$\mathbf{y}(k) = \mathbf{H}(k) * \mathbf{x}(k) + \mathbf{n}(k), \tag{6.3}$$

where the column vectors $\mathbf{y} = [y_1, \ldots, y_p]^T$, $\mathbf{x} = [x_1, \ldots, x_q]^T$ and $\mathbf{n} = [n_1, \ldots, n_p]^T$ contain the observations, the sources and the noise signals, respectively, with symbol ^{T} denotes the transpose operation. Matrix **H** represents the multi-input multi-output linear system which links sources with measurements. The matrix notation stresses the multi-channel nature of the problem. Figure 6.1 graphically explains the BSS model for convolutive mixtures, in the simplified case of two sources and two measurements.

In many applications this model can be further simplified by assuming that the linear filters h_{ij} are composed of a single coefficient: $h_{ij}(k) = m_{ij}\delta(k)$. This occurs, for instance, in narrowband propagation conditions, where the propagation delays from source to sensors can be reduced to phase delays. As a result, the propagation effects are reduced to a change in amplitude, $|m_{ij}|$, and a phase term, $e^{j\angle m_{ij}}$. Under these circumstances, equation (6.2) becomes:

$$y_i(k) = \sum_{j=1}^{q} m_{ij} x_j(k) + n_i(k), \quad i = 1,2,\ldots, p, \tag{6.4}$$

or, in matrix form:

$$\begin{bmatrix} y_1(k) \\ \vdots \\ y_p(k) \end{bmatrix} = \begin{bmatrix} m_{11} & \cdots & m_{1q} \\ \vdots & \ddots & \vdots \\ m_{p1} & \cdots & m_{pq} \end{bmatrix} \begin{bmatrix} x_1(k) \\ \vdots \\ x_q(k) \end{bmatrix} + \begin{bmatrix} n_1(k) \\ \vdots \\ n_p(k) \end{bmatrix} \quad \Rightarrow$$

$$\mathbf{y}(k) = \mathbf{M}\mathbf{x}(k) + \mathbf{n}(k). \tag{6.5}$$

This is the instantaneous linear mixture BSS model. Now matrix **M** contains the coefficients of the linear transformation which represents the transfer from sources to observations. This matrix is denoted as mixing, transfer or channel-parameter matrix [12-14].

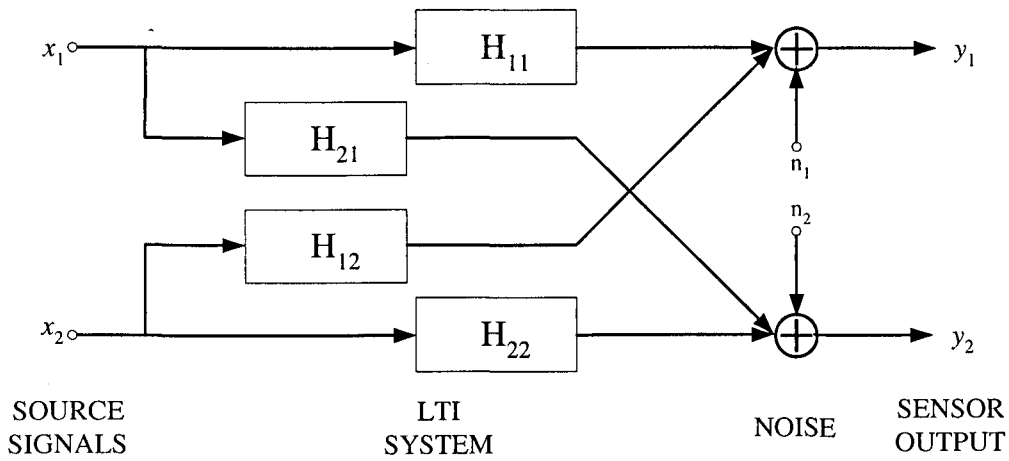

Figure 6.1: Convolutive signal separation model for the two-source two-sensor case.

The instantaneous linear model also applies when convolutive mixtures are considered, but in a different domain [15, 16]. Effectively, Fourier transforming both sides of equation (6.3) yields in the frequency domain:

$$\mathbf{Y}(\omega) = \mathbf{H}(\omega)\mathbf{X}(\omega) + \mathbf{N}(\omega), \tag{6.6}$$

where $\mathbf{Y}(\omega) = FT\{\mathbf{y}(k)\}, \mathbf{H}(\omega) = FT\{H(k)\}, \mathbf{X}(\omega) = FT\{\mathbf{x}(k)\}$ and $\mathbf{N}(\omega) = FT\{\mathbf{n}(k)\}$ are the Fourier transforms of the measurement vector, the multi-channel system, the

source vector and the noise vector, respectively. Therefore, both models (6.3) and (6.5) are somewhat equivalent when contemplated from different domains. However, the coefficients of the corresponding transfer matrix in (6.6) are not necessarily constant as in (6.5), but they may well vary with ω.

In both models, the goal of BSS can be stated as follows: to extract or recover the unknown original source signals, **x**, and possibly the unknown coefficients of the linear transformation that form the mixing matrix **M** from the only knowledge of the measured signals at the sensor output, **y**. The first objective (so-called blind signal estimation [14]) involves, explicitly or implicitly the estimation of the transfer matrix (so-called blind channel identification [14]), so both goals are inextricably interwined. Figure 6.2 graphically illustrated the basic BSS set-up.

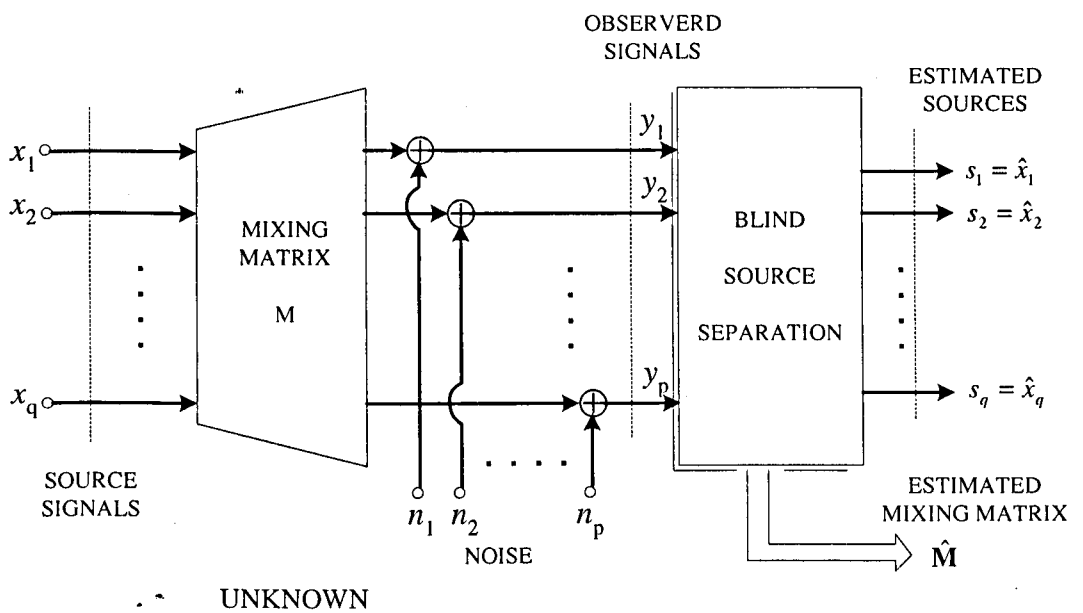

Figure 6.2: General Blind source separation set-up

6.1.2 Assumptions

To solve a problem with a model like (6.5), further assumptions must be made about the characteristics of the system. These hypotheses can be divided into three categories, depending on whether they refer to the mixing matrix, the sources or the noise signals. The standard hypotheses are the following:

A1. The mixing matrix **M** is full column rank, with $p \geq q$.

A2. Each component of $\mathbf{x}(k)$, $x_i(k)$, is a stationary zero-mean stochastic process, $i = 1,2,\ldots q$.

A3. At each time instant k, the components of $\mathbf{x}(k)$ are mutually statistically independent.

A4. The components of $\mathbf{x}(k)$ are unit-power.

A5. Each component of $\mathbf{n}(k)$, $n_i(k)$, is a stationary zero-mean process, $i = 1,2,\ldots p$.

A6. At each time instant k, the components of $\mathbf{n}(k)$ are mutually independent, as well as independent of the sources.

Assumption A1 states that the number of sensors must be at least equal to the number of sources. In general, one can recover, at most, as many sources as sensors. However, under certain conditions which hold in very specific problems, the extraction of more sources than sensors is indeed feasible [17, 18]. Similarly, the source stationarity of assumption A2 can sometimes be relaxed, or the lack of it can be tackled by a suitable adaptive implementation.

Assumption A3 is the crux of the blind separation. Statistical independence is equivalent to the factorization of the source joint probability density function (jPDF) in the product of the marginal PDF's:

$$p_x(\mathbf{x}) = \prod_{i=1}^{q} p_{x_i}(x_i), \tag{6.7}$$

where $p_x(\mathbf{x})$ is the source jPDF, and $p_{x_i}(x_i)$ the PDF of the i-th source signal. The above necessary and sufficient independence condition can also be stated as a function of the cumulants, which is often more tractable as a separation criterion:

$$Cum[x_{i_1},\ldots,x_{i_r}] = 0, \quad \forall\ (i_1,\ldots,i_r) \text{ not all equal, } \forall r \in \mathbb{N}, \tag{6.8}$$

i.e., the source cross-cumulants are null [19, 20, 21]. Physical independence of the sources is a sufficient condition for their independence in the statistical sense. However, the above condition on the source cumulants is too strong and it is often enough to constrain independence up to order r, that is, that all sth-order cross cumulants be equal to zero, for $s \leq r$. Generally, it is chosen $r = 4$, as in [22-25] and many other references. Third-order cumulants have not been paid attention in the literature because many practical distributions are symmetric. For these, the cumulants of such order are zero, and hence the problem becomes ill conditioned [26].

Assumption A4 is only a normalization convention. Actually the power of the sources can be included in the columns of **M**, leaving the observations unaltered. This property lies in the multiplicative-group structure of the model, which makes left-multiplication of the sources by a matrix equivalent to right-multiplication of the

mixing matrix by the same linear transformation [23, 27]. Let P_i be the power of the i-th source, $1 \le i \le q$, if $\mathbf{x}$ has not unit-power signals, the equivalent set of sources

$$\tilde{\mathbf{x}} = R_x^{-\frac{1}{2}}\mathbf{x}, \qquad R_x^{-\frac{1}{2}} = diag\left(\frac{1}{\sqrt{P_1}},\ldots,\frac{1}{\sqrt{P_q}}\right) \tag{6.9}$$

is such that $R_{\tilde{x}} \overset{\Delta}{=} E\left[\tilde{\mathbf{x}}\tilde{\mathbf{x}}^{\mathrm{H}}\right] = I_q$, $q \times q$ identity matrix. Then the new equivalent mixing matrix is transformed according to:

$$M\mathbf{x} = M(R_x^{-\frac{1}{2}}\tilde{\mathbf{x}}) = (MR_x^{-\frac{1}{2}})\tilde{\mathbf{x}}, \tag{6.10}$$

so one can always think of the sources being unit-power by properly scaling the columns of the mixing matrix. Hence one can assume that

$$R_x = I_q \tag{6.11}$$

with no loss of generality.

6.1.3 General approach

The source recovery and mixing matrix identification can be accomplished up to some extent. The following technical difficulties concerning the determination of the sources must be noticed [12, 22]:

1. Scalar factors can be exchanged between each source and the corresponding column of **M** without modifying the observations at all. That is, even bearing in mind the restriction imposed by Assumption A4, the sign (in the real case) or phase (in the complex case) of each source signal remains unobservable.

2. The outputs of the separator cannot be ordered. As a matter of fact, the order of the sources is itself arbitrary, since arranging the sources and the columns of the mixing matrix accordingly leave the observations unchanged. As a conclusion, the source signals can at best be recovered up to a permutation.

However, these degrees of freedom in the sources that can be estimated at the output of any unmixing system do not actually represent a limitation in the separation process, because in most practical applications:

1. The information conveyed by the sources is contained in their waveforms, rather than in their magnitudes, and hence a finite scalar factor is admissible.

2. The order in which the signals are arranged is immaterial. An order change in the recovered sources relative to the original set is thus acceptable.

Therefore, it is acceptable to obtain at the output of the separator a solution close to:

$$\hat{\mathbf{x}} = \mathbf{s} = PD\mathbf{x}, \tag{6.12}$$

where P is a $q \times q$ permutation matrix and D a non-singular diagonal matrix of the same size. The latter matrix represent the source re-arrangement commented in the first point above, whereas the former is a mathematical representation of the scaling factors referred to in the second place. The set of solutions $(MD^{-1}P^{-1}, PD\mathbf{x})$ form an equivalence class, so-called waveform-preserving (WP) equivalence [12-14].

Hence, solutions (M, x) and $(MD^{-1}P^{-1}, PD\mathbf{x})$ are said to be equivalent in the WP sense. Any recovered source vector of the form PDx is called a signal copy of the sources [28, 29].

The extraction of the sources is usually carried out by estimating a linear transformation W such that

$$\mathbf{s} = W\mathbf{y} \tag{6.13}$$

is WP equivalent to the original set of sources **x**, i.e., is a signal copy of the original sources. A matrix W fulfilling this condition is referred to as a (valid) separating matrix. The global system

$$G = WM \tag{6.14}$$

is the matrix which links the original set of sources with the estimated set, that is, the matrix that represents the whole mixing-unmixing system. Assumption A4 restricts D to have unit-norm diagonal elements.

Most BSS methods turn the sources independence assumption A3 into the separation criterion. A linear transformation W is sought so that the signals at the output of the

unmixing system, **s**, are independent. The independence assumption imposes certain conditions on the sources cross-cumulant, given by (6.8). thus, the cumulants become a natural quantitative measure of the degree of independence among the components of **s**. specifically, the elements of W must be such that the cross-cumulants of **s** vanish. The order up to which these cross-cumulants must be close to zero directly depends on the order of independence assumed for the sources.

A necessary and sufficient condition for the blind identifiability of the pair (M, **x**) is condensed by the following theorem:

Blind identifiability: *the source signals and the channel parameter matrix can be uniquely identified up to the waveform-preserving equivalence, if and only if at most one of the components of the source signals is Gaussian.*

An analogous result is found in [25]. This identifiability condition stems from the Gaussianity property of cumulants, which states that the cumulants of order higher than two of a random variable with Gaussian distribution are all null. This bounds the applicability of cumulants of such orders in the separation of Gaussian signals. The above identifiability condition could also be deduced from the fact that any linear combination of normal random variables is also normally distributed, and hence there is no way of separating such Gaussian signals in an additive model like (6.5). The above is a general condition for the identifiability of instantaneous linear mixtures. Actually, particular methods may have their own specific identifiability conditions, but all of them revolve around this general condition.

Two major groups of methods for BSS can be distinguished, depending on the statistical information employed – order of cumulants and degree of statistical information of the sources exploited. The first group is composed of second-order techniques, also known as Principal Component Analysis (PCA). PCA methods seek the removal of second-order dependence from the set of observations, thus providing a set of uncorrelated signals at the unmixing system output. The other main group of BSS methods is referred to as Independent Component Analysis (ICA). They aim to look for an output vector whose components are higher-order independent (the term 'higher' means more than second order). PCA procedures are simpler than ICA methods, but they are not always able to preserve the sources waveforms. The ICA overcomes this indeterminacy by resorting to the higher-order statistical information of the measurements. The use of this extra information makes the WP separation possible.

In many occasions, the BSS problem is tackled in two steps, the first one being a PCA and the second implementing ICA. This two-stage scheme presents some advantages relative to a single-step approach, as will be presented in the next section.

Most BSS methods mainly benefit from the spatial diversity of the problem, that is, the fact that distinct sensors output different (linearly independent) mixtures of the source signals, and generally any time structure is overlooked. In this connection, the BSS problem reduces to the identification of the source-vector probability distribution from the sample distribution of the observation vector [30]. In some cases, however, the time information can also be exploited, which may offer some advantages. For instance, if the source have different spectral content, the separation can be achieved

by means of the second-order statistics of the observation signals (such as correlation in different time lags). This allows Gaussian sources to be retrieved [12, 14, 31].

6.2 Two-stage strategy

It has been shown in the literature the convenience of facing the BSS problem through a two-step strategy [2, 22, 25, 32]. In the first step, the sensor outputs are decorrelated and normalized via conventional SOS-based technique, which corresponds to the PCA of the observations. Afterwards, in the noiseless environment, or if the noise spatial structure is known of fulfils certain conditions, only an orthogonal transformation remains to be unveiled to realize the separation. When the temporal information is disregarded, the second step necessarily involves BOS, yielding the ICA of the observations. This approach presents various advantages [25, 33]: a) since SOS are generally more accurately estimated than HOS, it seems sensible to exploit first all the information they contain, and b) a dimensionality reduction is achieved, since after the SOS step fewer (less than half) mixing-matrix parameters need to be identified, which, in addition, can be attained in a very efficient manner by means of Jacobi-like iteration procedures.

Direct single-step schemes have also been devised to tackle the problem [17, 34]. They are motivated by the main drawback of the two-stage method: the application of an initial second-order stage sets a limit on the performance of the whole separation system [35]. In addition, any existing noise affects the detection of the source signal subspace. If the noise is Gaussian, all their higher-order cumulant tensors vanish, so

that the inaccuracies introduced by the second-order step can be avoided by exploiting the HOS directly [34]. Nevertheless, the enhanced performance is usually achieved at the expense of an increase in computational complexity.

6.2.1 Second-order stage: PCA

The PCA is the standard statistical technique based on the decomposition of the covariance matrix of the observed variables [36, 37]. The original aim is to look for a few linear combinations of the observations that may be used to summarize the data, losing in the process as little information as possible. The selected transformation is such that it makes these linear combinations uncorrelated (i.e., independent at the second-order) and with decreasing variance. The resultant signals are regarded as an estimation of the true sources.

Let us assume that the mixing matrix has already been obtained. Then, the source signals may be estimated, for instance, via the maximum-likelihood (ML) principle by maximizing the likelihood of the observations with respect to the source vector. The log-likelihood is given by:

$$L(\mathbf{y};\mathbf{x}) = \log\big(p_y(\mathbf{y};\mathbf{x})\big) = \log\big(p_n(\mathbf{y} - M\mathbf{x})\big), \qquad (6.15)$$

where $p_y(\cdot)$ and $p_n(\cdot)$ denote the sensor-output and the noise PDFs respectively. If the noise is Gaussian, the maximizer of (6.15) is readily determined as [38]:

$$\hat{\mathbf{x}}_{ML} = (M^{\mathrm{T}} R_n^{-1} M)^{-1} M^{\mathrm{T}} R_n^{-1} \mathbf{y}, \qquad (6.16)$$

where $R_n \overset{\Delta}{=} E[\mathbf{n}\mathbf{n}^{\mathrm{H}}]$ denotes the noise covariance matrix. Note that the above expression even handle the case where the noise signals are spatially correlated, provided they are Gaussian and their covariance matrix is available. On the other hand, if it's known that the noise signals have the same variance, say σ_N^2, the ML estimator of the sources (6.16) reduces to:

$$\hat{\mathbf{x}}_{ML} = (M^{\mathrm{T}}M)^{-1}M^{\mathrm{T}}\mathbf{y}, \tag{6.17}$$

which corresponds to the well-known least-squares (LS) solution [38]:

$$\hat{\mathbf{x}}_{LS} = \arg\min_{\mathbf{x}} \|\mathbf{y} - M\mathbf{x}\|^2. \tag{6.18}$$

In the following, the singular value decomposition (SVD) [39, 40, 41] of the mixing matrix is used. It is given by:

$$M = U_M \Sigma_M V_M, \tag{6.19}$$

where $U_M \in C^{p\times p}$, $\Sigma_M \in C^{p\times p}$ and $V_M \in C^{p\times p}$ contain, respectively, the left singular vectors, the singular values and the right singular vectors of M. Matrices U_M and V_M^{H} fulfil the unitary condition: $U_M U_M^{\mathrm{H}} = U_M^{\mathrm{H}} U_M = V_M^{\mathrm{H}} V_M = I_p$.

PCA via EVD

In order to attain explicit PCA estimators of M and $\mathbf{x}$, consider the eigenvalue decomposition (EVD) of the sensor output covariance matrix, $R_y \overset{\Delta}{=} E[\mathbf{y}\mathbf{y}^{\mathrm{H}}]$:

$$R_y = \Gamma \Lambda \Gamma^{\mathrm{H}}, \tag{6.20}$$

in which matrix Γ contains the eigenvectors of R_y and diagonal matrix Λ contains its eigenvalues. From the BSS model (6.5), R_y can also be expanded as a function of the mixture elements:

$$R_y = MR_xM^{\mathrm{H}} + R_n = MM^{\mathrm{H}} + R_n = (U_M \Sigma_M)(U_M \Sigma_M)^{\mathrm{H}} + \sigma_N^2 I, \tag{6.21}$$

where assumption (6.11) is applied, as well as the orthogonality of the right singular matrix of M. Combining the previous two equations results in the estimate:

$$\hat{U}_M \Sigma_M = \Gamma(\Lambda - \sigma_N^2 I)^{\frac{1}{2}}, \tag{6.22}$$

where the rational power is taken element-wise. From (6.17), the estimated source vector is actually the set of uncorrelated observations, so-called whitened observations:

$$z = (\Lambda - \sigma_N^2 I)^{\frac{1}{2}} \Gamma^{\mathrm{H}} \mathbf{y}. \tag{6.23}$$

PCA via SVD

In a bid to avoid the explicit computation of the observation covariance matrix, advantage can be taken of the singular value decomposition (SVD) of the observation sample matrix. In a batch processing framework, T samples of the sensor signals are stored in the columns of a $p \times T$ matrix Y, so that $Y(:,k) = \mathbf{y}(k)$. Accordingly, the corresponding samples of the source and the noise signals would be contained in matrices X and N, respectively. The block-processing BSS model is the matrix equivalent of the vector model (6.5):

$$Y = MX + N . \tag{6.24}$$

The observation sample matrix Y can be expanded in its SVD:

$$Y = U\Sigma V^{\mathrm{H}} . \tag{6.25}$$

Then its covariance matrix accepts two different forms, one as a function of the mixing model (6.5), and the other from the previous SVD expansion:

$$R_y = MM^{\mathrm{H}} + R_n = (U_M \Sigma_M)(U_M \Sigma_M)^{\mathrm{H}} + \sigma_N^2 I \tag{6.26}$$

$$R_y \approx \frac{1}{T} YY^{\mathrm{H}} = \frac{1}{T} U\Sigma^2 U^{\mathrm{H}} . \tag{6.27}$$

Combine the above two equations, one can obtain the estimate:

$$\hat{U}_M \Sigma_M = \frac{1}{T} U (\Sigma^2 - T\sigma_N^2 I)^{\frac{1}{2}} . \tag{6.28}$$

If the noise is temporally (or spectrally) white (i.e., uncorrelated at different time instants), this expression can be submitted into (6.17), yielding the whitened signals:

$$Z = \sqrt{T}(\Sigma^2 - T\sigma_N^2 I)^{-\frac{1}{2}} U^{\mathrm{H}} Y = \sqrt{T}(\Sigma^2 - T\sigma_N^2 I)^{-\frac{1}{2}} \Sigma V^{\mathrm{H}} . \tag{6.29}$$

6.2.2 Higher-order stage: ICA

Second-order analysis leaves the right singular matrix of the mixing matrix undisclosed. This implies that the whitened sensor output and the true source vector are related through a unitary transformation $Q \in C^{p \times q}$:

$$\mathbf{z} = Q\mathbf{x} . \tag{6.30}$$

Remark that matrix Q above is not necessarily equal to the right singular matrix, V^{H}, of M. This can be justified as follows. Matrix $\hat{B}' = (\hat{U}_M \Sigma_M)'$ is said to whiten the observations, and is thus named whitening matrix. It fulfils:

$$R_z = R_{\hat{B}'y} = \hat{B}' R_y \hat{B}'^{\mathrm{H}} = (\hat{B}' U \Sigma)(\hat{B}' U \Sigma)^{\mathrm{H}} = I_q . \tag{6.31}$$

Hence, the estimated whitening matrix may be any of the form $\hat{B}' U \Sigma = \tilde{Q}$, with $\tilde{Q}$ an arbitrary unitary matrix. Therefore, $\mathbf{z} = \hat{B}' R_y = Q\mathbf{x}$, as in (6.30), with $Q = \tilde{Q} V^{\mathrm{H}}$.

An estimate of Q from the whitened observations is then sought so that it provides the source signal copy:

$$\hat{\mathbf{x}} = \mathbf{s} = \hat{Q}^{-1}\mathbf{z}\,. \tag{6.32}$$

In order to unveil this transformation, more constraints are needed. If the time information is used, such transformation may be estimated from the auto-correlation matrix of the whitened processes at lags different from zero. If, by contrast, the temporal information cannot be exploited or is just disregarded, the estimation of this matrix requires to take further advantage of the source statistical independence assumption. After a first estimation of the source via a second-order procedures, the matrix Q is sought by constraining higher-order independence at the outputs. This process involves, explicitly or implicitly, resorting to the higher-order statistical information (higher-order cumulants) of the signals. The extra processing, the ICA of the observations, supplies a set of higher-order independent signals. Under the general identifiability conditions summarized in Section 6.1.3, these output signals are WP equivalent to the wanted sources. In conclusion, the indeterminacy vanishes with the use of HOS techniques. Figure 6.3 sketches this two-step approach to BSS. Some of the most significant HOS-based approaches to BSS are surveyed in Section 6.3.

The two-signal real case

In the simplified real-mixture 2-source 2-sensor BSS case, unitary matrix Q in (6.30) becomes an elementary planar Givens rotation of the form:

$$Q = \tilde{Q}(\theta) \triangleq \begin{bmatrix} \cos\theta & -\sin\theta \\ \sin\theta & \cos\theta \end{bmatrix} \tag{6.33}$$

The problem, then, is reduced to determining angular parameter θ from the whitened observations. Once this has been achieved, a counter-rotation of this angle performed on the whitened observations provides the original source waveforms. For cases contain more than 2 sources, the process is of similar nature, and will be addressed in the next Section.

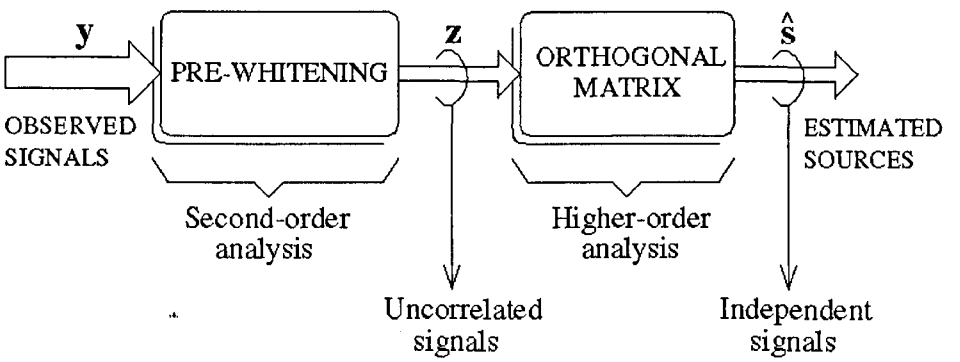

Figure 6.3: Two-stage approach to signal separation

6.3 Maximum likelihood approaches to BSS

With the help of the Gram-Charlier expansion of the sources jPDF, a sub-optimal two-step procedure is developed: first, decorrelation, second, 4th-order independence. Interestingly, the cost function to be maximized in the second step is identical to the contrast function derived separately by Comon in [25]. In [42], the ML principle leads

to estimating equations which depend on non-linear functions of the observations. The optimal nonlinearities are the derivatives of the logarithm of the source PDFs. The ML standpoint is also adopted in [32], where by using certain simplifications a close-form solution for the angle to be estimated in the noiseless two-source two-sensor BSS set-up. In [6] the ML principle is combined with the EM (Expectation-Maximization) algorithm to yield a method able to separate more sources than sensors in the case of discrete sources.

6.3.1 Approximate maximum-likelihood (AML) estimator

By definition, the ML estimator of θ is the value of the rotation angle that maximizes the (log-)likelihood of the given whitened observations, $\mathbf{z}(k)$. Mathematically, this idea can be expressed as:

$$\hat{\theta}_{\mathrm{ML}} = \arg\max_{\hat{\theta}} \log p_{\mathbf{z}}(\mathbf{z} \mid \hat{\theta}) \tag{6.34}$$

$p_{\mathbf{z}}(\cdot)$ denotes the PDF of the decorrelated measurement, which is related to the source PDF through:

$$p_{\mathbf{z}}(\mathbf{z} \mid \hat{\theta}) = p_{\mathbf{x}}(\hat{Q}^{-1}\mathbf{z}) = \prod_{i=1}^{q} p_{x_i}\left((\hat{Q}^{\mathrm{T}}\mathbf{z})_i\right), \tag{6.35}$$

$p_{x_i}(\cdot)$ being the marginal PDF of the i-th source. For T independent observations $\mathbf{z}(k)$, $k = 1, 2, \ldots, T$, the overall log-likelihood becomes the sum of each sample log-likelihood:

$$\log p_z(\mathbf{z} \mid \hat{\theta}) = \sum_{k=1}^{T} \log p_z(\mathbf{z}(k) \mid \hat{\theta}). \tag{6.36}$$

In [32], the source jPDF was approximated by its Gram-Charlier expansion [43, 44] truncated at the forth-order term. For symmetric sources, i.e., $\kappa_{30}^x = \kappa_{03}^x = 0$, the log-likelihood function reads:

$$\log p_z(\mathbf{z}(k) \mid \hat{\theta}) = -\frac{r_k^4}{2} + \frac{3}{4!}\left(\frac{r_k^4}{8} - r_k^2 + 1\right)(\kappa_{40}^x + \kappa_{04}^x)$$

$$+\frac{1}{4!2}(r_k^4 - 6r_k^2)\cos 2(\phi_k - \hat{\theta})(\kappa_{40}^x - \kappa_{04}^x) + \frac{r_k^4}{4!8}\cos 4(\phi_k - \hat{\theta})(\kappa_{40}^x + \kappa_{04}^x). \tag{6.37}$$

Assuming, additionally, that the source have the same distribution (at least up to the fourth-order in their Gram-Charlier expansion), the maximization of the likelihood function provided with the ML estimator of θ:

$$\hat{\theta}_{\mathrm{AML}} = \frac{1}{4}\operatorname{arctg}\frac{\sum_k r_k^4 \sin 4\phi_k}{\sum_k r_k^4 \cos 4\phi_k}. \tag{6.38}$$

The properties of the estimator were also studied in [32]. Under all the above assumptions, it was found to be unbiased for any sample size. In addition, the Cramer-Rao lower bound (CRLB) for the estimation of θ under the conditions of this particular ML development was deduced to be:

$$\mathrm{Var}[\hat{\theta}_{\mathrm{AML}}] \geq \frac{6}{T[(\kappa_{40}^x)^2 + (\kappa_{04}^x)^2]}, \tag{6.39}$$

where $\hat{\theta}$ is expressed in radians.

6.3.2 Extend maximum-likelihood (EML) estimator

Dropping the time index k for convenience, let us define the 4th-order complex statistic:

$$\xi \stackrel{\Delta}{=} \mathrm{E}[r^4 e^{j4\phi}] = \mathrm{E}[(z_1 + jz_2)^4]. \tag{6.40}$$

The above equation can be expanded as a function of the sources and the unknown rotation angle [45]:

$$\xi = e^{j4\theta}\,\mathrm{E}[r^4 e^{j4\phi'}] = e^{j4\theta}\,\mathrm{E}[(x_1 + jx_2)^4]. \tag{6.41}$$

From the expressions given in [46]:

$$\mathrm{E}[(x_1 + jx_2)^4] = \kappa_{40}^{x} + \kappa_{04}^{x}, \tag{6.42}$$

ξ may be expressed as a function of the source statistics:

$$\xi = e^{j4\theta}(\kappa_{40}^{x} + \kappa_{04}^{x}). \tag{6.43}$$

The term in brackets, the source kurtosis sum (sks), is not known, because by definition the sources are not known either. However, the statistic can be obtained from the whitened data as follows:

$$\gamma \overset{\Delta}{=} \kappa_{40}^{x} + \kappa_{04}^{x} \underset{\substack{\uparrow \\ from\ (8.42)}}{=} \mathrm{E}[(x_1 + jx_2)^4] = \mathrm{E}[(x_1^4 + x_2^4 - 6x_1^2x_2^2) + j4(x_1^3x_2 - x_1x_2^3)]$$

$$\underset{\substack{\uparrow \\ \kappa_{31}^{x}=\kappa_{13}^{x}=0}}{=} \mathrm{E}[x_1^4 + x_2^4 - 6x_1^2x_2^2] = \mathrm{E}[(x_1^2 + x_2^2)^2 - 8x_1^2x_2^2] \underset{\substack{\uparrow \\ E|x_1^2x_2^2|=1}}{=} \mathrm{E}[(x_1^2 + x_2^2)^2] - 8. \tag{6.44}$$

That is,

$$\gamma = \mathrm{E}[(x_1^2 + x_2^2)^2] - 8 = \mathrm{E}[r^4] - 8. \tag{6.45}$$

Hence, this parameter is also available as a function of the whitened data as:

$$\gamma = \mathrm{E}[(z_1^2 + z_2^2)^2] - 8, \tag{6.46}$$

From [45], $r^2 = x_1^2 + x_2^2 = z_1^2 + z_2^2$. Therefore,

$$\angle\xi_\gamma = 4\theta, \qquad \xi_\gamma \overset{\Delta}{=} \xi \cdot \mathrm{sign}(\gamma). \tag{6.47}$$

In practice, for single signal realizations composed of T samples, the ensemble or population averages in (6.40) and (6.45)-(6.46) are estimated by their unbiased time or sample average:

$$\hat{\xi} = \frac{1}{T}\sum_{k=1}^{T} r_k^4 e^{j4\phi_k} = \frac{1}{T}\sum_{k=1}^{T} (z_1(k) + jz_2(k))^4 , \tag{6.48}$$

$$\hat{\gamma} = \frac{1}{T}\sum_{k=1}^{T} r_k^4 - 8 = \frac{1}{T}\sum_{k=1}^{T} (z_1^2(k) + z_2^2(k))^2 - 8 , \tag{6.49}$$

so that ξ_γ can be estimated from the above two:

$$\hat{\xi}_\gamma = \hat{\xi} \cdot \text{sign}(\hat{\gamma}) . \tag{6.50}$$

As a result, the following angle estimator arises:

$$\hat{\theta}_{\text{EML}} = \frac{1}{4}\arg(\hat{\xi}_\gamma) , \tag{6.51}$$

in which function "$\arg(\hat{\xi}_\gamma)$" supplies the principal value of the argument of $\hat{\xi}_\gamma$ (i.e., its four-quadrant phase).

Notice that no assumptions on the source PDFs have been made at all to arrive at this expression, which makes this estimator valid for any source distribution combination with any kurtosis value and any type of symmetry, as long as the sks is not zero. In the case of such a sum being zero, the magnitude of ξ would also be null and θ could not be estimated from it any more.

6.4 WDM channel extraction using BSS

The technique presented in [47] is able to reconstruct the complete channel waveforms, from which performance parameters can be measured. Along the lines of [48] wavelength-dependent attenuators (WDAs) are employed to obtain additional observations of the WDM signal, each observation being considered as a mixture of the constituent channels. As the WDA has an adjustable nonlinear relation between the wavelength and the output power, the independent channels contribute with different strengths to each observation, and sufficient spatial diversity is available for a suitable BSS method to recover the original transmitted waveforms.

The symmetric adaptive decorrelation (SAD) technique of [49] was adopted as a separation device. This particular technique, however, presents a number of deficiencies. On the one hand, its complexity is of order $O(N!)$ for an N-channel WDM transmission. On the other hand, the method has inherent stability and convergence difficulties --- including spurious non-separating solutions [49] --- which may hinder the monitoring process in practical cases. More specifically, the method is based on second-order statistics, which causes identifiability problems in the separation of spectrally white sources. In [50, 51], each channel consumes a unique set of WDA and photodetector, which makes this technique less efficient with the increasing of the channel numbers.

In this Section, we overcome these shortcomings by a more cost-effective optical-loop structure to WDM monitoring, as well as applying HOS-based BSS.

Figure 6.4 shows a system setup of the proposed WDM channel monitoring scheme. A small fraction of the N channels WDM signal is coupled out of the network using an asymmetric power splitter. A predetermined period of time, let's say T_1, of this splitted optical signal is then cut out and sent into an optical loop, which contains a delay fibre and an optical pump, to generate a periodic optical signal sequence of repeating signal fraction T_1 for N times, each period of the signal is spaced to each other by a predetermined period of "all-zeros". An adjustable wavelength-dependent attenuator (WDA) [50] is used to attenuate this sequence. The WDA is synchronized with the optical switch, thus the attenuation factor for each period of signal fraction T_1 is adjusted to be different from each other. This synchronization is implemented by relating the driving voltage of the WDA to the optical switch, the required switching speed of the optical switch and WDA is related to T_1, thus the length of the delay fibre, and the length of the "all-zero" sequences used to space the "T_1" sequences. An optical pump is also applied to compensate the power coupled out of the optical loop. The attenuated optical signal sequence is converted into an electrical signal sequence by a photodetector. The purpose of the loop and WDA structure is to generate several linear mixtures of the WDM channels, which a BSS method can later be used to extract the WDM channels separately. From the reconstructed WDM waveforms, quality parameters such as eye diagrams, Q-factor, and BER can be estimated.

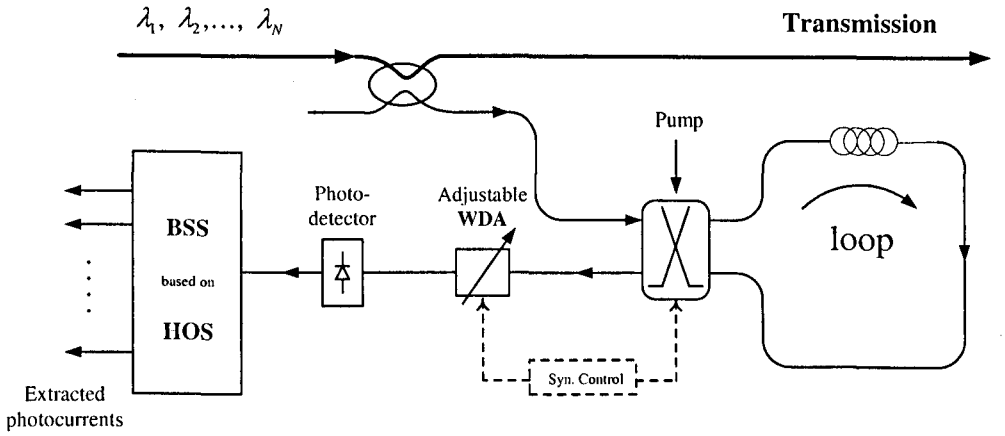

Figure 6.4: Experimental Setup

The wavelength-dependent attenuating procedure above is a form of nonlinear optical signal processing, which can compensate the lost of the wavelength information caused by the conversion from optical domain to electrical domain [48]. By applying appropriate electrical signal processing methods, upto some extent, we do not need to know the details of this nonlinear optical signal processing (i.e., the WDA).

Let $y_i(k)$, $1 \le i \le M$, denote the M observed photocurrents of the N-channel WDM signal ($M \ge N$), where k represents a discrete time index. Accordingly, let $s_i(k)$, $1 \le i \le N$, represent the channel (or source) baseband data, multiplexed within the WDM signal and thus not directly observable, can be assumed to be mutually statistically independent. Direct photodetection of the WDM transmission loses all wavelength information. As a result, neglecting additive noise terms, the detected signal appears as a weighted linear combination of the baseband data:

$$y_i(k) = \sum_{j=1}^{N} h_{ij} s_j(k), \quad 1 \le i \le M. \tag{6.52}$$

Coefficients h_{ij} represent the WDA effects over channel j in observed photocurrent i. Hence, the observation vector $\mathbf{y} = [y_1, ..., y_M]^T$ and the channel vector $\mathbf{s} = [s_1, ..., s_N]^T$ fulfil at any time instant the linear model:

$$\mathbf{y} = \mathbf{H}\mathbf{s}, \tag{6.53}$$

where the elements of the $(M \times N)$ mixing matrix $\mathbf{H}$ are given by $(\mathbf{H})_{ij} = h_{ij}$. Equation (6.53) corresponds to the BSS model of instantaneous linear mixtures. From Section 6.1.2, separation is generally achievable under two main assumptions: (A1) the source signals are mutually statistically independent and (A2) the mixing matrix is full column rank; both entities are otherwise unknown in model (6.53). Note that assumption A2 guarantees considerable freedom in the selection of the WDA attenuation patterns.

As in [48], we aim to perform the monitoring by first extracting the channel waveforms from the photocurrent observations, but here we resort to the BSS method of [52], which is based on higher-order-statistics (HOS). The method operates in two steps as shown in Figure 6.3. The first step is (spatial) pre-whitening, and seeks to normalize and decorrelate the observations by means of conventional second-order statistical analysis (PCA). This operation results in a signal vector $\mathbf{z}$ which is linked to the channel components through an unknown $(M \times N)$ orthogonal transformation $\mathbf{Q}$:

$$\mathbf{z} = \mathbf{Q}\mathbf{s}. \tag{6.54}$$

The second step finds an estimate $\hat{\mathbf{Q}}$ of $\mathbf{Q}$, from which the channel signals can be reconstructed as $\hat{\mathbf{s}} = \hat{\mathbf{Q}}^T \mathbf{z}$. In the two-signal case ($N = 2$), matrix $\mathbf{Q}$ becomes a givens rotation defined by a single real-valued parameter θ:

$$\mathbf{Q} = \begin{bmatrix} \cos\theta & -\sin\theta \\ \sin\theta & \cos\theta \end{bmatrix}. \tag{6.55}$$

The estimation of θ can be accomplished in closed form. Several analytic expressions exist, but the EML estimator of [52] presents the advantage that it approximates the maximum-likelihood solution when the source signals have the same statistics. This is the case in the WDM monitoring problem, where all transmitted channels are composed of bit streams, possibly contaminated by noise and interference. This estimator expression reads:

$$\hat{\theta} = \frac{1}{4} \angle(\xi \cdot \text{sign}(\gamma)), \tag{6.56}$$

with

$$\xi = (\kappa_{40}^{z} - 6\kappa_{22}^{z} + \kappa_{04}^{z}) + j4(\kappa_{31}^{z} - \kappa_{13}^{z}), \tag{6.57}$$

$$\gamma = \kappa_{40}^{z} + 2\kappa_{22}^{z} + \kappa_{04}^{z}, \tag{6.58}$$

where $\kappa_{mn}^{z\hat{}} = \text{Cum}_{mn}[z_1, z_2]$ represents the $(m+n)$th-order cumulant of the whitened components.

To achieve the source estimation for $N > 2$ channels, the closed-form expression is applied over each pair of whitened signals until convergence is reached. Since there exist $N(N-1)/2$ signal pairs and usually around $\left(1+\sqrt{N}\right)$ sweeps over the signal pairs are necessary for convergence, the method's complexity with respect to the number of channels is of order $O(N^{5/2})$. This value is lower than the $O(N!)$ of [53], especially for a large number of channels.

In addition, this HOS-based method ignores any temporal structure in the processed signals, so that spectrally white photocurrents could also be separated. If the data symbols transmitted by a single user are uncorrelated, such spectrally white photocurrents could arise when sampling the photodectector output at rates as low as the symbol rate. Our lower complexity but high performance method reduces the cost of the DSP needed for the WDM channel extraction and monitoring without sacrificing performance.

6.5 Implementation and simulation results

Illustrative experiments are carried out with the aid of the VPI™ simulation software, with the blind separation part implemented in MATLAB™ code.

First we demonstrate the technique in a four-channel WDM setup. Four data channels at wavelengths 1551.0, 1554.2, 1557.4 and 1560.6 nm (i.e., 3.2-nm separation), respectively, compose the WDM signal. The laser sources are modulated via Mach-

Zehnder modulators by NRZ data from a pseudorandom binary sequence at 10-Gb/s bit rate.

As explained in Section 6.4, a small fraction of the transmitted WDM signal is diverted from the optical link into the monitoring system through an asymmetric splitter, a fibre span of 50 km is included in front of the monitoring point. A block of this WDM signal fraction is then let into an optical loop. The signal block runs in the loop four circles, at the end of each circle the signal is coupled out of the optical loop. This means that the output of the optical loop are four blocks of repeated signals, each block is spaced to each other by 128 bit "all-zeros". These four signal blocks are sent to an optical signal processor, i.e., the adjustable WDA, sequentially. The adjustable WDA is synchronized with the optical loop, and is tuned to have different but unknown attenuation on each of the signal blocks. All these attenuated signal blocks are detected by a p-i-n photodetector, which generate the corresponding observed photocurrents shown in Fig. 6.5.

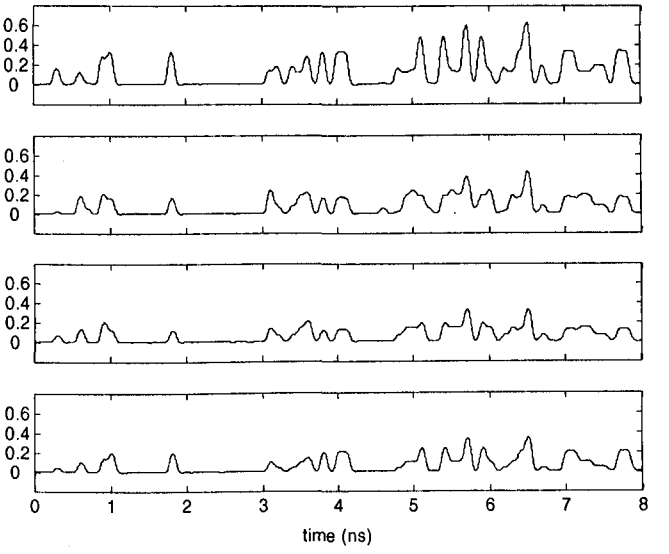

Figure 6.5: Observed photocurrents in the 4-channel experiment

These electronic signals are then collected and processed by the HOS-based BSS methods described in Section 6.4 to obtain the signal separation. The normalized (i.e., zero-mean, unit-power) channel data estimated by EML method are shown by the solid lines of Fig. 6.6. A block of 256 bits (32768 samples) was processed, of which only a short portion is displayed in the figure for the sake of clarity. Observe the accuracy with which the estimated sequences approximate the actual transmitted data (dotted lines).

Eye-diagrams for each channel can be plotted from the separated waveforms, shown in Fig. 6.7, thus the average Q-factors and bit error rates for each channel can be evaluated using the method introduced in section 3.3.

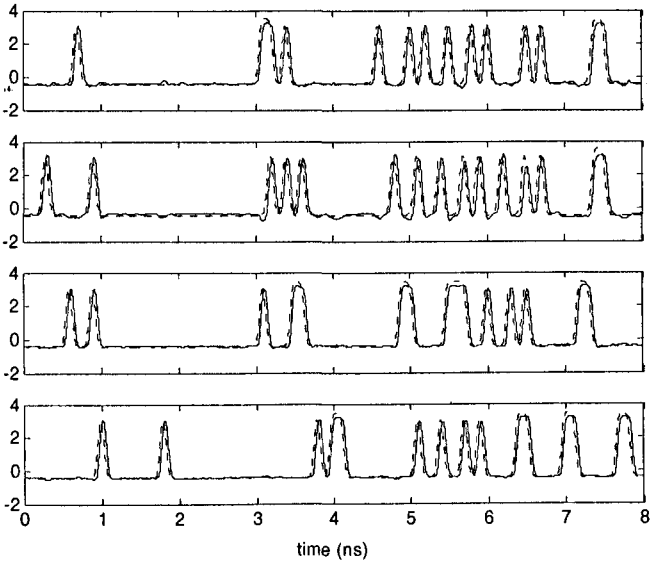

Figure 6.6: Normalized data sequences in the 4-channel experiment. Dotted lines: transmitted data. Solid lines: channel data estimated by the HOS-based BSS method (EML) from the photocurrents shown in Fig. 6.5.

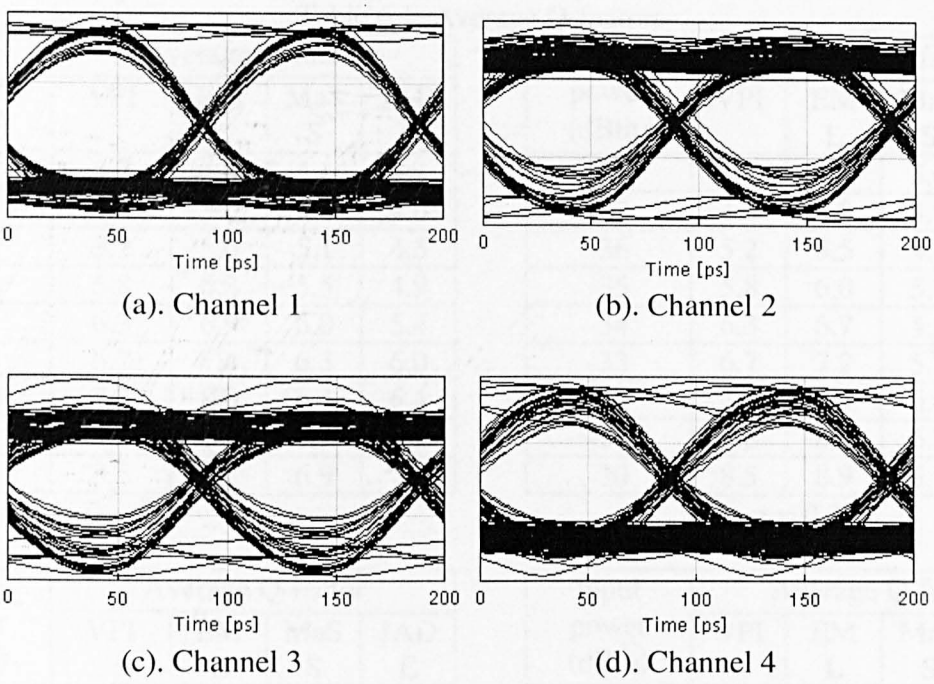

(a). Channel 1 (b). Channel 2

(c). Channel 3 (d). Channel 4

Figure 6.7: Eye-diagrams for the 4-channel experiment

Table 6.1 gives the average Q-factors of all 4 channels, with the channel waveforms extracted by EML, MaSSFOC and JADE method, respectively. The input power levels at the Mach-Zehnder modulators are tuned between –38 and –30 dBm, and the coefficient α in Eq. (13) is set to 0.1, 0.2, 0.3, 0.4, respectively. VPI software estimates BER through a Gaussian assumption [54], and the estimated average Q-factors are presented in the tables as well. Comparison of the results shows that, the EML method provides the best approach of Q_{avg} estimation to the industrial simulation software (VPI) with $\alpha = 0.3$. Figure 6.8 presents the average BER curves with the channel waveforms extracted by EML, MaSSFOC and JADE method, respectively, which shows that the EML method provides the best approach of BER estimation to the industrial simulation software (VPI), with the BER curves for each single channel shown in Fig. 6.9.

Table 6.1: Average Q-factors

Input power (dBm)	Average Q-factor			
	VPI	EML	MaSS	JADE
-38	3.7	4.3	4.1	3.4
-37	4.5	5.0	4.6	4.0
-36	5.2	5.6	5.1	4.5
-35	5.8	6.3	5.5	4.9
-34	6.3	6.9	6.0	5.4
-33	6.7	7.4	6.3	6.0
-32	7.3	8.0	6.4	6.4
-31	7.8	8.5	6.7	6.7
-30	8.5	9.2	6.9	7.1

(a). $\alpha = 0.1$

Input power (dBm)	Average Q-factor			
	VPI	EML	MaSS	JADE
-38	3.7	4.1	3.6	3.3
-37	4.5	4.8	4.1	4.0
-36	5.2	5.5	4.8	4.8
-35	5.8	6.0	5.2	5.2
-34	6.3	6.7	5.5	5.5
-33	6.7	7.2	5.7	5.8
-32	7.3	7.9	6.0	6.3
-31	7.8	8.5	6.2	6.7
-30	8.5	8.9	6.6	7.1

(b). $\alpha = 0.2$

Input power (dBm)	Average Q-factor			
	VPI	EML	MaSS	JADE
-38	3.7	3.9	3.4	3.1
-37	4.5	4.6	4.0	3.7
-36	5.2	5.3	4.5	4.2
-35	5.8	5.9	4.9	4.8
-34	6.3	6.3	5.2	5.2
-33	6.7	6.7	5.5	5.7
-32	7.3	7.2	5.8	6.3
-31	7.8	7.8	6.2	6.8
-30	8.5	8.6	6.6	7.5

(c). $\alpha = 0.3$

Input power (dBm)	Average Q-factor			
	VPI	EML	MaSS	JADE
-38	3.7	3.2	2.9	2.6
-37	4.5	3.8	3.4	3.1
-36	5.2	4.5	4.0	3.7
-35	5.8	5.1	4.4	4.2
-34	6.3	5.6	4.7	4.6
-33	6.7	6.0	5.0	5.1
-32	7.3	6.3	5.2	5.7
-31	7.8	6.9	5.3	6.1
-30	8.5	7.7	5.8	6.6

(d). $\alpha = 0.4$

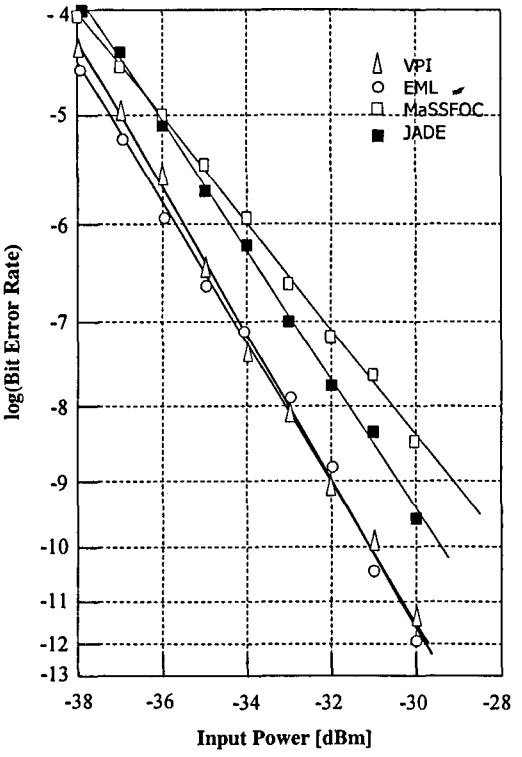

Figure 6.8: Comparison of average BER curves from different methods

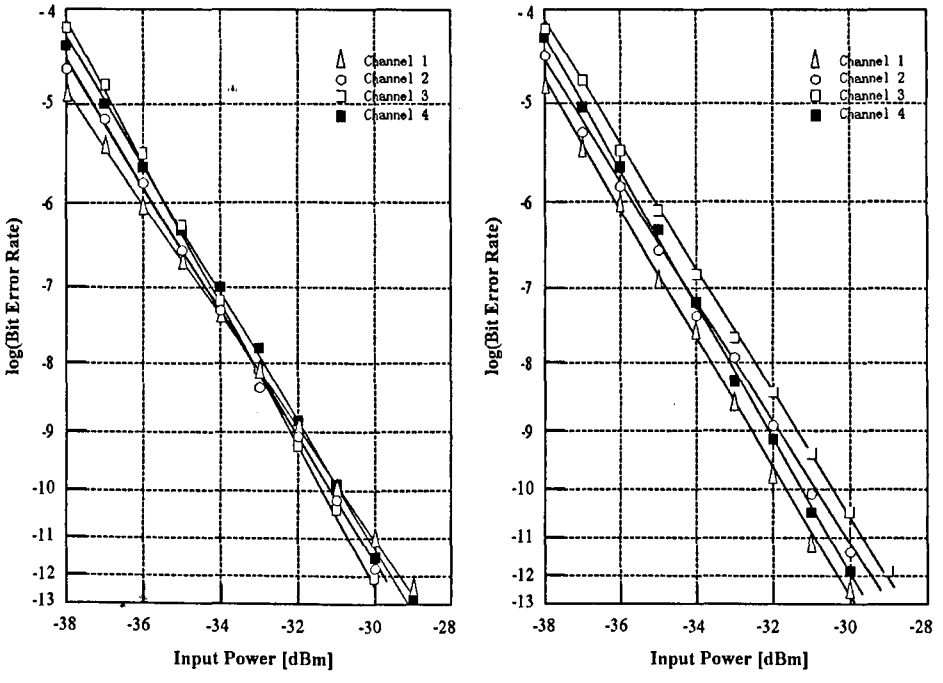

(a) (b)

Figure 6.9: BER vs. Input Power curves. (a) EML method with the optical loop structure; (b) Gaussian assumption by VPI.

The proposed method is also capable of monitoring a higher number of channels. Fig. 6.10 shows the observed photocurrents and separation results for an 8-channel WDM transmission with 1.6-nm channel spacing, under the general conditions for 4-channel experiment. The estimated BER curves for each channel are shown in Fig. 6.11(a), using EML method, compared with the results from VPI software shown in Fig. 6.11(b).

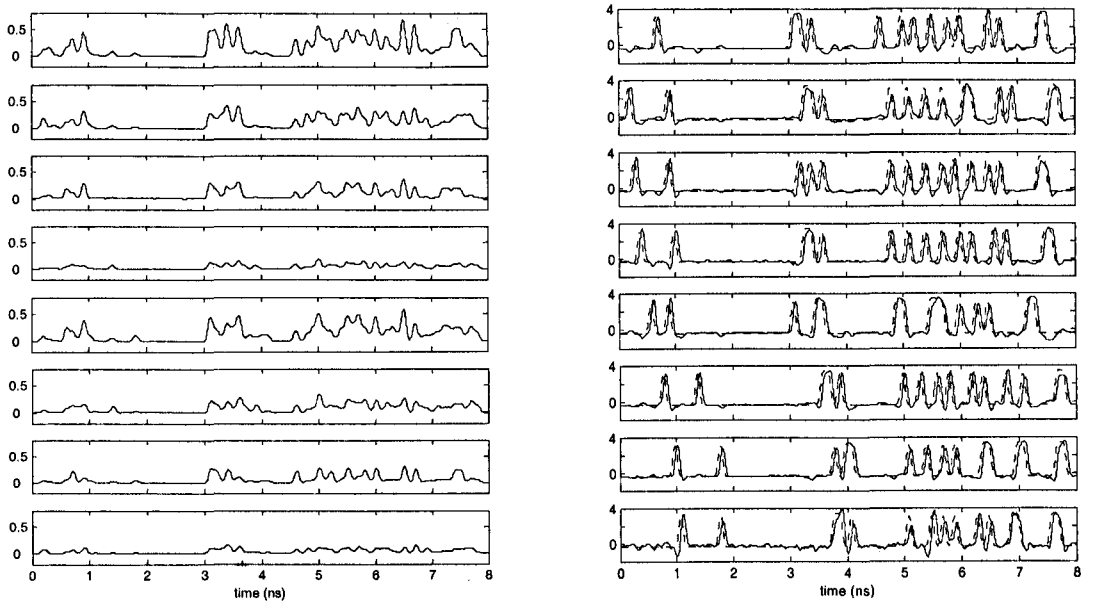

Figure 6.10: (a) observed photocurrents and (b) separation results for an 8-channel WDM transmission.

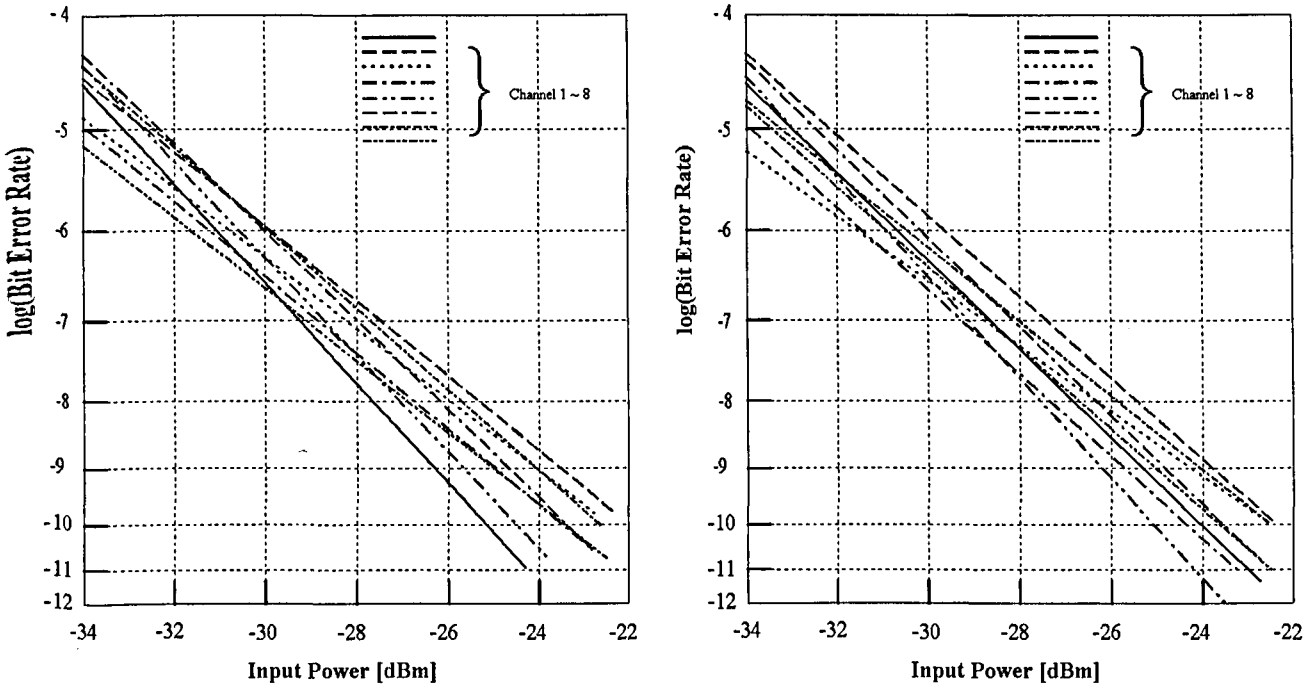

Figure 6.11: BER vs. Input Power curves. (a) EML method with the optical loop structure; (b) Gaussian assumption by VPI.

6.6 Summary

In this chapter we have proposed and demonstrated an optical transmission monitoring technique that utilizes blind signal separation methods based on higher-order statistics, and an optical-loop structure. This technique shows a reduced complexity, a reformative cost-efficiency, and an improved performance.

The EML method provides an approximate optimal solution (in the maximum-likelihood sense) for the case of two channels, and entails a computational cost of

$O(N^{5/2}L)$ when processing L-sample blocks of an N-channel WDM signal. For the signal distributions typically occurring in WDM monitoring, the method presents no undesired solutions. In addition, the case of spectrally white channels can also be handled, thus allowing beneficial reductions in the rates at which the photocurrents are sampled. Although the suggested procedure operates on signal blocks (batch processing), fast adaptive implementations can easily be designed as well [55].

Relative to previously proposed methods [50, 51], the optical-loop structure presented in this chapter has cost-effective features, especially when WDM signals are composed of a large number of channels. We have found a combination of BSS method and the quality measurement method presented in section 3.3, with most of the processing in the electrical domain, very close to those of traditional methods requiring expensive optical components, which simulated in an industrial simulation package (VPI).

It should be noted that the blind separation approach is not only useful in monitoring, but is effectively de-multiplexing the WDM signal. This feature envisages an enormous potential for BSS in optical transmission systems.

Chapter 7

Conclusion

This thesis has been devoted to the study of fibre nonlinear effects on WDM transmission system, and a novel WDM channel monitoring method through HOS-based blind signal separation.

As the theoretical foundation of this thesis, Chapter 2 has investigated on the pulse propagation in optical fibres. The nonlinear Schrödinger (NLS) equation has been investigated, several numerical approaches to the NLSE have been introduced, among which the split-step Fourier method is the most widely used approach. The theoretic model of Group-velocity dispersion (GVD) has been studied. Optical fibre nonlinear effects including Self-Phase Modulation (SPM), Cross-Phase Modulation (XPM), Four Wave Multiplexing (FWM) and Stimulated Brillouin Scattering (SBS) have been investigated. Analytical models for these effects have been presented.

Chapter 3 has introduced the typical WDM system constructions, and the expressions of signal and noise at the decision point for the Optical Pre-amplifiers (OPRs) have been derived. It is easy to see from the expressions of signal and noise that the signal-spontaneous emission beat noise is the most complicated term and the most time consuming for the calculations of signal and noise. The implementation time of the whole system is highly dependent on the calculation speed of this term. A method to evaluate average Q-factor from the eye diagrams and amplitude histograms, and thus evaluate BER through the Q-factor, has been introduced. This method provides fast and simple evaluations of WDM optical transmission quality with acceptable accuracy. Then, the implementation of the numerical simulation has been presented. The generation of the pseudo random binary sequence (PRBS) with different sequence length has been described. The procedure of the implementation of the system-level simulation has been given. The method to calculating the signal-spontaneous emission beat noise, which is more complicated and time consuming than any other calculations, has been described.

Chapter 4 has performed the influence of the variation in fibre parameters including fibre loss, dispersion and fibre effective core area. Prechirp is not necessary for the short distance transmission but for a long distance transmission a big sensitivity improvement is obtained by using negative prechirp. The optimum transmitter power increases greatly but the allowable transmitter power range decreases with a decreasing chirp parameter. The influence on sensitivity of the rise time is not serious

for the short transmission distances. The optimum sensitivity and the optimum transmitter power have very slight difference for different rise times. For a long transmission distance, a serious influence on sensitivity of the rise time is found. The optimum sensitivity becomes much better, the optimum transmitter power decreases and the allowable transmitter power range increases with an increasing rise time for a chirp-free input. The receiver sensitivity can be improved by an input with finite extinction ratio after a certain distance transmission. For a short transmission distance, the sensitivity nearly keeps constant for the extinction ratio over a certain value. For a long transmission distance, the optimum extinction ratio decreases when the transmission distance is longer. The maximum allowable transmitter power range shifts to a certain extinction ratio which is dependent on the transmission distance. The influence of the sequence length used in simulations is studied by using a 5th order Bessel electrical filter and a 5th order Butterworth electrical filter for 100 km and 150 km transmissions. It shows that a big receiver sensitivity difference is caused by short sequence length used but the sensitivity difference is very small when the sequence length used is longer than 128-bits. Thus, a 128-bits PRBS is reasonable for the transmission simulations when accuracy and calculation time are compromised.

Chapter 5 has investigated on the GVD-induced influences on an optical fibre transmission system, these influences can be remarkably restrained by applying proper dispersion management scheme. For C-band WDM transmission, four dispersion management schemes have been presented. Comparing the advantages and

disadvantages of different schemes, the author regards NZDF (D > 0) + DCF as generally the best fibre-combination scheme for dispersion management in WDM transmission systems. The influence of XPM effect on WDM transmission systems applying dispersion management has been investigated. If $\rho_j = \rho_{\mathrm{Rx},j} = 1$, the XPM-induced amplitude modulation can be hugely reduced, but can not be completely removed. While $\rho_{\mathrm{Rx},j} \neq 1$, ρ_j should deviate from 1 to reduce the influence of XPM. The noise amplification in a dispersion-managed WDM transmission system induced by modulation instability (MI) has been investigated. For optical fibre transmission system with positive dispersion (negative GVD), the MI-induced noise amplification becomes remarkable while the system is in-sufficiently compensated. The influence of SPM effect on WDM transmission systems applying dispersion management has been investigated. Appropriate in-sufficient compensation reduces or even eliminates the interference caused by pulse broadening. Dispersion management schemes have been implemented in a 16x10Gb/s WDM transmission system. Simulation results showed that the CSMF + DCF fibre-combination scheme has better performance in this case.

In chapter 6 we have proposed and demonstrated an optical transmission monitoring technique that utilizes blind signal separation methods based on higher-order statistics, and an optical-loop structure. This technique shows a reduced complexity, a reformative cost-efficiency, and an improved performance. The EML method provides an approximate optimal solution (in the maximum-likelihood sense) for the

case of two channels, and entails a computational cost of $O(N^{5/2}L)$ when processing L-sample blocks of an N-channel WDM signal. For the signal distributions typically occurring in WDM monitoring, the method presents no undesired solutions. Relative to previously proposed methods, the optical-loop structure presented in this chapter has cost-effective features, especially when WDM signals are composed of a large number of channels. We have found a combination of BSS method and the quality measurement method, with most of the processing in the electrical domain, very close to those of traditional methods requiring expensive optical components, which simulated in an industrial simulation package (VPI).

Finally, further research related to the subjects of this thesis might include topics such as the following. Applying the high-speed WDM system performance analysing and simulating platform introduced in this thesis to the industrial systems, e.g., 16×10Gb/s×500km CSMF or NZDF transmission system, to optimise the dispersion management schemes by comparing simulation results with measured parameters. The component models for other dispersion compensation methods, such as the fibre Bragg gratings, will be helpful to analyse different kinds of system configurations. It should be noted that the blind separation approach introduced in chapter 6 is not only useful in monitoring, but is effectively de-multiplexing the WDM signal. This feature envisages an enormous potential for BSS in optical transmission systems.

REFERENCES

Chapter 1

[1] See articles in: Special Issue on Factors Affecting Data Transmission Quality, *J. Lightwave Technology*, vol. 6, May 1988.

[2] See articles in: Feature Issue on Fundamental Challenges in Ultrahigh-Capacity Optical Fiber Communications Systems, *IEEE J. Quantum Electron.*, vol. 34, pp 2053-2103, November 1998.

[3] H. Ono, M. Yamada, and Y. Ohishi, "Gain-flattened EDFA for a WDM signal in 1.57-1.60 μ m wavelength region", *IEEE Photon. Technol. Lett.*, vol. 9, No. 5, pp. 596-598, 1997.

[4] A. K. Srivastava, Y. Sun, J. W. Sulhoff, et al, "1 Tb/s Transmission of 100 WDM 10Gb/s channels over 400 km of TrueWave™ fiber", *OFC '98*, PD10, San Jose, C.A., Feb., 1998.

[5] P. F. Wysocki, J. B. Judkins, R. P. Espindola, et al., "Broad-band erbium-doped fiber amplifier flattened beyond 40nm using long-period grating filter", *IEEE Photon. Technol. Lett.*, vol. 9, No. 10, pp. 1343-1345, 1997.

[6] S. H. Yun, B. W. Lee, H. K. Kim, et al, "Dynamic erbium-doped fiber amplifier with automatic gain flattening", *OFC/IOOC '99*, PD28, San Diego, CA, Feb., 1999.

[7] F. Forghieri, R. W. Tkach, A. R. Chraplyvy, "Fiber nonlinearities and their impact on transmission systems", in *Optical Fiber Telecommunications*, I. P. Kaminow, T. L. Koch, Eds, San Diego: Academic Press, 1997, vol. III-A, ch. 8, pp. 196-264.

[8] C. D. Poole, J. Nagel, "Polarization effects in lightwave systems", in *Optical Fiber Telecommunications*, I. P. Kaminow, T. L. Koch, Eds, San Diego: Academic Press, 1997, vol. III-A, ch. 8, pp. 114-161.

[9] A. H. Gnauck, R. M. Jopson, "Dispersion compensation for optical fiber systems", in *Optical Fiber Telecommunications*, I. P. Kaminow, T. L. Koch, Eds, San Diego: Academic Press, 1997, vol. III-A, ch. 8, pp. 162-195.

[10] R. W. Tkach, A. R. Chraplyvy, F. Forghieri, et al, "Four-photon mixing and high-speed WDM systems", *J. Lightwave Technology*, vol. 13, No. 5, pp. 841-849, 1995.

Chapter 2

[1] G. P. Agrawal, *Nonlinear Fiber Optics*, San Diego: Academic Press, Third Edition, 2001.

[2] T. R. Taha and M. J. Ablowitz, *J. Comput. Phys.*, 55, 203, 1984.

[3] S. A. Akhmanov, V. A. Vysloukh, and A. S. Chirkin, Chapter 1, *Optics of Femtosecond Laser Pulses*, New York: American Institute of Physics, 1992.

[4] D. Schadt and B. Jaskorzynska, *Electron. Lett.*, **23**, 1090(1987).

[5] B. Jaskorzynska and D. Schadt, *IEEE J. Quantum Electron.*, **24**, 2117(1988).

[6] S. Kumar, A. Selvarajan, and G. V. Anand, *J. Opt. Soc. Am.*, **B11**, 810(1994).

[7] D. Cotter, "Stimulated Brillouin scattering in monomode optical fiber", *J. of Optic. Commun.*, vol. 4, no. 1, pp. 10-19, 1983.

[8] T. Sugie, "Transmission limitations of CPFSK coherent lightwave systems due to stimulated Brillouin scattering in optical fiber", *J. Lightwave Tech.*, vol. 9, no. 9, pp. 1145-1155, 1991.

[9] E. Lichtman, R. G. Waarts, and A. A. Friesem, "Stimulated Brillouin scattering excited by a modulated pump wave in single-mode fibers", *J. Lightwave Tech.*, vol. 7, no. 1, pp. 171-174, 1989.

[10] R. G. Smith, "Optical power handling capacity of low loss optical fibers as determined by stimulated Raman and Brillouin scattering", *Appl. Opt.*, vol. 11, pp. 2489-2494, 1972.

[11] Y. Aoki, K. Tajima, and I. Mito, "Input power limits of single-mode optical fibers due to stimulated Brillouin scattering in optical communication systems", *J. Lightwave Tech.*, vol. 6, no. 5, pp. 710-719, 1998.

[12] R. H. Stolen, "Polarization effects in fiber Raman and Brillouin lasers", *IEEE J. Quantum Electron.*, vol. QE-15, pp. 1157-1160, 1979.

[13] A. Cosentino and E. Iannone, "SBS threshold dependence on line coding in

phase-modulated coherent optical systems", *Electron. Lett.*, vol. 25, pp. 1459-1460, 1989.

[14] M. Tatedal et al, "Suppression of stimulated Brillouin scattering in a strain-free single-mode optical fiber with non-uniform dopant concentration along its length", *OFC'93*, vol. 6, paper ThJ4, pp. 205-206, 1993.

[15] K. Shiraki, M. Ohashi, and M. Tateda, "Suppression of stimulated Brillouin scattering in a fiber by changing the core radius", *Electron. Lett.*, vol. 31, no. 8, pp. 668-669, 1995.

[16] X. P. Mao et al, "Stimulated Brillouin threshold dependence on fiber type and uniformity", *IEEE Phot. Elet. Lett.*, vol. 4, no. 1, pp. 66-69, 1992.

[17] A. Wada et al, "Suppression of stimulated Brillouin scattering by intentionally induced periodical residual-strain in single-mode optical fibers", *ECOC'91*, Paris, France, paper MoB1-1, pp. 25-28, 1991.

[18] P. A. Leilabady, et al, "Suppression of SBS in CATV distribution architectures employing long links", *ECOC'92*, Berlin, Germany, paper Th PD I.9, pp. 883-886, 1992.

[19] A. R. Chraplyvy, et al, "Limitations on lightwave communications imposed by optical fiber nonlinearities", *J. Lightwave Tech.*, vol. 8, no. 10, pp. 1548-1557, 1990.

[20] H. Yoshinaga, et al, "Nonlinear distortion due to stimulated Brillouin scattering and its suppression in SCM video-transmission systems", *OFC'93*, paper FC8, pp. 257-258, 1993.

[21] P. B. Hansen, et al, "2.488 Gbit/s unrepeatered transmission over 529 km using remotely pumped post- and pre-amplifiers, forward error correction, and dispersion compensation", *OFC'95*, vol. 8, paper PD25, 1995.

[22] C. G. Jørgensen, "Techniques for unrepeatered long distance optical transmission", Ph.D. thesis LD104, Dept. of Electromagnetic systems, Technical University of Denmark, pp. 44, 1994.

[23] Y. K. Park et al, "A 5 Gbit/s repeaterless transmission system using erbium-doped fiber amplifiers", *IEEE Phot. Tech. Lett.*, vol. 5, no. 1, pp. 79-82, 1993.

[24] J. E. J. Alphonsus et al, "5 Gbit/s repeaterless transmission over 339 km by using an Er-doped fiber post-preamplifiers, and remote amplifiers", *OFC'95*, paper WG2, pp. 121-122, 1995.

[25] L. D. Pedersen, et al, "Uncoded NRZ 2.488 Gbit/s transmission over 347 km standard fiber, 67 dB span loss, using a remotely pumped amplifier, SBS suppression, SPM optimization and Raman gain", *OFC'94*, paper PD28, pp. 128-131, 1994.

[26] S. S. Sian et al, "511 km at 2.5 Gbit/s and 531 km at 622 Mbit/s - Unrepeatered transmission with remote pumped amplifiers, forward error correction and dispersion compensation", OFC'95, paper PD26, 1995.

[27] P. B. Hansen et al, "423 km repeaterless transmission at 2.488 Gbit/s using remotely pumped post- and pre-amplifiers", ECOC'94, Florence, Italy, postdeadline paper, pp. 57-60, 1994.

Chapter 3

[1] Feature Issue on "Fundamental Challenges in Ultrahigh-Capacity Optical Fiber Communications Systems", *IEEE J. Quantum Electron.*, vol. 34, pp. 2053-2103, November 1998.

[2] H. Masuda, S. Kawai, K-I Suzuki, and K. Aida, "Untrawide 72-nm 3-dB gain-band optical amplification with erbium-doped Fluoride fiber amplifiers and distributed Raman amplifiers", *IEEE Photon. Technol. Lett.*, vol 10, pp. 516-518, 1998.

[3] F. A. Flood: "L-band Erbium-doped fiber amplifiers", paper WG1, *Technical Digest of the OFC '2000*, Baltimore, USA, pp. 102-104, 2000.

[4] D. Breuer, H. J. Ehrke, F. K. Uppers, and H. G. Webber, et al, "Unrepeated 40 Gb/s RZ single-channel transmission at 1.55 μ m using various fiber types", *IEEE Photon. Technol. Lett.*, vol. 10, pp. 822-824, 1998.

[5] C. M. Weinert, R. Ludwig, and W. Pieper, et al, "40 Gb/s and 4x40 Gb/s TDM/WDM standard fiber transmission", *IEEE J. of Lightwave Technol.*, vol. 17, pp. 2276-2284, 1999.

[6] D. Bayart, S. Gauchard, and S. Gurib, "Analysis of 50 GHz spacing in WDM transmission over G. 652 and NZ-DSF fibres", *ECOC '98*, Madrid, Spain, pp. 303-304, 1998.

[7] N. S. Bergano, C. R. Davidson, and H. Abdelkader, et al, "640 Gb/s transmission of sixty-four 10 Gb/s WDM channels over 7200 km with 0.33 (bits/s)/Hz spectral

efficiency", PD2, *OFC '99*, San Diego, USA, 1999.

[8] B. F. Jørgensen, B. Mikkelsen, and C. J. Mahon, "Analysis of optical amplifier noise in coherent optical communication systems with optical image rejection receivers", *J. Lightwave Technol.*, vol. LT-10, no. 5, pp. 660-671, 1992.

[9] S. D. Personick, "Receiver design for digital fiber optic communication systems I", *BSTJ.*, vol. 53, pp. 843-874, 1973.

[10] G. Jacobsen, "Noise in digital optical transmission systems", Chapter 12, Artech House, 1994.

[11] H. Urkowitz, "Signal theory and random processes", Dedham, MA: Artech House, 1983.

[12] B. F. Jørgensen, B. Mikkelsen, and C. J. Mahon, "Analysis of optical amplifier noise in coherent optical communication systems with optical image rejection receivers", *J. Lightwave Technol.*, vol. LT-10, no. 5, pp. 660-671, 1992.

[13] A. Papoulis, "Probability, random variables, and stochastic processes", McGraw-Hill Book Company, 1984.

[14] A. Papoulis, "Signal analysis", McGraw-Hill Book Company, 1984.

[15] N. Hanik, A. Gladisch, et al, "Application of amplitude histograms to monitor performance of optical channels", *Electronics Letters*, **5**, pp. 403-404. 1999.

[16] I. Shake, H. Takara, K. Uchiyama, and Y. Yamabayashi, "Quality monitoring of optical signals influenced by chromatic dispersion in a transmission fiber using averaged *Q*-factor evaluation", *IEEE Photon. Technol. Lett.*, **4**, pp. 385-387, 2001.

[17] N. S. Bergano, F. W. Kerfoot, and C. R. Davidson, "Margin measurements in optical amplifier systems", *IEEE Photon. Technol. Lett.*, **3**, pp. 304-306, 1993.

[18] I. Shake, H. Takara, S. Kawanishi, Y. Yamabayashi, "Optical signal quality monitoring method based on optical sampling", *Electron. Lett.*, **22**, pp. 2152-2154, 1998.

[19] M. I. Skolnik, "Introduction to radar systems", McGraw-Hill Book Company, 1981.

Chapter 4

[1] B. F. Jørgensen, "Unrepeatered transmission at 10 Gbit/s over 204 km standard fiber", *ECOC'94*, Florence, Italy, pp. 685-688, 1994.

[2] M. Murakami, et al, "10 Gbit/s, 6000 km transmission experiment using erbium-doped fiber in-line amplifiers", *Electron. Lett.*, vol. 28, no.14, pp.2254-2255, 1992.

[3] G. P. Agrawal, *Nonlinear Fiber Optics*, San Diego: Academic Press, Third Edition, 2001.

[4] Y. Feng, Y. He, "Performance analysis of semiconductor multi-quantum-well Mach-Zender optical modulator", Modern Cable Transmission, Mar., 2000.

Chapter 5

[1] D. Marcuse, *Appl. Opt.*, **20**, 3573, 1981.

[2] G. P. Agrawal, *Fiber-Optic Communication Systems*, Chapter 2, New York: Wiley, 1997.

[3] G. P. Agrawal and N. K. Dutta, *Semiconductor Lasers*, Chapter 6, 2nd ed., New York: Van Nostrand Reinhold, 1993.

[4] M. Nishimura, M. Onishi, "Dispersion-compensating fibers and their applications", OFC'96, ThA1, San Jose, CA, 1996.

[5] M. Onishi, H. Kanamori, and T. Kato, "Optimization of dispersion-compensating fibers considering self-phase modulation suppression", OFC'96, ThA2, San Jose, CA, 1996.

[6] Y. Akasaka, R. Sugizaki, A. Umeda, "High-dispersion-compensation ability and low nonlinearity of W-shaped DCF", *OFC'96*, ThA3, San Jose, CA, 1996.

[7] D. J. DiGivanni, D. P. Jablonowski, and M. F. Fan, "Advances in fiber design and processing", in *Optical Fiber Communications*, vol. III-A, Chapter 4, pp. 79-83, I. P. Kaminow, T. L. Koch, Eds., San Diego: Academic Press, 1997.

[8] Qian Yu, "Analysis of fiber dispersion, nonlinearity and EDFA effects on WDM system performance", PhD thesis, Tsinghua University, 1999.

Chapter 6

[1] S. L. Altimann, *Rotations, Quaternions and Double Groups*, Oxford: Oxford University Press, pp. 317, 1986.

[2] S. Amari and A. Cichocki, "Adaptive blind signal processing – neural network approaches", *Proc. Of the IEEE*, vol. 86, No. 10, pp. 2026-2048, 1996.

[3] S. Amari, "Superefficiency in blind source separation", *IEEE Trans. On Sign. Proc.*, vol. 47, No. 4, pp. 936-944, 1999.

[4] P. O. Amblard and J. M. Brossier, "Adaptive estimation of the fourth-order cumulant of a white stochastic process", *Sign. Proc.*, vol. 42, pp. 37-43, 1995.

[5] E. Bacharakis, *Separation of maternal and foetal ECG using blind source separation methods*, MSc thesis, University of Strathclyde, Glasgow, Scotland, UK, 1995.

[6] A. Belouchrani and J. F. Cardoso, "Maximum likelihood source separation for discrete sources", EUSIPCO'94, pp. 768-771, Edinburgh, Scotland, 1994.

[7] A. J. Bell and T. J. Sejnowski, "An information-maximization approach to blind separation and blind deconvolution", *Neural Computation*, vol. 7, No. 6, pp. 1129-1159, 1995.

[8] H. Sahlin, *Blind Signal Separation by second order statistics*, PhD thesis, Chalmers University of Technology, Sweeden, 1998.

[9] E. Weinstein, M. Feder and A. V. Oppenheim, "Multi-channel signal separation by decorrelation", *IEEE Trans. on Speech and Audio Proc.*, vol. 1, No. 4, pp.

405-413, 1993.

[10] D. Yellin and E. Weinstein, "Criteria for multichannel signal separation", *IEEE Trans. on Sign. Proc.*, vol. 42, No. 8, pp. 2158-2168, 1994.

[11] D. Yellin and E. Weinstein, "Multichannel signal separation: methods and analysis", *IEEE Trans. on Sign. Proc.*, vol. 44, No. 1, pp. 106-118, 1996.

[12] L. Tong, R. Liu, V. C. Soon and Y. F. Huang, "Indeterminacy and identifiability of blind identification", IEEE Trans. on Sign. Proc., vol. 38, No. 5, pp. 499-509, 1991.

[13] L. Tong, S. Yu, Y. Inouye and R. Liu, "A necessary and sufficient condition of blind identification", *Proceedings of the International Signal Processing Workshop on Higher-Order Statistics*, Chamrousse, France, pp. 261-264, 1991.

[14] L. Tong, Y. Inouye and R. Liu, "Waveform-preserving blind estimation of multiple independent sources", *IEEE Trans. on Sign. Proc.*, vol. 41, No. 7, pp. 2461-2470, 1993.

[15] J. L. Lacoume and P. Ruiz, "Source identification: a solution based on the cumulants", *Proceedings ICASSP'88*, Minneapolis, USA, 1988.

[16] J. L. Lacoume, M. Gaeta and P. O. Amblard, "From order 2 to HOS: new tools and applications", EUSIPCO'92, Brussels, pp. 91-98, 1992.

[17] J. F. Cardoso, "Eigen-structure of the fourth-order cumulant tensor with application to the blind source separation problem", *Proceedings ICASSP'90*, Albuquerque, New Mexico, USA, vol. 5, pp. 2655-2658, 1990.

[18] P. Comon and O. Grellier, "Non linear inversion of underdetermined mixtures",

Proceedings ICA'99, Aussois, France, pp. 461-465, 1999.

[19] D. R. Beillinger, *Time Series Data Analysis and Theory*, San Francisco: Holden-Day, 1981.

[20] J. M. Mendel, "Tutorial on higher-order statistics (spectra) in signal processing and system theory: theoretical results and some applications", *Proceedings of the IEEE*, vol. 79, No. 3, pp. 278-305, 1991.

[21] C. L. Nikias and J. M. Mendel, "Signal processing with higher-order statistics", *IEEE Sign. Proc. Magazine*, vol. 10, No. 3, pp. 10-37, 1993.

[22] J. F. Cardoso and A. Souloumiac, "Blind beamforming for non-Gaussian signals", *IEE Proceedings-F*, vol. 140, No. 6, pp. 362-370, 1993.

[23] J. F. Cardoso and B. H. Laheld, "Equivariant adaptive source separation", *IEEE Trans. on Sign. Proc.*, vol. 44, No. 12, pp. 3017-3030, 1996.

[24] P. Comon, "Separation of stochastic processes", *Proceedings of the Workshop on Higher-Order Spectral Analysis*, Vail, Colorado, USA, pp. 174-179, 1989.

[25] P. Comon, "Independent component analysis, a new concept?", *Sign. Proc.*, vol. 36, No. 3, pp. 287-314, 1994.

[26] P. Comon, "Separation of sources using higher-order cumulants", *SPIE vol. 1152 Advanced Algorithms and Architectures for Signal Processing IV*, pp. 170-181, 1989.

[27] J. A. Gallian, *Contemporary Abstract Algebra*, Fourth Edition, Boston, MA: Houghton Mifflin Company, 1998.

[28] J. F. Cardoso, "Blind signal separation: statistical principles", *Proceedings of the*

IEEE, vol. 86, No. 10, pp. 2009-2025, 1998.

[29] I. J. Clarke, "Direct exploitation of non-Gaussianity as a discriminant", *Proceedings EUSIPCO'98*, Rhodes, Greece, vol. IV, pp. 2057-2060, 1998.

[30] J. F. Cardoso, "Statistical principles of source separation", *Proceedings IFAC SYSID'97*, Fukuoka, Japan, pp. 1837-1844, 1997.

[31] A. Benveniste, K. Abed-Meraim, et al, "A blind source separation technique using second-order statistics", *IEEE Trans. on Sign. Proc.*, vol. 45, No. 2, pp.434-444, 1997.

[32] F. Harroy and J. L. Lacoume, "Maximum likelihood estimators and Cramer-Rao bounds in source separation", *Sign. Proc.*, vol. 55, pp. 167-177, 1996.

[33] P. Comon, "Higher-order separation, application to detection and localization", *EUSIPCO'90*, Barcelona, Spain, pp. 277-280, 1990.

[34] J. F. Cardoso, "Iterative techniques for blind source separation using only fourth-order cumulants", *EUSIPCO'92*, Brussels, pp. 739-742, 1992.

[35] J. F. Cardoso, "On the performance of orthogonal source separation algorithms", *EUSIPCO'94*, Edinburgh, Scotland, pp. 776-779, 1994.

[36] R. A. Johnson and D. W. Wichern, *Applied Multivariate Statistical Analysis*, 2nd Ed., Prentice Hall, 1988.

[37] K. V. Mardia, J. T. Tent and J. M. Bibby, *Multivariate Analysis*, London: Academic Press, 1979.

[38] L. L. Scharf, *Statistical Signal Processing. Detection, Estimation and Time Series Analysis*, Addison-Wesley, 1991.

[39] E. Biglieri and K. Yao, "Some properties of singular value decomposition and their applications to digital signal processing", *Sign. Proc.*, vol. 18, No. 3, pp. 277-289, 1989.

[40] G. H. Golub and C. F. Van Loan, *Matrix Computations*, 2nd Ed., Baltimore: The Johns Hopkins University Press, 1989.

[41] W. H. Press, B. P. Flannery, et al, *Numerical Recipes in C. The Art of Scientific Computing*, Cambridge: Cambridge University Press, 1988.

[42] D. P. Pham, P. Garat and C. Jutten, "Separation of a mixture of independent sources through a maximum-likelihood approach", *EUSIPCO'92*, Brussels, pp. 771-774, 1992.

[43] S. Kotz and N. L. Johnson, *Encyclopedia of Statistical Sciences*, New York: John Wiley & Sons, 1982.

[44] D. L. Wallace, "Asymptotic approximations to distributions", *Annals of Mathematical Statistics*, vol. 29, pp. 635-654, 1958.

[45] V. Zarzoso, *Closed-Form Higher-Order Estimators for Blind Separation of Independent Source Signals in Instantaneous Linear Mixtures*, PhD thesis, the University of Liverpool, 1999.

[46] A. Stuart and J. K. Ord, *Kendall's Advanced Theory of Statistics*, vol. I, 6th Ed., London: Edward Arnold, 1994.

[47] M. P. H. van de Bergh, J. J. G. M. van der Tol and H. J. S. Dorren, "A novel WDM monitoring method," Photonic Network Communications, No. 4, pp. 323-329, 1999.

[48] E. Tangdiongga, N. Calabretta, P. C. W. Sommen and H. J. S. Dorren, "WDM monitoring technique using adaptive blind signal separation," IEEE Photonic Technology Letters, No. 3, pp. 248-250, 2001.

[49] S van Gerven and D. van Compernolle, "Signal separation by symmetric adaptive decorrelation: stability, convergence, and uniqueness," IEEE Transactions on Signal Processing, No. 7, pp. 1602-1612, 1995.

[50] Y. Feng, V. Zarzoso and A. K. Nandi, "WDM monitoring through blind signal separation", in *Proceedings of OFC'02*, Anaheim, California, USA, pp. 746-748, 2002.

[51] Y. Feng, V. Zarzoso and A. K. Nandi, "WDM monitoring using blind signal separation based on higher-order statistics", in *Proceedings of DSP'02*, Greece, pp. 155-158, 2002.

[52] A. Hyvärinen, J, Karhunen and E. Oja, *Independent components analysis*, New York: John Wiley & Sons, 2001.

[53] L. E. Nelson, S. T. Cundiff, and C. R. Giles, "Optical monitoring using data correlation for WDM systems," IEEE Photonics Technology Letters, No. 7, pp. 1030-1032, 1998.

[54] VPIVirtualPhotonics, *VPI Photonic Modules Reference Manual*, pp. 45-49, 2002.

[55] V. Zarzoso and A. K. Nandi, "Adaptive blind source separation for virtually any source probability density function," *IEEE Trans. on Sign. Proc.*, No. 2, pp. 477-488, 2000.

[56] A K Nandi (Ed.), "Blind estimation using Higher-Order Statistics", *Kluwer Academic Publishers*, Amsterdam, Netherlands, 1999 (ISBN 0-7923-8442-3).

[57] V Zarzoso and A K Nandi, "Optimum delay blind MIMO equalization using independent component analysis", *Journal of Adaptive Control and Signal Processing,* vol. 18, no. 3, pp. 245-263, 2004.

[58] Y. Feng, V. Zarzoso and A. K. Nandi, "Quality monitoring of WDM channels with blind signal separation methods", *Journal of Optical Networking,* vol. 3, pp. 477-489, 2004.

[59] V Zarzoso and A K Nandi, "Exploiting non-Gaussianity in blind identification and equalization of MIMO FIR channels", *IEE Proceedings – Part VIS,* vol. 151, no. 1, pp. 69-75, 2004.

[60] V Zarzoso and A K Nandi, "Closed-form estimators for blind separation of sources – Part.II: Complex mixtures", *Wireless Personal Communications,* vol. 21, no. 1, pp. 29- 48, 2002.

[61] V Zarzoso and A K Nandi, "Closed-form estimators for blind separation of sources – Part I: Real mixtures", *Wireless Personal Communications,* vol. 21, no. 1, pp. 5-28, 2002.

[62] F Herrmann and A K Nandi, "Blind separation of linear instantaneous mixtures using closed form estimators", *Signal Processing,* vol. 81, no. 7, pp. 1537-1556, 2001.

[63] A K Nandi and F Herrmann, "Fourth-order cumulant based estimator for independent component analysis", *Electronics Letters,* vol. 37, no. 7, pp.

469-470, 2001.

[64] V Zarzoso and A K Nandi, "Non-invasive fetal electrocardiogram extraction: blind separation versus adaptive noise cancellation", *IEEE Transactions on Biomedical Engineering,* vol. 48, no. 1, pp. 12-18, 2001.

[65] V Zarzoso, A K Nandi, F Herrmann and J Millet-Roig, "Combined estimation scheme for blind source separation with arbitrary source PDFs", *Electronics Letters,* vol. 37, no. 2, pp. 132-133, 2001.

[66] V Zarzoso and A K Nandi, "Adaptive blind source separation for virtually any source probability density function", *IEEE Transactions on Signal Processing,* vol. 48, no. 2, pp. 477-488, 2000.

[67] V Zarzoso and A K Nandi, "Blind separation of independent sources for virtually any source probability density function", *IEEE Transactions on Signal Processing,* vol. 47, no. 9, pp. 2419-2432, 1999.